

CHIP-BASED BIOASSAY BASED ON SURFACE PLASMON RESONANCE FOR
LABEL-FREE BIOMOLECULAR DETECTION

By

PEI-YU CHUNG

A DISSERTATION PRESENTED TO THE GRADUATE SCHOOL
OF THE UNIVERSITY OF FLORIDA IN PARTIAL FULFILLMENT
OF THE REQUIREMENTS FOR THE DEGREE OF
DOCTOR OF PHILOSOPHY

UNIVERSITY OF FLORIDA

2011

© 2011 Pei-Yu Chung

To my family

ACKNOWLEDGMENTS

I would like to thank my advisor, Dr. Christopher Batich, for his guidance and support. His philosophy of applying engineering for improving lives serves as a role model in my research career. I also thank my committee members: Dr. Cammy Abernathy, Dr. Eugene Goldberg, Dr. Gregory Schultz, Dr. Henry Hess, and Dr. Mark Davidson for their supervisions. Dr. Peng Jiang gives me bountiful assistances, and his passion stimulates my creativity. The meaningful collaboration with Dr. Pei-Kuen Wei broadened my vision. I truly appreciate Dr. Tzong-Jih Cheng and other professors in NTU for their supports since my undergraduate. Dr. Weihong Tan gave me genuine suggestions and encouragement, so I could improve myself and strengthen my heart. I also enjoyed the time engaging in the significant project with the Lovelace Respiratory Research Institute. Dr. Ching-Chung Kuo's encouragement from University of North Texas lightened up my life. Jennifer Wrighton, Kerry Siebien, Gill Brubaker, and Ludie Harmon are respectful professions at UF, and they play important roles in my Ph.D.

I am grateful to love and patience from my grandmother and parents, Fu-Lan Li (李福蘭), Chen-Yu Chung (鍾成裕) and Ying-Liang Liu (劉盈良). They sculpture my personality and morality, and let me be the person I want to be. My sibling, Eva Chung, is my oldest friend who protects me since I was born. My aunts in Li, Liu, and Wu families take care of me as their daughter. They all make my life. I also appreciate all the supports from all of my colleagues and friends, especially Kuang-Li Lee at Sinica and John Azeke, Titilayo Moloye, Tzung-Hua Lin, Zhi Zhu, Travis Kemper, Xiangling Xiong, and Shi-Fen Yeh at UF. Their kindnesses are my strongest support after coming

to United States. I treasure the love from Vivien Lee and Yu-Lin Wang. They forever vibrate in my heart.

I thank God for giving me everything to pursue my beloved and loving life.

TABLE OF CONTENTS

	<u>page</u>
ACKNOWLEDGMENTS.....	4
LIST OF FIGURES.....	9
LIST OF ABBREVIATIONS.....	12
ABSTRACT.....	14
CHAPTER	
1 INTRODUCTION	16
1.1 Motivation	16
1.1.1 Global Health and Bioanalytical Systems	16
1.1.2 Surface Plasmon Resonance Sensor.....	17
1.2 Study Outline	19
2 SURFACE PLASMON RESONANCE IN GOLD NANOSLIT ARRAYS	21
2.1 Background.....	21
2.1.1 Surface Plasmon	21
2.1.2 Substrates for Surface Plasmon Resonance.....	22
2.1.3 Multispectral Analysis	24
2.1.4 Biosensing Application	25
2.1.5 Raman Spectroscopy and Surface-enhanced Raman Spectroscopy	25
2.2 Experimental.....	27
2.2.1 Fabrication of Gold Nanoslit Arrays	27
2.2.2 Apparatus for Using the Gold Nanoslit Sensor	27
2.2.3 Surface-enhanced Raman Spectroscopy	28
2.2.4 Bioassay of Surface-enhanced Raman Spectroscopy by Using Aptamer.....	28
2.3 Results and Discussions.....	29
2.3.1 Periodicity Effects on the Gold Nanoslit Arrays in Microscale Spacing ...	29
2.3.2 Periodicity Effects on the Nanoscale Gold Nanoslit Arrays	31
2.3.3 Observation of Localized Surface Plasmon Resonance on Nanoslit Array	34
2.3.4 Observation of Wood's anomalies on Gold Nanoslit Arrays	36
2.3.5 Refractive Index Sensing by Using Multispectral Analysis	37
2.3.6 Influence of Nanoslit Periodicity on SERS Spectra	41
2.3.7 Surface-enhanced Raman Scattering Peak Identification of DNA Aptamer.....	41
2.4 Summary	43

3	SURFACE PLASMON RESONANCE IN GOLD NANOPYRAMID ARRAYS.....	60
3.1	Background.....	60
3.1.1	Gold Nanopyramid for Label-free and Real-time Biosensing.....	60
3.1.2	Tilted Angle and Vertical Reflection Modes.....	62
3.1.3	Finite-difference Time-domain Simulation (FDTD).....	63
3.2	Experimental.....	63
3.2.1	Fabrication of Gold Nanopyramids.....	63
3.2.2	Apparatus for using the Gold Nanopyramid Sensor.....	64
3.2.3	Finite-difference Time-domain Simulation.....	65
3.2.4	Bioassay of Gold Nanopyramid Sensor.....	66
3.3	Results and Discussions.....	67
3.3.1	Fabrication of Gold Nanopyramid Arrays.....	67
3.3.2	Gold Nanopyramid Sensor in a Tilted Angle Reflection Mode.....	68
3.3.3	Finite-difference Time-domain Simulations in Tilted Angle Reflection Mode.....	69
3.3.4	Gold Nanopyramid Biosensor in Tilted Angle Reflection Mode.....	70
3.3.5	Refractive Index Sensing in a Vertical Reflection Mode.....	70
3.3.6	Finite-difference Time-domain Simulated Electromagnetic Field Distributions.....	72
3.3.7	Gold Nanopyramid Biosensor in a Vertical Reflection Mode.....	73
3.4	Summary.....	75
4	GOLD-POLYMER HYBRID PYRAMID BIOSENSORS.....	91
4.1	Background.....	91
4.2	Experimental.....	93
4.2.1	Fabrication of Gold-polymer Hybrid Nanopyramids.....	93
4.2.2	Apparatus for Using the Gold-polymer Hybrid Sensor.....	94
4.2.3	Surface-enhanced Raman Spectroscopy.....	95
4.2.4	Finite-difference Time-domain Simulation.....	95
4.3	Results and Discussions.....	96
4.3.1	Fabrication of Gold-polymer Hybrid Nanopyramid.....	96
4.3.2	Extraordinary Transmission of Gold-polymer Hybrid Nanopyramid.....	97
4.3.3	Finite-difference Time-domain Simulation.....	99
4.3.4	Refractive Index Sensing of Gold-polymer Hybrid nanopyramid.....	100
4.3.5	Surface-enhanced Raman Scattering Peak Identification of DNA aptamer.....	102
4.4	Summary.....	104
5	CONCLUSIONS.....	116
6	FUTURE WORK.....	118
6.1	Preliminary Experiments.....	118
6.2	Preliminary Results.....	120

LIST OF REFERENCES 130
BIOGRAPHICAL SKETCH..... 141

LIST OF FIGURES

<u>Figure</u>		<u>page</u>
2-1	The scheme of gold nanoslit array sensing apparatus.	44
2-2	The SEM image of a 2 μm -periodic gold nanoslit array.	45
2-3	The transmission spectra of the microscale gold nanoslit arrays with different periodicity in water.	46
2-4	The transmission spectrum of the 400 nm-periodicity gold nanoslit arrays immersed in different refractive index solutions.	47
2-5	The baseline-subtracted transmission spectrum of the 400 nm-periodicity gold nanoslit arrays.	48
2-6	The baseline-subtracted transmission spectrum of the 600 nm-periodicity	49
2-7	The configuration of light-SPP coupling and induced dipole coupling.	50
2-8	The transmission spectra of the nanoscale gold nanoslit arrays showing the LSPR region.	51
2-9	The transmission spectrum of the 1 μm -periodicity gold nanoslit arrays showing the LSPR and Wood's anomalies.	52
2-10	Step response by adding different refractive index solutions.	53
2-11	A plot of total response versus varied RI from multiple runs.	54
2-12	The sensitivity comparison in the gold nanoslit arrays according to different slit periodicity varied from 400 nm to 15 μm	55
2-13	The SERS spectra of the gold nanoslit arrays modified with benzenethiol.	56
2-14	The SERS spectra of aptamer conjugated on the nanoslit array with slit periodicity 2 μm and 5 μm respectively.	57
2-15	The SERS spectra of aptamer conjugated on the 2 μm -periodicity nanoslit array compared with control.	58
2-16	The SERS spectra of aptamer conjugated on the 2 μm -periodicity nanoslit array before and after adding thrombin protein.	59
3-1	Scheme of various interrogations to monitor shifts in coupling wavelength, coupling angle, and light intensity generated by biomolecular binding events [100].	76

3-2	Scheme of excitation of SPPs by using a polarized light source. The size and properties of gold nanopyramid arrays were set to mimic the real conditions. ...	77
3-3	Tilted-view at 35° of SEM image of a templated gold nanopyramid arrays. 320 nm of silica spheres were used to generate the template.....	78
3-4	Magnified view of SEM image of the gold nanopyramid arrays.	78
3-5	Optical reflection of white light excited at 45° on the gold nanopyramid array immersed in glycerol solutions of different refractive indices.....	79
3-6	FDTD-simulated optical reflection of plane wave from a gold nanopyramid array immersed in liquids of different refractive indices.	80
3-7	Comparison between normalized experimental and FDTD-simulated optical reflection from nanopyramids with different sizes of tips.	81
3-8	Comparison of detection sensitivity between the experimental result and FDTD simulation.....	82
3-9	Normalized reflection spectra obtained from a gold nanopyramid array conjugated with anti-alcohol dehydrogenase and the target protein.....	83
3-10	The simulated reflectivity in an environmental refractive index 1.33 and 1.35 respectively.....	84
3-11	The experimental reflectivity changes in different environmental refractive indices.	85
3-12	The sensitivity to the environmental refractive index calculated from the linear fit of reflection spectra dip position to the environmental refractive indices	86
3-13	The FDTD-simulated electromagnetic field distribution in x-z cross section.....	87
3-14	The FDTD-simulated electromagnetic field distribution in x-y cross section. The vertical position of the monitor is at the tip of nanopyramids.	88
3-15	The biomolecule detection of anti-alcohol dehydrogenase antibody and different concentration levels of alcohol dehydrogenase	89
3-16	The plot of AD concentration versus the shifts in the spectra based on a single run.....	90
4-1	Schematic of the optical SPR measurement system adapted from a bright-field inverted microscope.....	105
4-2	AFM images of nanopyramid arrays templated from the inverted silicon pyramidal pits.	106

4-3	Photos of a one-inch-sized hybrid nanopyramid arrays.....	107
4-4	Transmission spectra through hybrid nanopyramid arrays immersed in various refractive index solutions.....	108
4-5	Simulated electromagnetic field enhancement by FDTD modeling.	109
4-6	Simulated electromagnetic field enhancement by FDTD modeling.	110
4-7	Simulated electromagnetic field enhancement by FDTD modeling at cross-sectional of x-y surface.....	111
4-8	Evaluation of refractive index sensitivity and reproducibility for hybrid nanopyramid arrays.....	112
4-9	Evaluation of refractive index sensitivity and repeatability for hybrid nanopyramid arrays.....	113
4-10	SERS spectra for characterizing the thrombin aptamer which is modified on the hybrid nanopyramid array and filled in the silicon wafer..	114
4-11	SERS spectra for characterizing the thrombin aptamer and the complex of thrombin aptamer-thrombin protein..	115
6-1	Real-time biosensing for anti-BSA and BSA binding.	124
6-2	Concentration calibration of BSA detection. Detected total response versus the logarithm of concentrations of BSA was plotted to obtain the detection	125
6-3	Real-time human thrombin detection.....	126
6-4	Adding BSA to the thrombin sensor.....	127
6-5	The trivial amount of thrombin protein on the sensor.....	128
6-6	Schematic of a dual sensing system.	129

LIST OF ABBREVIATIONS

Ar	Argon
Au	Gold
AFM	Atomic force microscope
APTCS	Acryloxypropyl trichlorosilane
BSA	Bovine serum albumin
BW-SPP	Bloch wave-surface plasmon polariton
DNA	Deoxyribonucleic acid
ELISA	Enzyme-linked immunosorbent assay
ETPTA	Ethoxylated trimethylolpropane triacrylate
FDTD	Finite-difference time-domain
IgG	Immunoglobulin G
LSPR	Localized surface plasmon resonance
NIR	Near Infrared
NPGS	Nano-pattern generating system
OTE	Octadecyltriethoxysilane
PCR	Polymerase chain reaction
PDMA	Polydimethylsiloxane
PML	Perfect matched layers
PMMA	Poly (methyl methacrylate)
POCT	Point-of-care testing
RI	Refractive index

RIU	Refractive index unit
SEM	Scanning electron microscopy
SELEX	Systematic Evolution of Ligands by Exponential Enrichment
SERS	Surface-enhanced Raman scattering
SPPs	Surface plasmon polaritons
SPR	Surface plasmon resonance
SPRi	Surface plasmon resonance imaging
T	Transmission
Ti	Titanium
TM	Transverse-magnetic
WA	Wood's anomalies

Abstract of Dissertation Presented to the Graduate School
of the University of Florida in Partial Fulfillment of the
Requirements for the Degree of Doctor of Philosophy

CHIP-BASED BIOASSAY BASED ON SURFACE PLASMON RESONANCE FOR
LABEL-FREE BIOMOLECULAR DETECTION

By

Pei-Yu Chung

May 2011

Chair: Christopher Batich
Major: Materials Science and Engineering

Optical sensing techniques utilizing the surface plasmon resonance (SPR) effect on nanostructures are of great importance for label-free and high sensitivity biomolecule detections. Compared with conventional prism-based SPR sensing tool, nanostructured substrate is promising for the development of low-cost and portable biosensors. This dissertation studied the interesting optical characteristics generated on various periodic nanostructures including gold nanoslits, gold nanopyramids, and hybrid nanopyramids theoretically and experimentally. A set of engineered nanoslit arrays with periodicity ranging from nm to μm were able to fine tune optical responses and achieved a high sensitivity of 28600 %T nm/RIU with multispectral analysis (RIU=refractive index unit). Gold nanopyramids and hybrid nanopyramids were fabricated by low-cost and efficient methods, and finite-difference time-domain modeling was used to simulate the electromagnetic field distributions and the theoretical spectra. In experiments, the sensitivity achieved 239 nm/RIU without multispectral analysis and 2000 nm/RIU with multispectral analysis for gold nanopyramids and hybrid nanopyramids respectively.

Moreover, detection of biomolecular binding events is demonstrated by using transmission/reflection interrogations and surface-enhanced Raman spectroscopy. These novel substrates exhibit strong SPR effect and are promising for developing sensitive biological and chemical sensors for real-time and label-free detections.

CHAPTER 1 INTRODUCTION

1.1 Motivation

1.1.1 Global Health and Bioanalytical Systems

Bioanalytical systems support in-depth research in fields such as biomolecular interactions, cell signaling process, gene expression, and drug development [1-3]. These fundamental research areas help discover pathogenic mechanisms as well as efficient treatments, and thus provide a meaningful contribution to improve global health. Moreover, applying bioanalytical systems for the purpose of diagnosis is particularly important for providing a timely treatment to patients and a continuous monitoring of diseases. Since infectious diseases cause a majority of mortality and morbidity in developing countries, there is an urgent need for a diagnostic technology to identify symptoms and to prevent the disease from spreading.

Unfortunately, an accurate system usually requires a laboratory setting. Enzyme-linked immunosorbent assay (ELISA) and other methods involving an automatic robotic processing are generally not feasible in low-resource settings [4-6]. The long operation time and the cost of testing are also of great concern. These challenges not only limit practical applications in developing countries, but also limit the development in biowarfare detection and point-of-care personal healthcare service. Point-of-care testing (POCT) is a convenient platform for an efficient, personalized, and near-patient diagnostic at home and at hospitals. Currently available POCT exists for home measurement of glucose, pregnancy, and coagulation efficiency, and this testing will be increasingly used for identifying pre-symptomatic and symptomatic individuals in every doctor's office.

To develop an ideal sensor which is capable of sensitive and specific pathogen detection while retaining an ease of use and independence from complex laboratory instrumentation, a label-free approach seems to be an effective alternative to avoid the cost of labeling reagent, labeling time, and the requirement for professional operators [7, 8]. Of the existing label-free techniques, an optical measurement system, specifically surface plasmon resonance (SPR) technology, is a promising tool to obtain an accurate and high-throughput detection [9-11]. The improvement of nanotechnology in recent decades can solve the cost issue, scale down the instrument, and enable a high-sensitivity SPR detection system. The integration of these systems with high-density microarrays and microfluidic devices provides another advantage in high-throughput detection by measuring a complex set of biomarkers. [12-17].

1.1.2 Surface Plasmon Resonance Sensor

The first documented observation of surface plasmons dates back to 1902 [18], when Wood illuminated a metallic diffraction grating with polychromatic light and noticed narrow dark bands in the spectrum of the diffracted light. This phenomenon was later explained by Fano as the result of surface electromagnetic waves [19]. As more characteristics of the surface waves were studied by Ritchie, Thurbadar, and Otto [20-22], they concluded that surface waves are related to surface plasmon polaritons (SPPs), which propagate along the surface of a conductor, usually a metal. When light excites SPPs, the resonant interaction between the surface charge oscillation and the electromagnetic field of the light constitutes SPPs. Therefore, a loss in the reflectivity was observed as the energy is transferred to the excitation of SPPs [22]. It should be also noted that SPPs are confined on the surface and will gradually attenuate; owing to

absorption in the metal. These unique properties of SPPs give rise to many exciting applications [23].

The excitement of SPPs requires an extra momentum to compensate for the energy difference between incident light and free charges. In the traditional Kretschmann configuration, a prism in the attenuated total reflection mode is used to generate evanescent waves for coupling the incident light to SPPs. Although the prism-based SPR sensor has demonstrated high-sensitivity biomolecular detections [24], the use of prism increases the cost and limits the portability. The complex optical system equipped with tilted light source, prism, and tilted detector also impedes miniaturization and integration in a microfluidic system [21, 25, 26]. In order to scale down the SPR sensor, nanoparticles and nanoscale structures are used to mimic a subwavelength aperture as a way of focusing the electromagnetic field [23, 27-31].

Once excited, the SPP waves will propagate at a metal/dielectric interface, and generate interesting optical spectra collected by spectrometers. The properties of SPPs could be altered by several parameters including metal permittivity, environmental refractive index (RI), the light source, or the structure configuration. This serves as the basis of a SPR label-free biosensing technique. In general, a probe molecule should be conjugated at the metal/dielectric interface first. If other substances are captured by the probe molecule, the RI profile near the interface will be altered and thus generate shifts in intensity, wavelength, and phase shown in spectra.

In recent decades, SPPs have been widely applied in the development of SPR sensors for studying biomolecular reactions [15, 16]. This technique plays a key role in diagnostic, kinetic analysis and therapeutic investigations because SPPs' surface

confinement nature enables a label-free, high sensitivity, real-time, and surface specific detection [32-34]. Due to the high-sensitivity of the SPR technology, it provides a high-throughput alternative not only for applications in diagnostics but also microarray [12-14] and biomolecular sequencing [35].

1.2 Study Outline

This study focuses on applying nanoscale plasmonic materials for SPR technology. The nanoscale structures excite SPPs without the use of a prism, and thus could be applied for a label-free, high-sensitivity, cost-effective and point-of-care sensing technology. Chapter 2 presents a nanoslit array which triggers SPPs by the subwavelength aperture created by e-beam lithography. The configuration of the nanoslit array was tailored for studying the fundamental properties of SPPs and also for optimizing the structure for a diagnostic application. Surface-enhanced Raman scattering (SERS) based spectroscopy was also applied on the nanoslit array to characterize a conjugated biomolecule. To further decrease the cost and increase the efficiency of fabrication, a colloidal templating technology was introduced. Detailed in Chapter 3, this scalable and tunable method creates numerous gold nanopyramids on arrays in a high-throughput fashion. Finite-difference time-domain modeling was used for a better understanding of SPPs on nanopyramids. Biomolecular binding events of antibody and target protein were used to demonstrate the diagnostic application. Chapter 4 reports the same configuration of nanopyramid arrays, where the material is composed of the polymer, ethoxylated trimethylolpropane triacrylate (ETPTA), and a thin layer of gold. This gold-polymer hybrid configuration exhibits the phenomenon of an extraordinary transmission and enables a high sensitivity biosensing by using a transmission measurement system. Both antibody and deoxyribonucleic acid (DNA)

aptamer binding were carried out in this system for a broader applicability. The SERS technique was also applied for the qualitative characterization of biomolecules.

CHAPTER 2
SURFACE PLASMON RESONANCE IN GOLD NANOSLIT ARRAYS

2.1 Background

2.1.1 Surface Plasmon

Surface plasmon polaritons (SPPs), as known as surface plasmon resonance (SPR) generated in plasmonic crystals [36, 37] play an important role in a wide range of applications such as optoelectronics [38-42] and biosensing measurements [43-45].

SPPs are generated from the resonance between light and free electrons at the interface between two materials, where one has a positive permittivity material and another one has a negative permittivity. Gold, silver, and copper have negative permittivity values [20, 46-49], and a dielectric medium such as water has positive permittivity value. Therefore, the combination of both materials can excite SPPs. However, free electrons on these flat metallic surfaces cannot be coupled to light because of different dispersion relations possessed by electrons and light. Specifically, the wave number of light is $\frac{\omega}{c}$, where c is the phase velocity of wave propagation and ω

is the angular frequency. On the other hand, the wave number of SPP waves is

$\frac{\omega}{c} \left(\frac{\epsilon_1 \epsilon_2}{\epsilon_1 + \epsilon_2} \right)^{1/2}$, where ϵ is the permittivity. To match the wave number between free

charges on metal and light, a momentum parallel to the surface is required [21, 24, 26], and it could be achieved by the Kretschmann configuration [24, 25] or a periodic nanostructure grating film [32, 46, 48]. In the Kretschmann configuration, a metal is placed against a prism which generates evanescent waves parallel to the thin metal film and excites SPPs. On the other hand, the periodic nanostructured grating film creates a diffracted light to fulfill the difference in the wave number.

After the excitation, SPPs propagate at the interface as collective charge oscillations. The properties of SPPs could be altered by several parameters including metal permeability, environmental refractive index (RI), the light source, or the structure configuration. Therefore, biomolecular binding events that change the RI profile near the interface will modulate SPPs [50, 51], and this mechanism gives rise to a label-free, high sensitivity, real-time and surface specific sensing technique. This technique is also known as SPR sensing or SPR sensor because of the resonance property, and it has demonstrated applications in diagnosis, drug discovery, and proteomics' research [14, 16, 52-54].

2.1.2 Substrates for Surface Plasmon Resonance

Although the Kretschmann configuration is commonly used in SPR sensors, the use of prisms increases the cost and limits the portability. To develop a cost-effective, portable and high throughput apparatus, various types of metallic nanostructured grating film and nanoparticle conjugated substrates are used to exhibit localized surface plasmon resonance (LSPR) [36, 55-60]. However, the stochastic separation between neighboring nanoparticles that significantly affects LSPR impedes the sensing reproducibility. On the other hand, periodically patterned nanostructures draw great attention due to their highly engineered structures and higher reproducibility.

These grating films exhibit interesting optical properties such as the extraordinary transmission due to the focusing effect by the subwavelength aperture [48, 61-63]. On these plasmonic nanostructured substrates, several system factors can vary the focusing effect and therefore alter optical properties in transmission, reflection, and surface-enhanced resonance Raman scattering (SERS) spectra [51]. These factors

include RI of dielectric medium, temperature, nanostructure geometry, light incidence angle, and metal thickness, etc. The SPR biosensors particularly transduce the refractive index changes to shifts in optical spectra. It is well known that optimizing these biosensors for the greatest sensitivity to RI changes is very challenging because many factors are also involved in this system. In this work, a series of plasmonic grating substrates with different periodicity were created to compare the different properties generated on the individual grating geometry. The periodicity was chosen as a key variable because of its importance in affecting the spatially coherent geometry and optical spectra.

The plasmonic grating structure studied here is a periodic gold nanoslit array in a size of $150\ \mu\text{m} \times 150\ \mu\text{m}$. These arrays offer the opportunity for high packing density of sensing elements and easy integration with microfluidic devices [13, 14, 64]. To create a highly engineered substrate, a nano-pattern writing system was used to pattern the geometry of the periodic gold nanoslit array. This tunable nanofabrication enables the creation of a desired amount of SPP peaks and dips in the spectra under specific coupling conditions. The sensing apparatus was built on a conventional inverted microscope with light incidence along the surface normal for collecting the transmission spectra. Compared with a tilted light incidence, a straight light incidence used here is considered to improve the portability and the integration with high-throughput image-based devices. The transmission spectra show that gold nanoslit arrays exhibit several types of resonance including Bloch wave SPPs (BW-SPPs) [47], Wood's anomalies [65, 66], LSPR coupling, and slit-slit interference.

2.1.3 Multispectral Analysis

As mentioned in 2.1.1, the excited SPPs are very sensitive to RI changes generated by biomolecular binding events, and this mechanism gives rise to a label-free, high sensitivity, and real-time SPR sensing technique. The plasmonic grating film is used here to improve the portability compared with Kretschmann configuration. To achieve such a high sensitivity as the Kretschmann configuration, the multispectral analysis [37] was utilized on gold nanoslit arrays to integrate shifts in both transmission and wavelength shown in spectra. This analysis offers advantages of capturing the total peak and dip shifts in spectra and increasing the sensitivity of plasmonic crystals such as nanohole arrays and nanoparticles substrates. However, this analysis method does not increase the sensitivity much on the plasmonic crystals that generate a single peak in spectra because the calculated amount of shift is not significant enough. As a result, only a limited number of plasmonic crystals that generate several SPP peaks and dips could take advantage of the multispectral analysis.

Owing to the multiple resonant spectroscopic peaks and dips generated on the gold nanoslit arrays, a multispectral analysis is perfect to maximize the sensitivity. Still, the degree of the maximization depends on the slit periodicity since the amount of spectroscopic peaks and dips is related to the periodicity. This study also compares the RI sensitivity calculated by a multispectral analysis on a series of nanoslit arrays with periodicity ranging from nm to μm . This comprehensive comparison and optimization give an insight in designing the nanostructure geometry for the application of biosensors that detect RI changes induced by the biomolecular binding events.

2.1.4 Biosensing Application

The optimization procedure is essential to obtain an optimum periodicity for a higher RI sensitivity which results in a high sensitivity biosensor. Biosensors are used to study biological interactions and allow us to understand the mechanisms of cell signaling, gene expression and drug metabolism. Moreover, biosensors are important for medical diagnosis. Label-free, real-time, and high sensitivity SPR biosensors have demonstrated their powerful applications in studying biomolecular kinetics and diagnosis. However, the well-known prism-based SPR biosensor could only enable a limited number of sensing channels on a chip, and biomolecular reactions are transduced to shifts in wavelength or angle of incidence. To developing a high-throughput detection, surface plasmon resonance imaging (SPRi) can be integrated into a microarray [12, 16], and biomolecular reactions are transduced to changes in the image intensity instead. To increase the sensitivity and signal to noise ratio, the multispectral analysis is used here to integrate changes in both intensity and wavelength position. This method could improve the sensitivity for a high-throughput SPRi system. The optimized geometry obtained in this study may benefit a new generation of SPRi microarray techniques in the future.

2.1.5 Raman Spectroscopy and Surface-enhanced Raman Spectroscopy

Raman spectroscopy is another spectroscopic technique for providing characteristic information about the vibrational and rotational mode in absorbed materials [67, 68]. It relies on a laser light to interact with a material, and excites the molecule from a ground state to a virtual state. After the molecule returns to the ground state, the resulting inelastic Raman scattering causes an alternation of photon energy and gives the

information of absorbed material. Compared with elastic Rayleigh scattering in which emitted photon has the same energy as the incident photon, Raman scattering emits a photon with slightly different energy. Therefore, spontaneous Raman scattering is typically very weak.

SERS was first observed by Fleischman in 1974, when enhanced Raman intensities were exhibited on the surface covered by layers of organic molecules such as pyridine. It is believed that surface plasmons excited by a laser results in a significantly increased signal from adsorbed molecules on metals. Typically, a strong SERS-active system must possess a structure in the range of 5 nm to 100 nm for enhancing the magnitude of Raman cross section. Due to the improvement in nanotechnology, many types of strong SERS-active substrates were fabricated. Applying these substrates in a nondestructive and label-free Raman spectroscopy allows identifications of fingerprints of different biological systems [69-73]. Unlike infrared spectroscopy, SERS can be operated in aqueous systems.

Although nanoparticle substrates play a key role in SERS biomolecular characterization, fabrication of these substrates with a regular and reproducible pattern is very challenging. In this study, e-beam lithography was chosen to fabricate a SERS-active substrate, the gold nanoslit array for a consistent data output. As mentioned earlier in this chapter, the periodicity of nanoslits determinates the degree of the plasmonic effect. Therefore, SERS spectra of nanoslit arrays should also be affected by the periodicity. This study used a common SERS active molecule, benzenethiol, for evaluating the degree of SERS enhancement depending on the slit periodicity. Moreover, an aptamer is also absorbed on the nanoslit arrays for SERS

characterization. The results provide a proof of concept in applying optimized nanoslit arrays for identifying characteristic peaks on the aptamer.

2.2 Experimental

2.2.1 Fabrication of Gold Nanoslit Arrays

The gold nanoslit arrays were fabricated by using electron-beam lithography (LEO 1530) and a reactive-ion etching. A 5 nm-thick titanium (Ti) film and a 130 nm-thick gold (Au) film were deposited on the glass slide by using an electron gun evaporator. After the deposition, a 350 nm-thick poly(methyl methacrylate) (PMMA) resist (MicroChem) was spin-coated on the sample. A field-emission scanning electron microscope modified with a nano-pattern generating system (NPGS) was used to write nanoslits on the PMMA resist. The NPGS could generate arrays of nanoslits with arbitrary spacing and width. The patterns were then transferred to Ti/Au films by using argon sputtering in a reactive-ion etching machine (Plasmalab 80 Plus, Oxford Instruments). The power of the radiofrequency wave in the reaction chamber was 200W. The chamber pressure was 1×10^{-2} Torr, and the flow rate of argon (Ar) gas was 40 sccm. The PMMA resist was then removed by rinsing the sample in acetone for a few hours. To make sure that no PMMA residue remained in the gold nanoslits, the sample was cleaned by using ozone sputtering, put in ultrapure water, and then placed in an ultrasonic bath for 20 min. After the ultrasonic cleaning, the sample was purged dry by nitrogen.

2.2.2 Apparatus for Using the Gold Nanoslit Sensor

A UV-Vis-NIR spectrophotometer (BTC112E, BWTEK) was used for acquiring transmission spectra of the gold nanoslit arrays. Figure 2-1 shows the scheme of the apparatus for the gold nanoslit sensor. Although a tilted excitation light source and detector generate stronger plasmonic effects, a surface normal incidence was chosen

for a future advantage of scaling down the instrument. The surface normal incidence means that the light is parallel to the surface normal line. For maximizing the resonance effect by utilizing a transverse-magnetic (TM) mode, a polarized collimated white light was selected to illuminate the arrays after passing a 10X microscope objective lens. The transmitted light was then focused by a 10X condenser lens and then coupled to a spectrometer through an optical fiber bundle.

2.2.3 Surface-enhanced Raman Spectroscopy

SERS measurements were carried out by using benzenethiol and thrombin binding aptamer. To minimize contamination and enhance the aptamer binding on the sensing surface of the gold nanoslit arrays, the arrays were cleansed by an air-plasma cleaner (PDC-32G, Harrick Scientific) at medium power for 3 min.

The arrays were immersed in a 5 mM benzenethiol in 200-proof ethanol for 45 min and then rinsed by 200-proof ethanol for several minutes. The samples were dried by nitrogen before being put on the Raman spectroscopy. A set of benzenethiol conjugated nanoslit arrays with periodicity ranging from 2 μm to 10 μm were put on Renishaw inVia Raman microscope equipped with a 785 nm high power near infrared diode laser. Before use, a calibration step was run with a silicone wafer sample. Raman spectra of benzenethiol conjugated arrays were collected using a 785 nm laser at 0.5 mW through a 50X objective lens with integration time of 30 s. Spectra were accumulated five times for improving signal to noise ratio.

2.2.4 Bioassay of Surface-enhanced Raman Spectroscopy by Using Aptamer

Thrombin binding aptamer was a generous gift from Dr. Weihong Tan's group in Department of Chemistry at University of Florida. The synthesized thrombin aptamer is

a 29-base single strand oligonucleotides with 5-base spacer as AGT CCG TGG TAG GGC AGG TTG GGG TGA CTT TTT T-SH. The thrombin aptamer was diluted to a concentration of 2 μ M in PBS solution (pH 7.4, 0.137 M NaCl) (BP399-500, Fisher) before adsorption to cleansed nanoslit arrays. All buffer solutions were made with ultrapure water (Millipore). This water contains fewer hydrocarbons and contaminants, which can influence the sensing process. After an overnight incubation, the arrays with aptamer conjugation were gently washed with PBS solution, and then put on Renishaw inVia Raman microscope equipped with a 785 nm high power near infrared diode laser. The control used was the same feature of gold nanoslit array without aptamer conjugation. Spectra were collected by the same method described in 2.2.3.

2.3 Results and Discussions

Different types of resonances appear on gold nanoslit arrays depending on whether slit periodicity is greater or less than 1 μ m. The slit periodicity is the constant spacing between hundreds of slits within an array. To clarify the term, the arrays with slit periodicity greater than 1 μ m is named as a microscale nanoslit array, and the array with slit periodicity less than 1 μ m is called as a nanoscale gold nanoslit array. Both types of arrays can create multi-peaks and dips for higher sensitivity. Understanding the different types resonances on the nanoslit arrays with periodicity ranging from nanoscale to microscale will help design the ideal plasmonic crystals for many applications particularly for biosensor applications.

2.3.1 Periodicity Effects on the Gold Nanoslit Arrays in Microscale Spacing

Figure 2-2 shows a nanoslit array that has 150 μ m long slits distributed within a 150 μ m x 150 μ m array. The distance between adjacent slits is 2 μ m. The transmission

spectra of the microscale gold nanoslit arrays with different slit periodicity from 1 μm to 10 μm are shown in Figure 2-3. The figure shows that an increased amount of the peaks and dips is found in the spectra when increasing the slit periodicity on arrays. This finding is in good agreement with the theory of BW-SPP coupling modes. BW-SPP waves can be pictured as standing waves generated from the coherent superposition of propagating SPPs. Different orders of BW-SPP modes are excited when SPPs resonantly couple with light whose in-plane momentum matches the Bragg coupling condition for the periodic grating. It is also known that the BW-SPP waves are generated on periodic metallic grating such as microscale nanohole arrays, and these waves have a significant influence on the corresponding transmission spectra [47]. Because the nanoslit arrays also have periodic grating structures, the theory of BW-SPP waves is also applied for the nanoslit arrays.

Under a surface normal excitation, the coupling positions of different BW-SPP modes were predicted by [47, 74]:

$$\lambda_{BW-SPP} = \frac{P}{\sqrt{n_x^2 + n_y^2}} \sqrt{\frac{\varepsilon_{Au}(\lambda)\varepsilon_d}{\varepsilon_{Au}(\lambda) + \varepsilon_d}} \quad (2-1)$$

Since our model is one dimensional nanoslit structure, the equation is modified to:

$$\lambda_{BW-SPP,1-D} = \frac{p}{n} \sqrt{\frac{\varepsilon_{Au}(\lambda)\varepsilon_d}{\varepsilon_{Au}(\lambda) + \varepsilon_d}} \quad (2-2)$$

where P is the slit spacing, n is the order of BW-SPP modes, and ε_{Au} and ε_d are the permittivity of gold and dielectric materials e.g. water respectively. By increasing the slit spacing in Equation 2-2, the BW-SPP peaks appeared in a visible spectrum are of a higher order. For instance, on a 2 μm -periodicity array, the 1st order BW-SPP peak

should appear around 2 μm , the 2nd order is located near 1000 nm, and the 3rd order position is calculated to be 700 nm approximately. As a result, the distance between the 2nd and the 3rd order is about 300 nm. On the other hand, for a 4 μm -periodicity array, the BW-SPP peaks appear in the visible spectrum will be at least the 5th or higher order, and the distance between the 5th and 6th mode is about 133 nm. Based on calculations above, the distance between BW-SPP peaks in the visible spectrum of a 4 μm -periodicity array is shorter than the distance between peaks of a 2 μm -periodicity array.

Furthermore, the intensity of transmission spectra also depended on the slit periodicity. Figure 2-3 shows a decreased intensity in transmission spectra while increasing a slit periodicity. It is due to the energy dissipation in a longer slit spacing array, where SPPs launched from one slit are mostly dissipated before arriving at another slit. Therefore, the amplitudes of peaks and dips are decreased.

2.3.2 Periodicity Effects on the Nanoscale Gold Nanoslit Arrays

To investigate the optical properties of gold nanoslit arrays in both microscale and nanoscale, the slit periodicity was further tuned down from 1 μm to 400 nm. These arrays are called the nanoscale gold nanoslit arrays to distinguish from the microscale arrays described in 2.3.1. The transmission spectra were collected from substrates exposed to different concentrations of glycerol in water, which created different environmental refractive indices. Although Figure 2-4 reveals shifts in transmission spectra with different refractive indices, these shifts are mostly implicit in the original shape of spectra determined by slit periodicity. Thus, to clearly identify shifts induced by refractive index changes rather than the changes of slit geometry, baseline spectrum

was subtracted from all spectra shown in Figure 2-5. The baseline transmission spectrum was recorded while the nanoslit array was immersed in a water medium as shown in Figure 2-4. After the subtraction, Figure 2-5 illustrates four peaks that are subjected to the refractive index change. The intensity is significantly decreased once the refractive index is increased.

Interestingly, these SPP transmission peaks in Figure 2-5 can not be predicted by the BW-SPP Equation 2-2 even though this equation predicted the position of transmission peaks in various types of metallic grating films such as gold nanohole arrays [13, 45]. Furthermore, the amount of transmission peaks is more than what BW-SPP equation estimates. It is noticeable that this equation is not enough to explain all the phenomena particularly for structures in a nanoscale. The comparison between spectra of arrays with varied slit periodicity from 400 nm to 800 nm shows that the slit-slit interference [75] influences SPP characteristics of gold nanoslit arrays when the periodicity of these slits is in the nanoscale range.

The slit-slit interference originates in the SPPs localized around slits [76]. Because of the localization effect, each slit acts as a SPP source, and the interference between each SPP source generates certain fringe patterns. These coherent interactions between each slit are called slit-slit interference, and have been shown to propagate further than for a single slit [77]. The similar mechanism is also observed on nanohole arrays. Based on the model of the nanohole arrays, the measured fringe-wavelength is half of the SPP-wavelength. The far-field transmission measurement shows a stronger intensity at the SPP band peak than at a gold intraband transition peak, and the total electric field intensity is related to the periodic aperture interference. Other studies on

nanoslit arrays also observed the same phenomenon that the measured fringe-wavelength of the multiple nanoslit array was about half of the SPP-wavelength [77].

This evidence suggests the existence of slit-slit interference on the nanoslit array.

Another example on nanohole arrays also supports the hypothesis that slit-slit interference plays a significant role on nanoscale nanoslit arrays instead of microscale nanoslit arrays. On the nanohole arrays, the SPP source generated from one nanohole can be coupled with adjacent nanoholes, and this interference effect called hole-hole interferences is crucial for the enhanced transmission effect [76, 78]. However, if there is only an isolated hole or the distance between adjacent nanoholes is larger than the SPP propagating length, the SPPs launched from one nanohole would be mostly dissipated before they could reach the adjacent nanoholes. Under this circumstance, the hole-hole interference is not excited [79]. In summation, since the slit periodicity of the nanoscale gold nanoslit arrays is less than 1 μm , the arrays are able to exhibit the SPP interference; while the SPPs on microscale gold nanoslit arrays dissipates easily before arriving adjacent nanohole.

Since the slit periodicity determines the coupling efficiency of adjacent slits, an interference-modified BW-SPP equation should be used to predict the BW-SPP positions. Figure 2-6 depicts possible BW-SPP positions of a 600 nm-periodicity nanoslit array based on the concept of the interference. By using this modified equation for a 600 nm-periodicity nanoslit array, a number of 600 nm was adopted for P in the Equation 2-2. Then, a number of 1200 nm also accounted for P in the equation as this number originated from coupled interferences between two slits. The calculations continued until P equaled 15000 nm, which came from coupled interferences between

25 slits. After all these calculations, it is found that the common multiple of the slit periodicity and the length of the array exhibited the strongest interference which can be observed easily in the spectrum.

It is concluded from Figures 2-3, 2-4, 2-5 and 2-6 that optical spectra were modified by varied nanoslit geometry. Meanwhile, peaks excited by both of the BW-SPPs and slit-slit interferences shifted by altering the dielectric environment near the metal interface. This serves a basis of applying nanoslit arrays for sensing or other photonic devices.

2.3.3 Observation of Localized Surface Plasmon Resonance on Nanoslit Array

Unlike BW-SPPs and slit-slit interferences, LSPR [27, 57, 80] is sensitive to the geometry changes rather than the refractive index changes. LSPR is non-propagating SPPs that can be resonantly excited on metal nanoparticles and around nanoholes or nanowells in thin metal films [81, 82]. On gold nanoslit arrays, the LSPR is excited by the oscillations between two interfaces across a dielectric cavity/slit [83]. One metal-dielectric interface has electrons coupled to light, and another interface has dipole SPPs induced by the light-SPP coupling happening at the first interface. Figure 2-7 illustrates the light-SPP coupling and dipole SPPs. The LSPR coupling position shown in spectra of the gold nanoslit array is pointed out in Figure 2-8. The position is similar to the simulated result by using a finite-difference time-domain (FDTD) method [84]. From the simulation, the LSPR optical-field was enhanced 33 times higher in the nanoslit cavity compared with remaining surface [33]. This is because the SPP coupling in slits is resonantly enhanced by the edge of the cavity. While the nodes of standing waves are

located at the slit edge, the LSPR positions could be predicted by the cavity resonance equation [85]:

$$m\lambda = (N_{top} + N_{bottom})L + 2N_{slit}H \quad (2-3)$$

where m is an integer presenting the order of LSPR mode, λ is the estimated LSPR position, N_{top} , N_{bottom} and N_{slit} are the effective refractive indices of the dielectric medium, substrate and slit cavity respectively, L is the slit periodicity, and H is the depth (height) of the slit. The general experimental conditions used in Figure 2-8 are $N_{top} = 1$, $N_{bottom} = 1.52$, $N_{slit} = 1$ and $H = 130$ nm. The values of λ calculated by Equation 2-3 are in agreement with the LSPR positions in Figure 2-8.

For the 1st order of LSPR mode on the 600 nm-periodicity array, the value of m and L equals to 1 and 600 nm respectively. Therefore, this mode should appear at 1772 nm, whereas it is beyond the detection limit of the UV-Vis spectrometer. As depicted by Equation 2-3, the position of a higher order of LSPR mode should shift to a lower wavelength in the spectrum. The experimental results in Figure 2-8 prove the same concept as the position of the 3rd LSPR mode on the 600 nm-periodicity array is calculated to be 590 nm. According to Figure 2-6, the baseline-subtracted spectra in different environmental refractive indices are overlapped, and this phenomenon supports the finding that LSPR mode is not sensitive to changes in refractive index.

Equation 2-3 shows that a longer periodicity, L , increases the LSPR peak wavelength position, λ , and spectra Figure 2-6, 2-8, and 2-9 also demonstrate the same result. Comparison between Figure 2-6 and 2-9 shows that the LSPR mode is at a higher spectroscopic wavelength when the slit periodicity is increased from 600 nm to 1 μm . These findings are consistent with results obtained in the reported nanohole arrays.

Despite the strong evidences above, the LSPR peak was not observed on the 400 nm-periodicity array in Figure 2-4 and 2-5, while Equation 2-3 suggested a spectroscopic position of 634 nm. It can be assumed that that a short distance of 400 nm between nanoslits caused disturbances on generating LSPR. It also seems likely that the stronger slit-slit interference of the 400 nm-periodicity array happened to appear in this region, and the slit-slit interference thus disguised the LSPR peaks.

It is concluded that LSPR peaks can be identified in corresponding spectra by using Equation 2-3 utilizing the concept of standing waves surrounding the nanoslit. The baseline-subtracted transmission spectra provided compelling evidence that these LSPR peaks are not sensitive to changes in refractive index. This property is contradictory to the propagating SPPs such as BW-SPP waves and slit-slit interference mentioned above. The same phenomenon is also observed in literature [24]. Nevertheless, LSPR regions were not recognized in the spectra when the slit periodicity was longer than 2 μm . It is logical that these peaks were shifted to a longer wavelength in spectra beyond the detection limit of the spectrometer.

2.3.4 Observation of Wood's anomalies on Gold Nanoslit Arrays

The evidence of the Wood's anomalies (WA) is also obtained in spectra. Wood's anomalies are usually observed in grating structures, which produce a range of diffracted light in successive orders. At some critical wavelength, the diffracted light lies in the plane of the grating and thus produces effects that could not be explained by ordinary grating theory. The prediction for the wavelength positions of WA is [66]

$$\lambda_{\text{Wood's}} = \frac{P}{\sqrt{n_x^2 + n_y^2}} \sqrt{\epsilon_d} \quad (2-4)$$

Since the gold nanoslit arrays here are one-dimensional structures, the modified equation should be

$$\lambda_{Wood's-1D} = \frac{p}{n} \sqrt{\epsilon_d} \quad (2-5)$$

For a 500 nm-periodicity array immersed in water, Equation 2-5 predicted that the 1st order WA should appear at 666 nm, while for a 600 nm-periodicity array, the positions should be at 800 nm. The arrays with the periodicity in microscale also exhibited the Wood's anomalies. The estimated position for the 2nd order WA is 666 nm on a 1 μm-periodicity array, and the 3rd order WA was also identified at 666 nm on a 1.5 μm-periodicity array. In Figure 2-6 and 2-9, WA appears in the region between slit-slit interference.

2.3.5 Refractive Index Sensing by Using Multispectral Analysis

As mentioned before, having the ability to interpret the relationship between slit geometry and optical spectra improves the array designs; particularly for bioassay applications such as the biosensor and the microarray development. These bioassay applications rely on the label-free sensing to the environmental refractive index changes. To enhance the sensitivity, a multispectral analysis is a better approach compared with the conventional method. The multispectral analysis calculates whole spectral alterations which results from shifts in the transmission intensity and the wavelength position by Equation 2-6:

$$R = \int |\Delta(\%T(\lambda))| d\lambda \quad (2-6)$$

where R presents the total response to the alteration. On the other hand, the conventional method monitors changes of a single peak or dip by Equation 2-7:

$$R = \%T(\lambda) \times \Delta\lambda \quad (2-7)$$

Although this type of analysis offers an increase in sensitivity, only a limited number of plasmonic crystals that generate several SPP peaks and dips by multiple plasmonic resonances could take the advantage of the multispectral analysis. Fortunately, the nanoslit arrays exhibit multiple resonances in the spectra as shown above and therefore would be an ideal structure for applying the multispectral analysis to it.

To evaluate the efficacy of the multispectral analysis, the conventional method according to Equation 2-7 and the multispectral method according to Equation 2-6 were both used in Figure 2-10 and 2-11. Figure 2-10 plots the immediate changes in total response versus time, whereas Figure 2-11 displays the variation of the total response to different refractive index solutions on a 600 nm-periodicity gold nanoslit array. The graph of the total response versus the refractive index yields a line whose gradient gives the sensitivity. Compared with the conventional method, utilizing the multispectral analysis improved the sensitivity from 97 %T nm/RIU to 28600%T nm/RIU about 300 times higher. Moreover, the noise shown in the step response graph was reduced so the resolution and the signal-to-noise ratio were improved. Although using multispectral analysis can improve the sensitivity because of the multi-resonances generated on the nanoslit array, different geometries also affect the sensor performance. The following work focuses on the optimization of the nanoslit geometry for higher RI sensitivity by using the multispectral analysis.

Based on the findings above, the propagating SPP peaks including BW-SPP peaks and slit-slit interference peaks are more sensitive to RI changes compared with the LSPR peaks. Therefore, to improve the sensitivity to environmental refractive index

changes, one strategy is to increase the amount of propagating SPP peaks. The more amount of existing propagating SPP peaks can also overlap the LSPR peaks which tends to be less sensitive to RI changes. Although increasing the periodicity can increase the amount of SPP peaks, the SPP energy will dissipate in a longer slit periodicity. In addition, a longer slit periodicity is likely to generate the BW-SPP peaks at a longer wavelength even above the detection limit of the UV-Vis spectrometer. On the other hand, if the slit periodicity is shortened down to a nanoscale, BW-SPP peaks might shift to a shorter wavelength even below the detection limit of the UV-Vis spectrometer. For instance, a 500 nm-periodicity array generates the 2nd order of BW-SPP peak around 250 nm and the 3rd order peak around 150 nm, and both of these peaks are below the detection limit of the spectrometer. Therefore, the best strategy to increase the refractive index sensitivity is neither extremely decreasing nor increasing the slit periodicity, but rather at some optimum separation in between.

To determine the optimal slit periodicity for a higher sensitivity, gold nanoslit arrays with a slit periodicity varied from 400 nm to 15 μm were immersed in different RI solutions for transmission characterization. It is apparent that in all arrays, the peaks were shifted to an increased wavelength, and the transmission intensities were decreased after adding a higher refractive index solution. To minimize the noise from the background, the total response was normalized by Equation 2-8,

$$R_{norm} = \int |\Delta T_{norm}| d\lambda = \int \left| \frac{T_{solution} - T_{baseline}}{T_{baseline}} \right| d\lambda. \quad (2-8)$$

The graph of the normalized total response versus the refractive index yields a line whose gradient gives the sensitivity. Because the unit of the normalized total response is nm, the unit for the sensitivity becomes nm/RIU. According to Figure 2-12, the

sensitivity was improved when the slit periodicity was increased from 800 nm to 2 μm . This is evident that the amount of peaks and dips increases with the longer slit periodicity. However, due to the energy dissipation, the sensitivity was decreased when the slit periodicity was increased from 2 μm to 15 μm . This result is also related to the fact that a higher order of BW-SPP mode should be generated on a longer periodicity nanoslit arrays, and the higher order of BW-SPP mode is more sensitive to RI changes compared with the lower order. This result is observed in many types of plasmonic crystals. For triangular nanoprism arrays, the lower order of dipole resonance which exists at a longer wavelength achieved a higher sensitivity than the higher order quadrupole resonance at a shorter wavelength [60]. Quasi one-dimensional nanoslit arrays also exhibited a higher sensitivity by observing SPP peaks in longer wavelengths because these long-wavelength SPP peaks were generated by the lower orders of SPR-BW modes [74].

In the category of nanoscale gold nanoslit arrays, the highest sensitivity lies in 500 nm- and 600 nm-periodicity arrays. It can be concluded that the strong light-SPP coupling enhanced the transmission shifts, improving the sensitivity due to the counting of the transmission shifts using the multispectral analysis. Interestingly, the sensitivity of 500 nm- and 600 nm-periodicity arrays is the highest when compared with other nanoscale nanoslit arrays such as 400 nm-, 700 nm-, and 800 nm-periodicity arrays. This result could be explained by the property of LSPR discussed above. LSPR peaks appeared at the center of spectra on the 700 nm- and 800 nm- periodicity arrays. Because the LSPR peaks are not sensitive to environmental RI changes, the 700 nm- and 800 nm-periodicity nanoslit array did not exhibit a comparable sensitivity as the 500

nm- and 600 nm-periodicity arrays. On the other hand, 400 nm-periodicity arrays also failed to display a high sensitivity because LSPR peaks play a major role in the spectra. Moreover, the low order of BW-SPP modes is likely to be limited by the detection range of the spectrometer. For example, the 1000 nm-periodicity arrays could have the 4th order of BW-SPP mode at 720nm, while the 400 nm-periodicity arrays have same order at 145 nm beyond the detection limit. This result suggests that either 600 nm- or 2 μm -periodicity nanoslit arrays is a strong candidate for sensing applications.

2.3.6 Influence of Nanoslit Periodicity on SERS Spectra

The periodicity not only affects the sensitivity of the UV-Vis SPR sensing but also SERS sensing. Benzenethiol was used as a SERS active molecule on a 2 μm - and 10 μm -periodicity nanoslit array in Figure 2-13. The spectra indicate that the enhancement only happened on the 2 μm -periodicity nanoslit array but not on the 10 μm -periodicity array. The result is similar to the previous observation from UV-Vis SPR sensing shown in Figure 2-10 where 2 μm -periodicity arrays achieved the best sensitivity and SPR energy decays in the following periodicity. However, Figure 2-14 shows both of 2 μm - and 5 μm -periodicity nanoslit arrays exhibit the SERS enhancement because a reflection mode was used in SERS apparatus, and 5 μm -periodicity array reflected more light to the detector.

2.3.7 Surface-enhanced Raman Scattering Peak Identification of DNA Aptamer

SERS technique enables quantitative fingerprint identifications of varied molecules, and therefore becomes a useful tool for studying structures and conformations of biomolecules. However, the use of SERS-active labels limits the reproducibility and causes potential interference. On the other hand, a strong SERS

enhancement exhibited on the nanostructured substrate allows a label-free SERS sensing, and therefore eliminates the interference from labels, reduces the procedure, and yields a real-time result. To demonstrate the applicability of label-free SERS tool on nanoslit arrays, characterizations of thrombin binding aptamer and thrombin protein are presented.

The DNA aptamer is demonstrated to be useful in many applications. Aptamers are single-stranded oligonucleotides which can fold into three-dimensional structures. Similarly to antibodies, aptamers can bind with other molecules. Briefly, the aptamer selection involves incubating a random nucleic acid library with target molecules. The bound nucleic acid is then detached from molecules and enriched by polymerase chain reaction (PCR) amplification. The enrichment continues for several times to select a strong aptamer candidate with a low dissociation coefficient. Aptamers are distinguished by advantages in higher stability and lower cost compared with other biomolecules such as antibodies or peptides.

Because SERS technique only senses molecular components sufficiently close to the active surface, the aptamer was dried on the nanoslit array after overnight incubation. Figure 2-15 shows the SERS spectra of the thrombin aptamer conjugated on the nanoslit array and the control. Based on Figure 2-15, the SERS peaks at 730, 998, 1098, 1245, 1396 and 1485 cm^{-1} are characteristic SERS peaks of a thrombin binding aptamer. As the nucleobases adenine, cytosine, thymine and guanine all appear in the 27-mer thrombin aptamer, the peak adenine peak at 730 cm^{-1} and the adenine, cytosine, as well as thymine peak at 1485 cm^{-1} were identified. The deoxyribose vibration mode was observed at 998 cm. The strong band around 1396 cm

is likely due to the two different mechanisms lying behind. One is the CH₂ deformation, and the other one is contributed from the ring stretching mode of the guanine. The backbone stretching was also observed at the band around 1098 cm⁻¹. The peak at 1245 cm⁻¹ is possibly attributed to the deoxythymidine.

Figure 2-16 shows the spectra from aptamer alone and a complex of aptamer and thrombin protein. Although characteristic peaks are not shifted after adding thrombin protein, the intensity of a broad band from 600 to 1000 cm⁻¹ is increased. This could be explained by the conformational changes of thrombin binding aptamer induced by thrombin protein.

2.4 Summary

In conclusion, the gold nanoslit array exhibits several types of SPPs including BW-SPPs, Wood's anomalies, LSPR coupling, and slit-slit interference. This chapter particularly studies the relationship between slit periodicity and corresponding optical properties. As the array owns the superior tunable feature, a wide range of arrays from nanoscale to microscale were studied. The direct observation of several types of SPPs allows the development for different applications. To determine the most suitable slit periodicity for a higher sensitivity, the performance of gold nanoslit arrays having a slit periodicity varied from 400 nm to 15 μm was evaluated. Among all the arrays, the highest sensitivity lies in 500 nm-, 600 nm-, and 2 μm nanoslit arrays. Furthermore, a multispectral analysis improve sensitivity and signal-to-noise ratio. In the end, SERS also demonstrated a strong enhancement effect in the gold nanoslit arrays. As SERS is a useful method to identifying characteristic peaks of specific molecules, DNA aptamer was utilized for peaks identification. As a result, multiple peaks were illustrated in

spectra compared with the control. A conformation change was also observed by adding thrombin protein.

TM polarized light

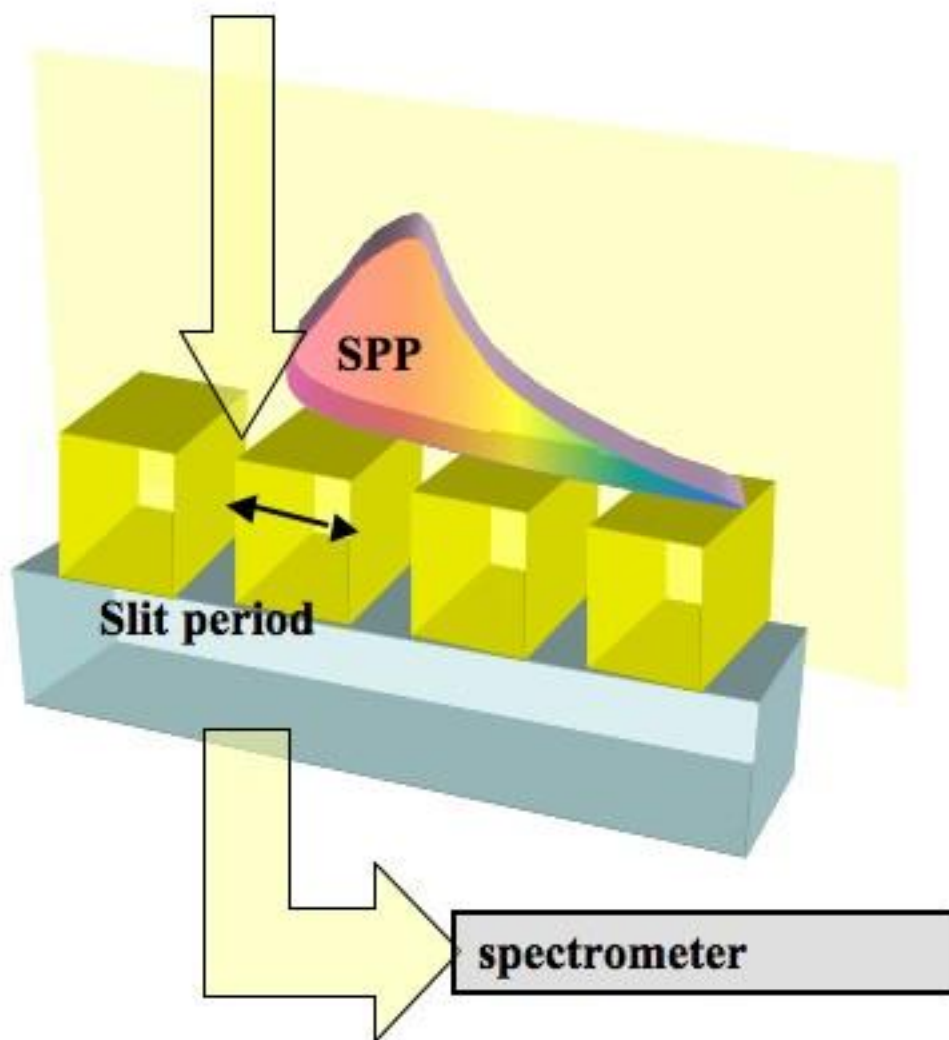


Figure 2-1. The scheme of gold nanoslit array sensing apparatus.

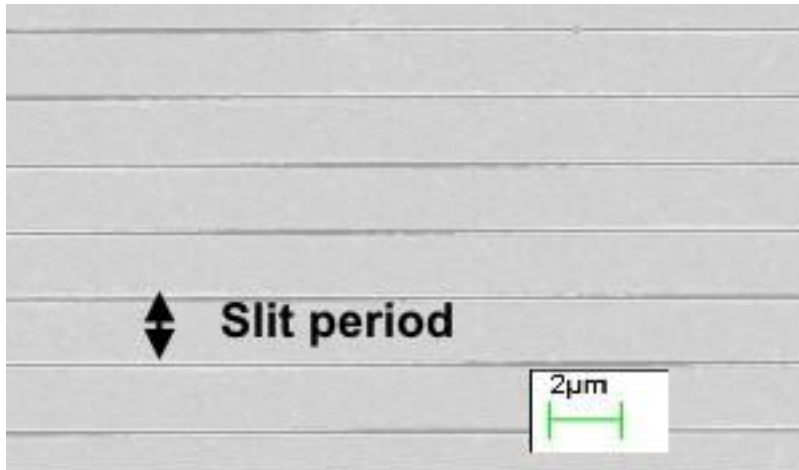


Figure 2-2. The SEM image of a 2 μ m-periodic gold nanoslit array.

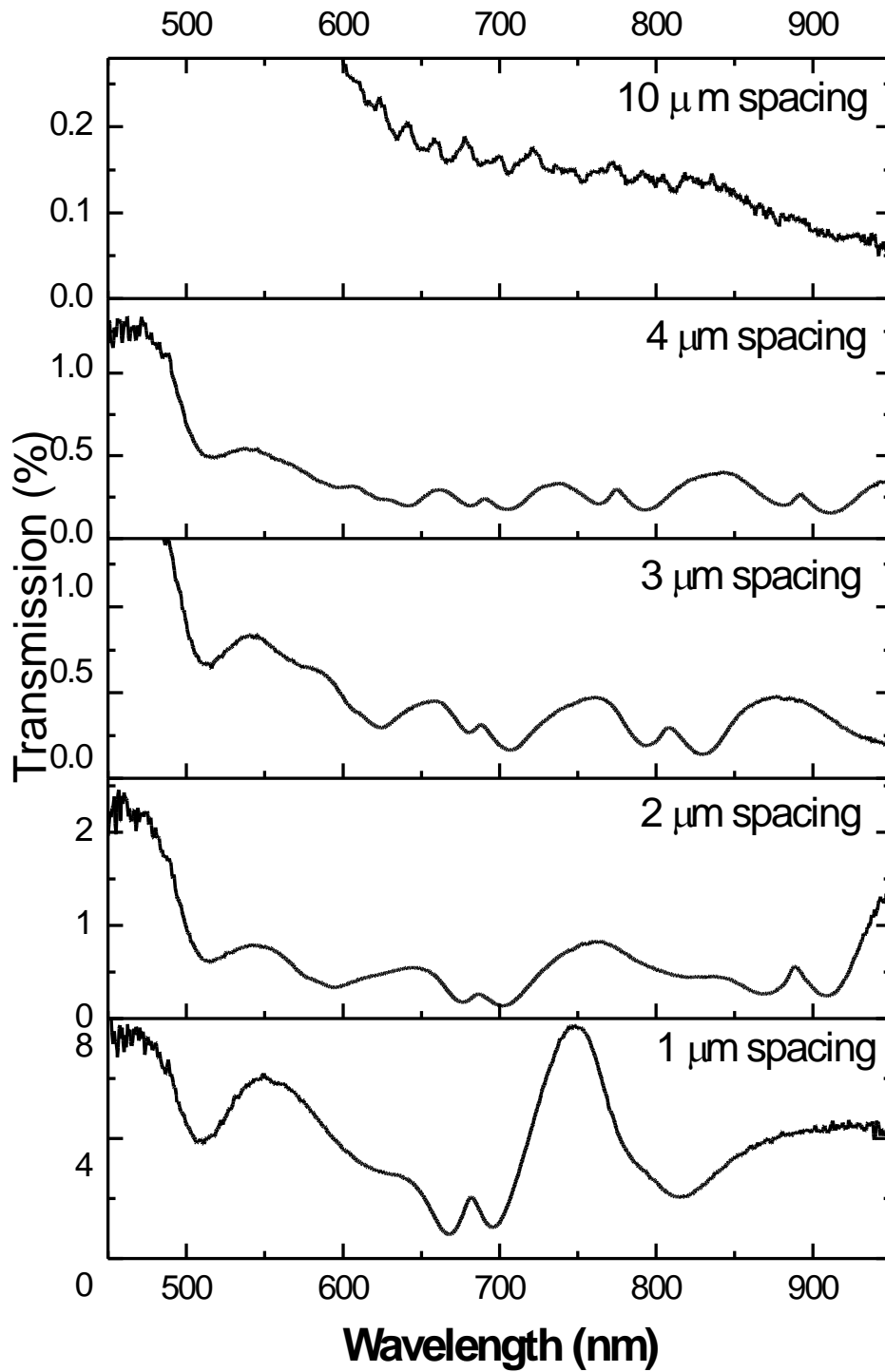


Figure 2-3. The transmission spectra of the microscale gold nanoslit arrays with different periodicity in water.

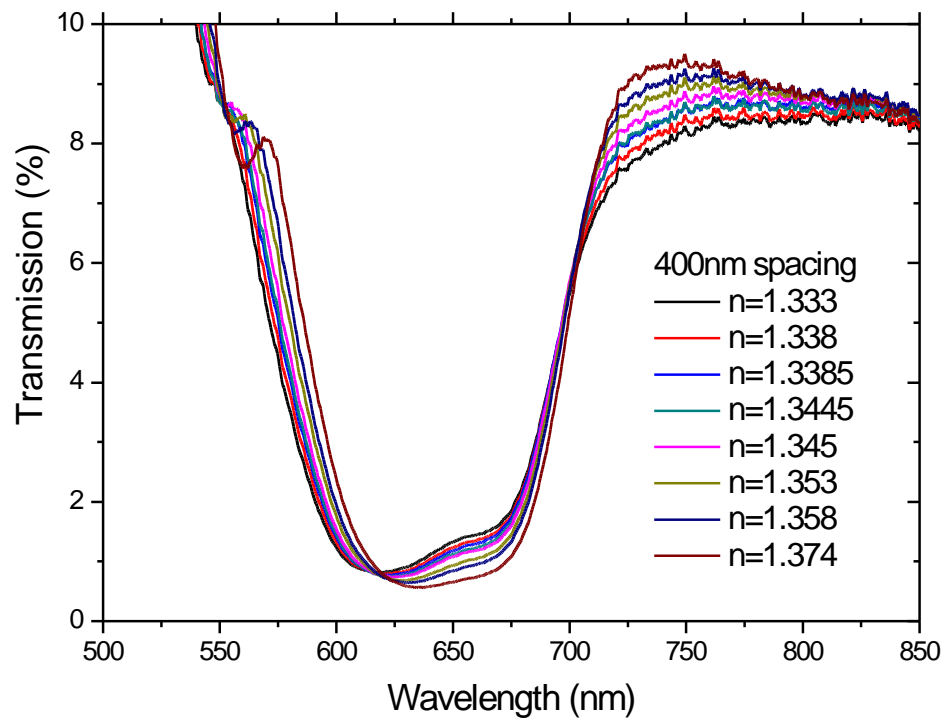


Figure 2-4. The transmission spectrum of the 400 nm-periodicity gold nanoslit arrays which is one of a class of nanoscale gold nanoslit array immersed in different refractive index solutions.

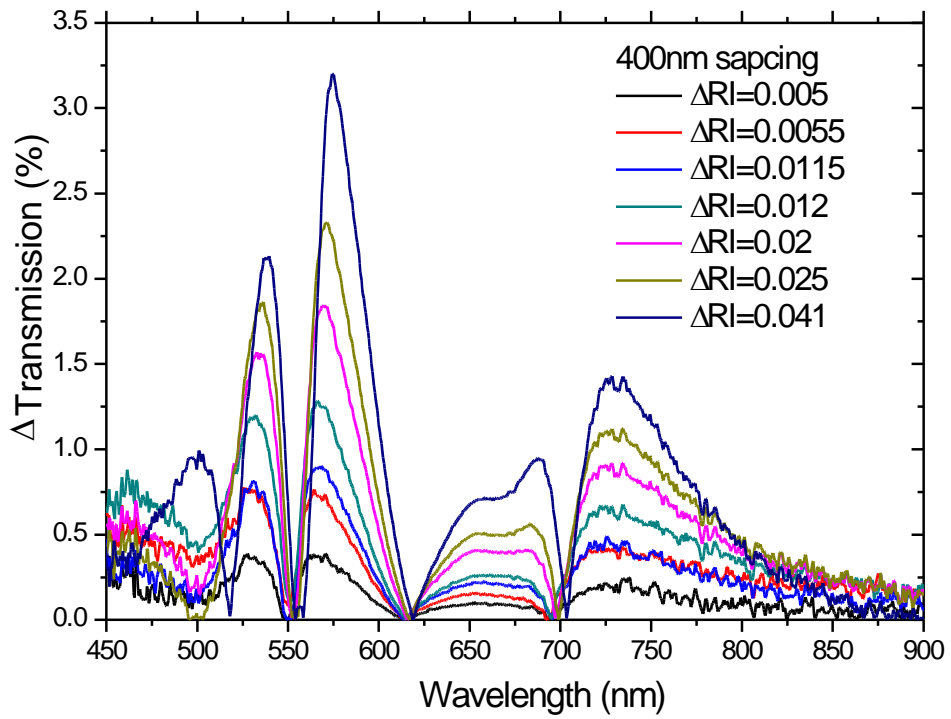


Figure 2-5. The baseline-subtracted transmission spectrum of the 400 nm-periodicity gold nanoslit arrays.

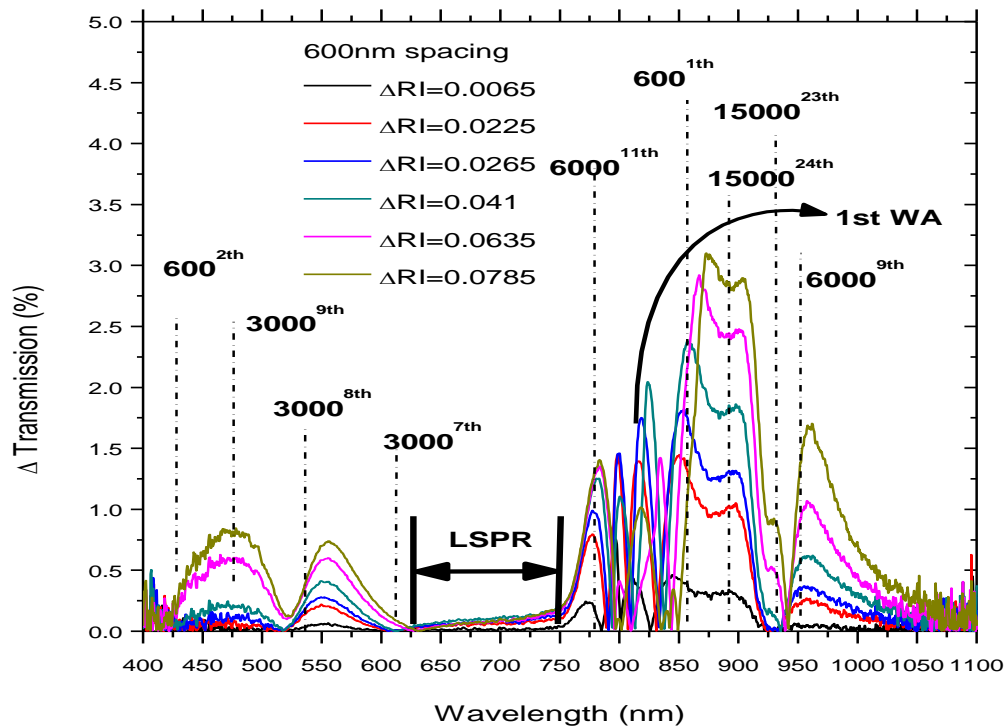


Figure 2-6. The baseline-subtracted transmission spectrum of the 600 nm-periodicity gold nanoslit arrays showing the excitations of the slit-slit interference, LSPR coupling and Wood's anomalies. The positions of these excitations can be predicted by equations

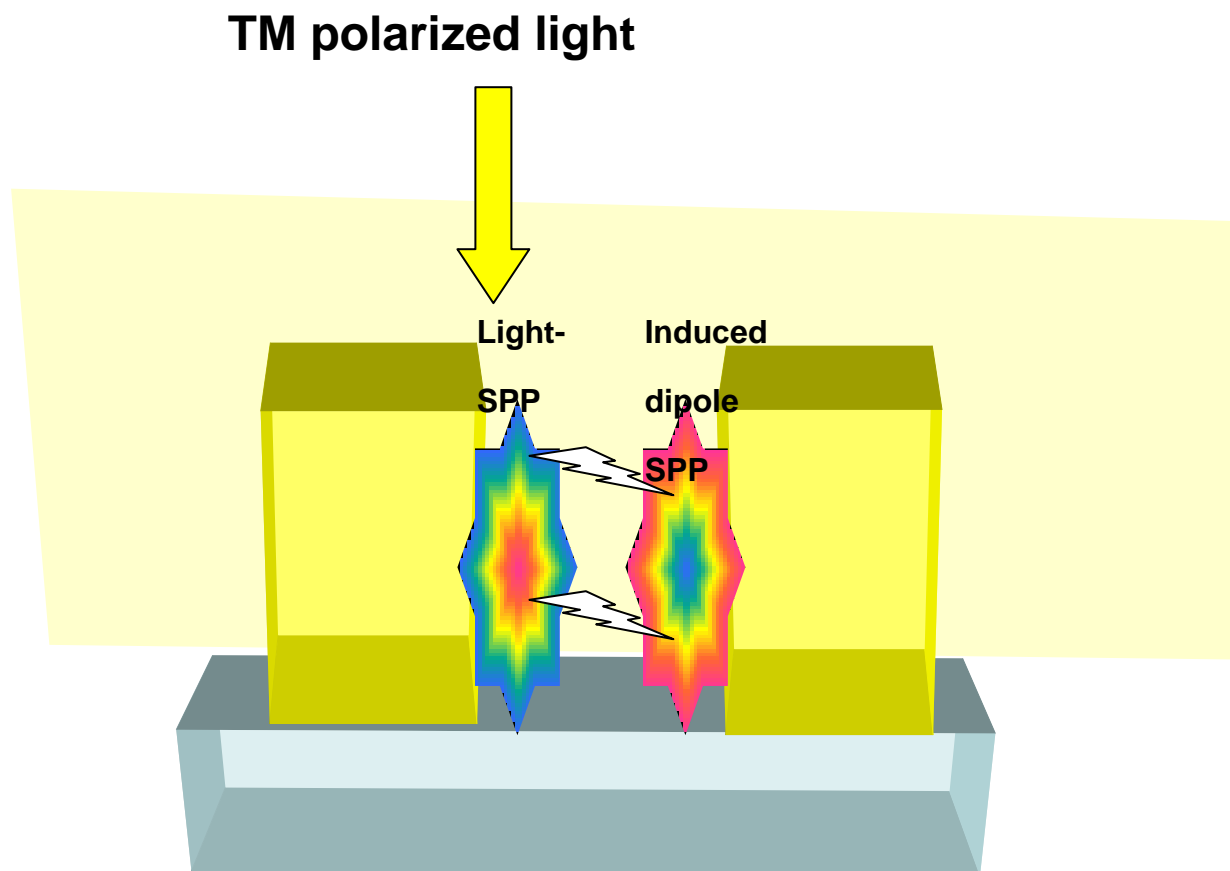


Figure 2-7. The configuration of light-SPP coupling and induced dipole coupling.

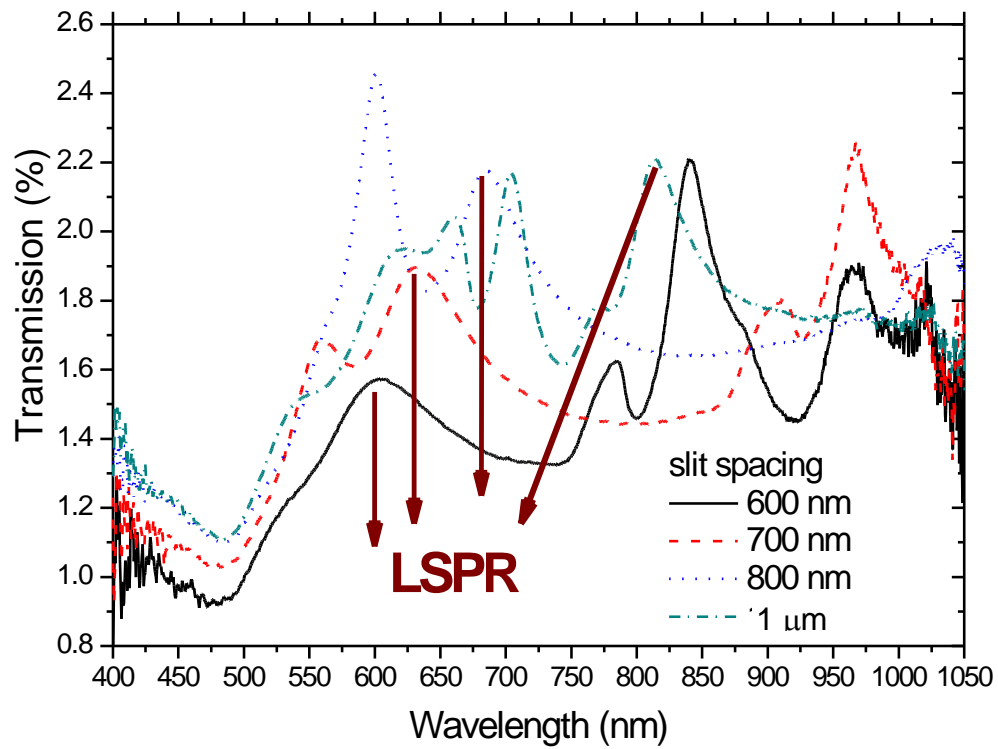


Figure 2-8. The transmission spectra of the nanoscale gold nanoslit arrays showing the LSPR region.

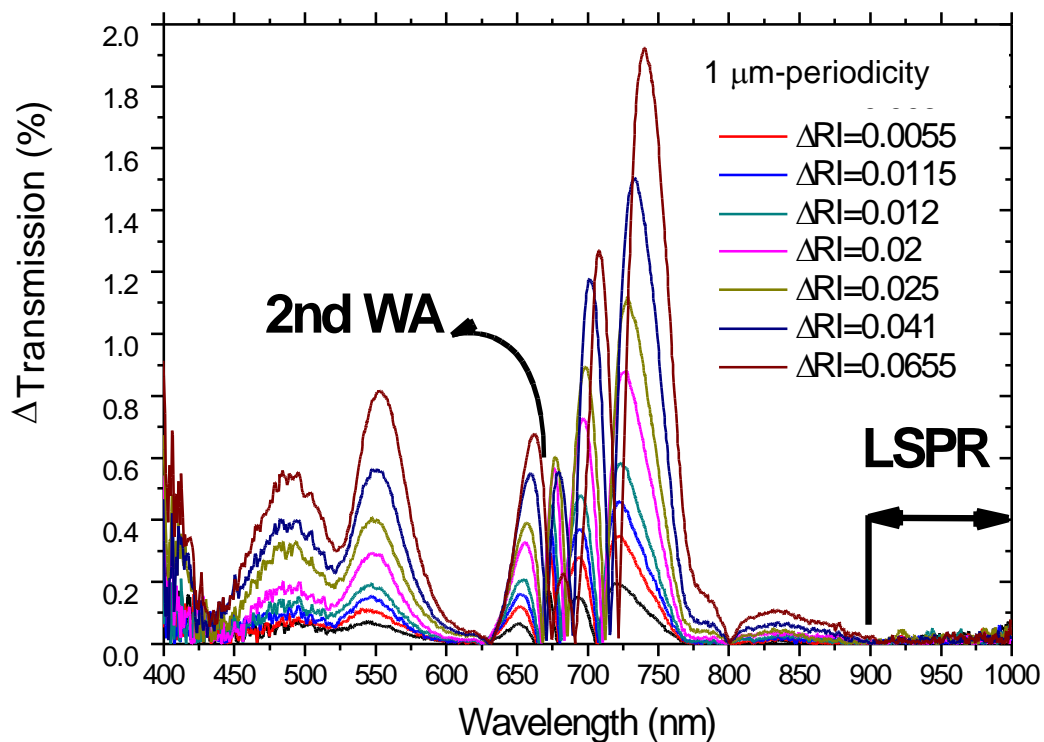


Figure 2-9. The transmission spectrum of the 1 μ m-periodicity gold nanoslit arrays showing the LSPR and Wood's anomalies. 2nd WA represents the second order of Wood's anomalies.

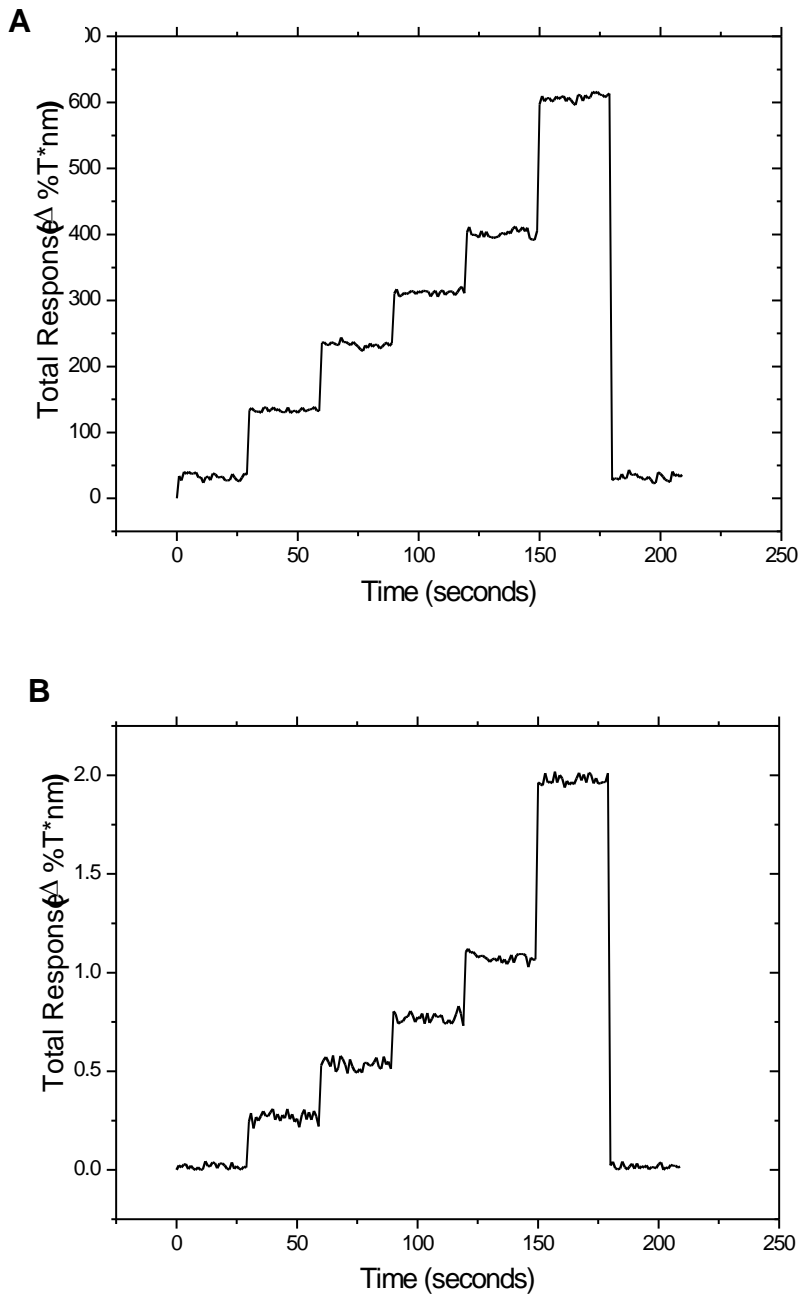


Figure 2-10. Step response by adding different refractive index solutions. A) The amount of shifts in wavelength and intensity yielded a value for total response by the equation of a multispectral analysis. B) The value for response was calculated by a traditional analysis method rather than a multispectral analysis. By using the traditional method, only a single peak was chosen for monitoring the amount of shifts.

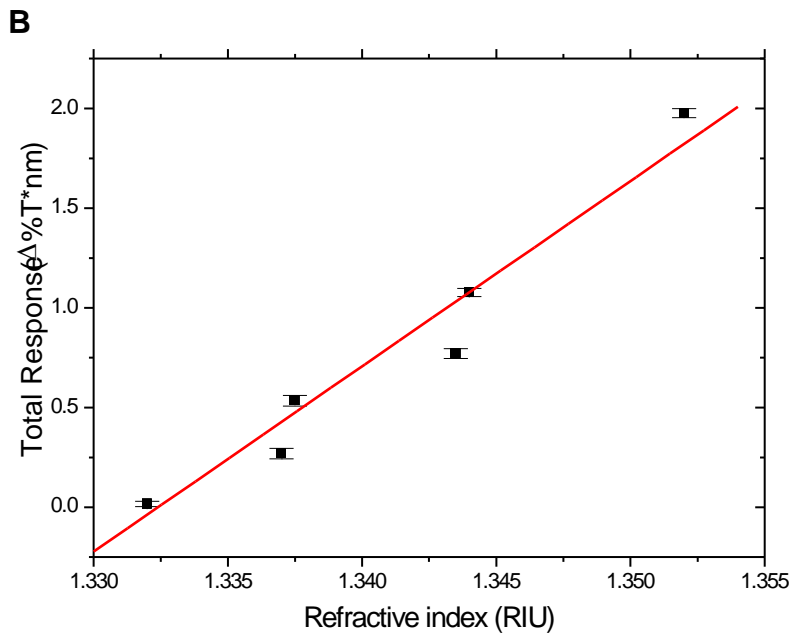
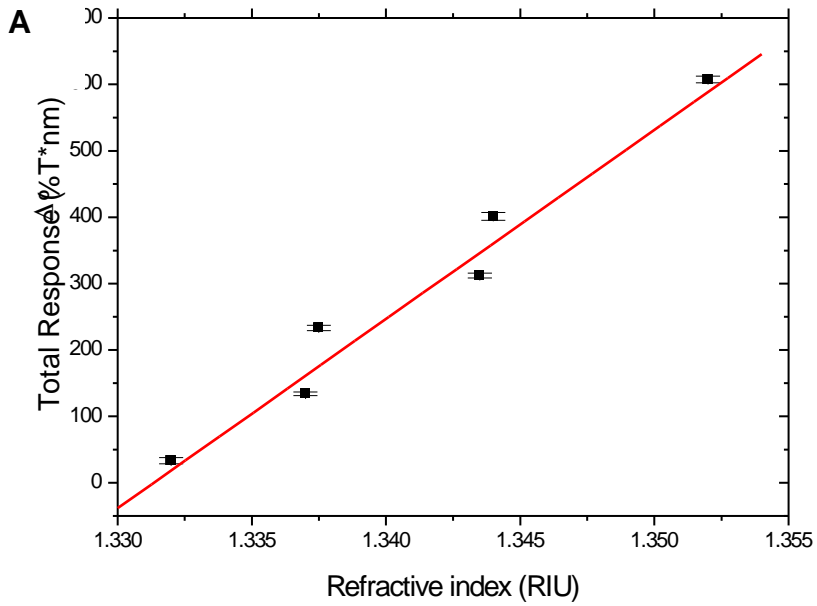


Figure 2-11. A plot of total response versus varied RI from multiple runs. A) The sensitivity is $28500 \Delta T^*nm/RIU$ by using a multispectral analysis. B) The sensitivity is $97 \Delta T^*nm/RIU$ by using a common analysis method.

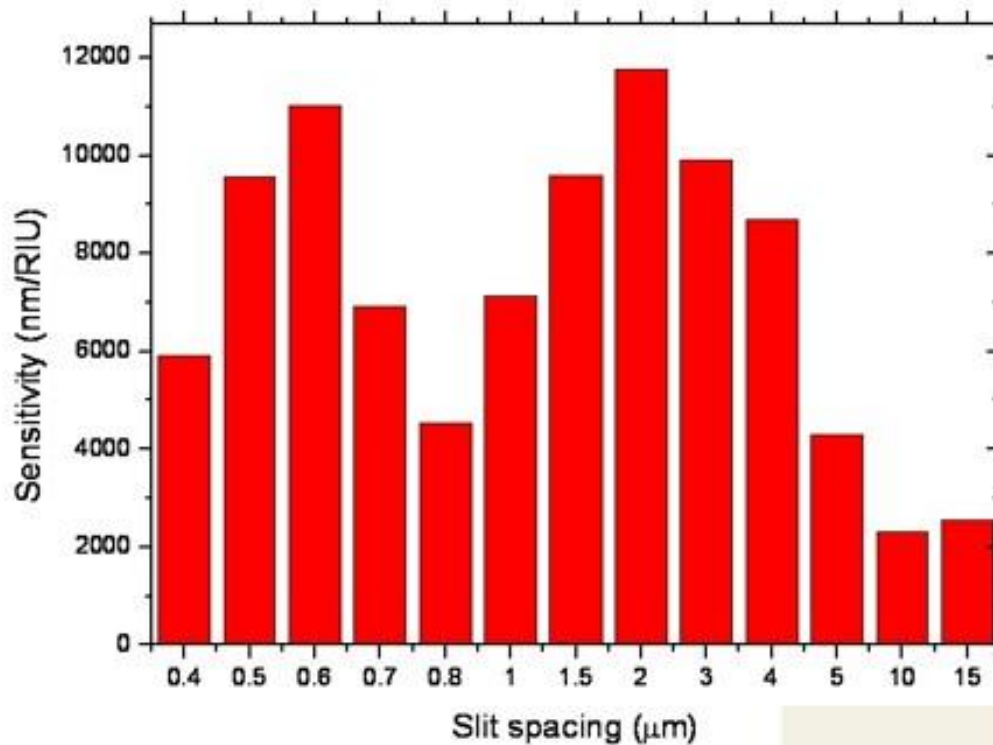


Figure 2-12. The measured sensitivity comparison in the gold nanoslit arrays according to different slit periodicity varied from 400 nm to 15 μm . The sensitivity was calibrated from the graph that yields a line between normalized total responses versus refractive index variation.

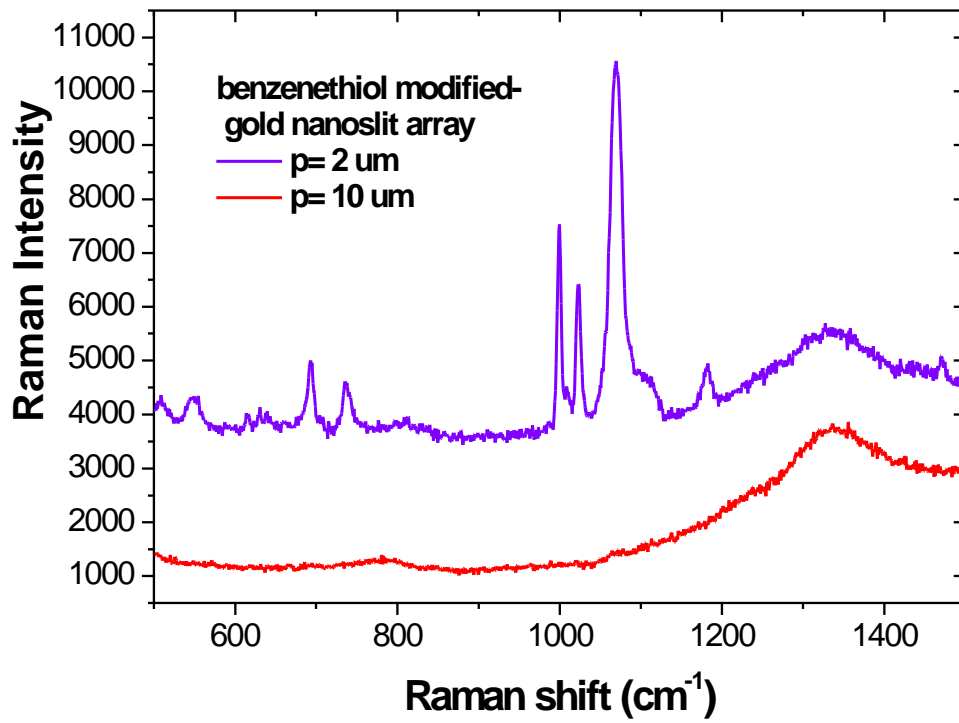


Figure 2-13. The SERS spectra of the gold nanoslit arrays modified with benzenethiol.

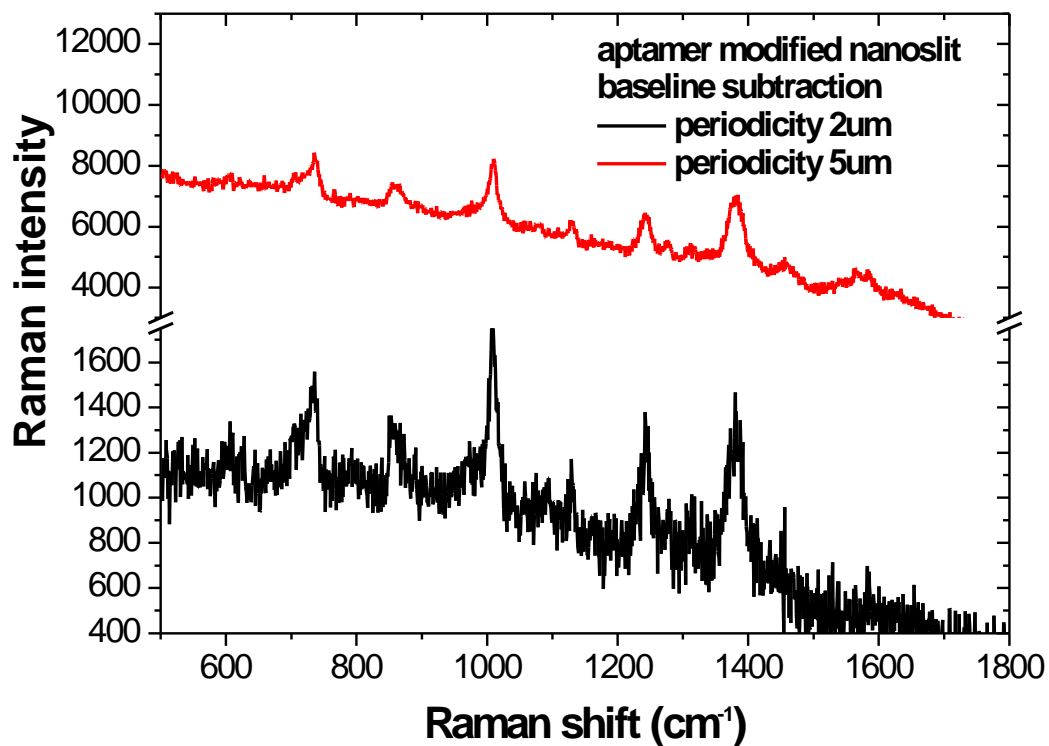


Figure 2-14. The SERS spectra of aptamer conjugated on the nanoslit array with slit periodicity 2 μm and 5 μm respectively.

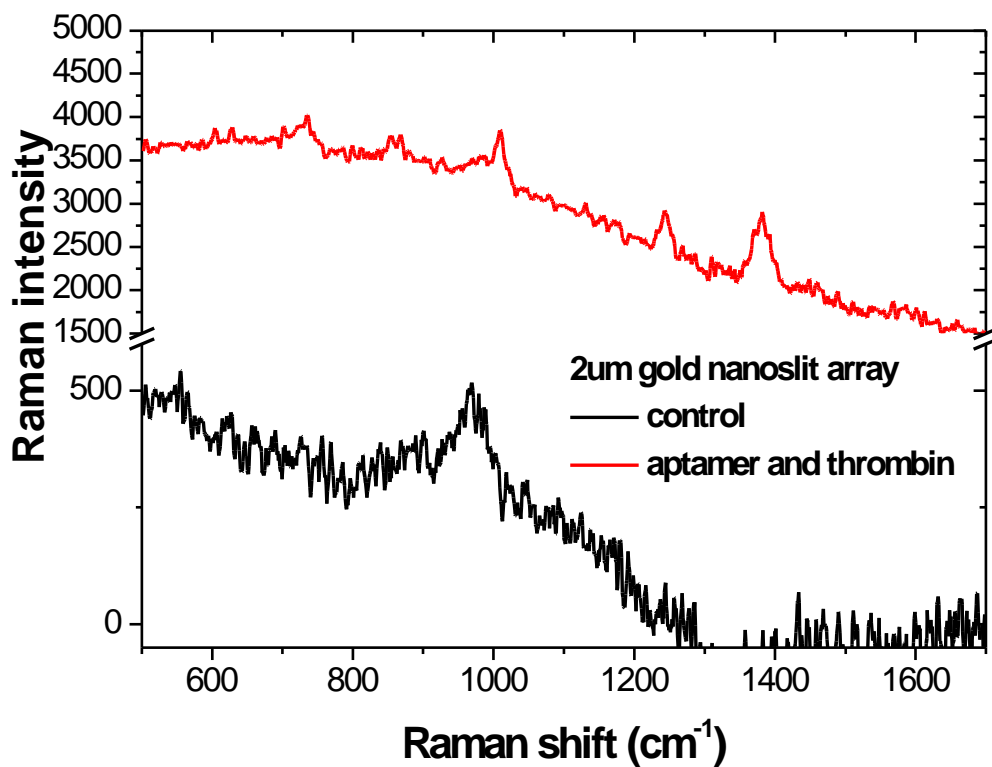


Figure 2-15. The SERS spectra of aptamer conjugated on the 2 μm-periodicity nanoslit array compared with control.

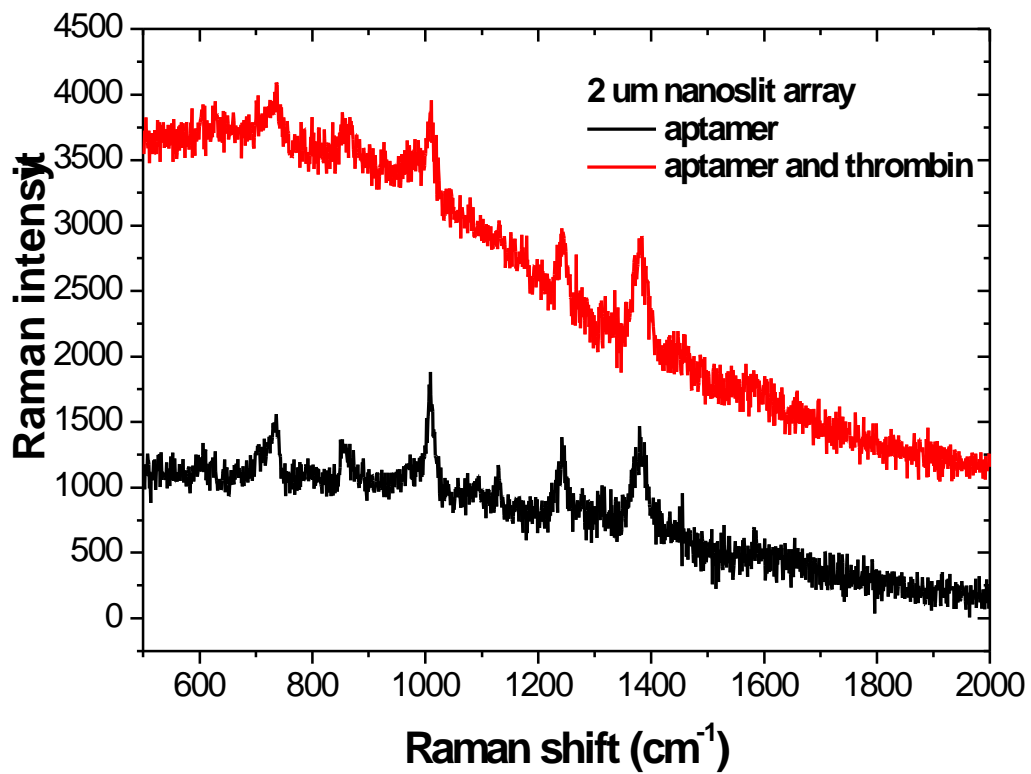


Figure 2-16. The SERS spectra of aptamer conjugated on the 2 μm -periodicity nanoslit array before and after adding thrombin protein.

CHAPTER 3 SURFACE PLASMON RESONANCE IN GOLD NANOPYRAMID ARRAYS

3.1 Background

3.1.1 Gold Nanopyramid for Label-free and Real-time Biosensing

In Chapter 2, the effect of SPPs on nanoslit arrays was demonstrated by using two spectroscopic methods, UV-Vis transmission spectroscopy and SERS, and the periodicity-dependence was extensively discussed. In Chapter 3, the unique contribution of SPPs to label-free biosensing is discussed, particularly for gold nanopyramid arrays. Gold nanopyramid arrays also exhibit SPP waves that propagate along a metal/dielectric interface and can be pictured as a traveling charge density wave on the surface of a metal [23, 86]. The coupling of incident light with free electrons in metal forms SPPs that are essentially confined to the metal/dielectric interface, leading to a strong concentration of electromagnetic field.

The SPR technique which results from SPPs is of great importance for monitoring binding events in biological systems because it offers a direct and label-free platform for rapid screening test [54, 81, 87-91]. This is because the confined SPPs are very sensitive to any changes on this interface. The adsorption of molecules to a metal surface significantly changes the oscillation of SPPs, and thus automatically results in the modulation of light output without any label reagents. The modulation could be monitored by several types of interrogations such as the excitation angle, intensity, and phase in reflection or transmission spectra shown in Figure 3-1 [24, 54]. Compared to other immunoassays, such as enzyme-linked immunosorbent assay (ELISA) and radioimmunoassay [92], the SPR technique is highly promising for rapid and sensitive biosensing because the label-free and real-time characteristics of SPR sensors shorten

the sample preparation time, minimize the interference of conjugating radioactive or enzyme labels, and enable direct analyte detection without a sandwich format [54, 81, 93].

To generate SPPs, the difference in the momentum of incident light and SPPs must be compensated [23]. In the traditional Kretschmann configuration of the attenuated total reflection method, a prism is used to couple the incident light to SPPs [24]. However, the bulky experimental setup impedes miniaturization and integration in microfluidic systems [94]. The exploitation of LSPR around metal nanoparticles is favorable for developing planar on-chip-based sensors [44, 95]. However, the stochastic separation between neighboring nanoparticles that significantly affects LSPR impedes the sensing reproducibility. Periodically patterned nanostructures, which support both localized and propagating SPPs, therefore draw great attention due to their high reproducibility [95-98].

We developed a scalable bottom-up colloidal self-assembly technique for generating wafer-sized periodic gold nanopyramids with nanoscale tips as an efficient surface-enhanced Raman scattering substrate [99]. Unlike top-down techniques such as nanolithography technologies, this bottom-up method provides a simple, cost-effective, and efficient method for nanofabrication. The spin-coating technology could generate a wafer-scale pattern employed as a mold for nanopyramids replicates. It is believed that the periodic structures and the sharp tips of gold nanopyramids enhance the resonance and thus could be utilized as sensitive SPR sensors for chemical and biological sensing. Although e-beam lithography can develop the same type of

sophisticated structures, the drawbacks in cost and time limit its potential for a point-of-care diagnostic application.

3.1.2 Tilted Angle and Vertical Reflection Modes

A tilted angle reflection mode was first adapted for the biosensing applications. The angle of incidence was set as 45° to generate diffracted lights for bridging the momentum between light and SPPs. Once SPPs are excited, the biomolecule binding event happening at the sensor surface will result in spectra shifts. Later, the angle of incidence was set to 0°, parallel to the surface normal. The path of the light is depicted in Figure 3-2 by using simulation package software, Lumerical Solutions FDTD software. This method offers advantages over the tilted angle setup in many aspects. Firstly, the tilted angle setup requires a careful path alignment by using optics extensively, and therefore limits the development of a portable sensing apparatus. Moreover, when the tilted light enters an interface such as air and water, the refractive index of respective medium determines the degree of refraction stated by Snell's law.

$$n_1 \sin \theta_1 = n_2 \sin \theta_2 \quad (3-1)$$

Since the angle of refracted light contributes to the light probing area on the sensor surface, different refractive index of solutions alters the probing area, and causes the instability. While changing buffers is common procedure in the biosensing protocol, this instability is likely to produce false positive results even without biomolecular binding events. Lastly, the vertical incidence setup prevents the image deformation when using an image-based sensing, and therefore enables a future application in detections in a high-throughput and image-based SPR sensing. The simulated results provided the evidence of the enhanced electromagnetic field

surrounding the nanopylramids. This finding suggests the use of nanopylramid arrays for a high-sensitivity, low-cost, real-time and label-free sensing technique.

3.1.3 Finite-difference Time-domain Simulation (FDTD)

FDTD simulation is a numerical solution of Maxwell's equations useful for modeling complex geometries. This method solves Maxwell's equations discretely in time, and offers insight into a variety of materials for numerous types of applications. This modeling has been conducted to complement the optical measurements. The simulated results also provided evidence of the outstanding electromagnetic field enhancement in the nanopylramid array.

3.2 Experimental

3.2.1 Fabrication of Gold Nanopyramids

Periodic gold nanopylramids were fabricated by a simple templating technology using spin-coated monolayer colloidal crystals as structural templates. This technology is well-developed by Dr. Peng Jiang's laboratory in Department of Chemical Engineering at University of Florida. Monodispersed silica colloids are dispersed in UV-curable Ethoxylated trimethylolpropane triacrylate (ETPTA) (Sartomer) to make final particle volume fraction of 20%; 2 wt % Darocur 1173 is added as photoinitiator. The silica-ETPTA dispersion is dispensed on a 3-acryloxypropyl trichlorosilane (APTCS)-primed (100) silicon wafer and spin-coated at 8000 rpm for 6 min on a standard spin-coater, yielding a hexagonally ordered colloidal monolayer. The monomer is then photopolymerized for 4 s using a Pulsed UV Curing System. The polymer matrix is fully removed using a reactive ion etcher operating at 40 mTorr oxygen pressure, 40 sccm flow rate, and 100 W for 4 min. A 30 nm mask of chromium is deposited on the wafer using sputtering deposition at a deposition rate of 1.6 Å/s. After the wafer is then rinsed

by deionized water and rubbed with a cleanroom Q-tip to remove templating silica microspheres, chromium nanoholes were generated on the wafer.

To facilitate anisotropic wet etching, the wafer was immersed in a freshly prepared solution of 62.5 g KOH, 50 ml of anhydrous 2-propanol, and 200 ml of ultrapure water at 60 °C for various durations. Inverted pyramid pit was generated within each nanohole. The wafer was then rinsed with deionized water and then wet etched with a chromium etchant (type 1020, Transene) to remove the chromium template. The etched wafers show iridescence under white light illumination.

To create a nanopyramid array in gold, we sputtered the wafer with 500 nm of gold at a deposition rate of 5 Å/s. The layer of gold on the surface of the wafer can be easily peeled off with Scotch tape (3M), yielding a non-close-packed nanopyramid array in gold. To separate the metallic nanopyramid arrays from the silicon templates in a more reliable and reproducible way, we applied a thin layer of polyurethane adhesive (NOA 60, Norland Products) between the metallized wafer and a glass substrate. The adhesive is then polymerized by exposure to ultraviolet radiation. The silicon wafer templates can finally be peeled off, resulting in the formation of wafer-scale nanopyramid arrays supported on glass substrates.

3.2.2 Apparatus for using the Gold Nanopyramid Sensor

A sandwiching cell, consisting of a gold nanopyramid array adhered to a glass microslide, a glycerol solution (Sigma-Aldrich) and a bare glass microslide, was used to evaluate the optical reflection under the influence of glycerol solutions with different refractive indices. A 2 mm of polydimethylsiloxane (PDMS, Sylgard 184 from Dow Corning) was used as a spacer between two glass microslides for holding glycerol

solutions that were injected by a 250 μm I.D. needle. Prior to each measurement, glycerol solution was injected and extracted several times to remove residual glycerol solution from the last run. A tungsten halogen light source (LS-1, Ocean Optics) and a reflection probe (R600-7, Ocean Optics) were used for the optical measurements. The angle of probe on the top of the gold nanopyramid array was controlled at 45 by using a reflection probe holder (RPH-1, Ocean Optics). The reflected light was collected by a high-resolution portable spectrometer (HR4000, Ocean Optics). The environmental refractive index sensing ability is determined by dividing the spectrum wavelength shift in a “nm” unit by the refractive index changes in a “RIU” unit.

3.2.3 Finite-difference Time-domain Simulation

We used Lumerical FDTD Solution software (from Lumerical Solution, Inc, Canada) in simulations of the electromagnetic field of the nanopyramid arrays. The geometrical parameters of simulated structures were chosen to mimic the experimental situation. The base length, nanopyramid height, lattice spacing, and tip radius of curvature were obtained from the SEM image in Figure 3-3 as 300 nm, 200 nm, 420 nm, and 50 nm, respectively. As the simulation is discrete in space, electromagnetic fields and structural materials are described on a discrete mesh made up of so-called Yee cells. A mesh refinement region (8 nm maximum mesh step in dx, dy and dz) to the simulation was added to make sure the mesh is fine enough to resolve the gold pyramid structures. The excitation source was put at 700 nm above the nanopyramid tip in the format of plane waves with a wavelength range from 500 to 700 nm, a center wavelength of 600 nm, and a 0° polarized angle were used for the modeling.

A 3D simulation region was chosen with a proper boundary condition. Each simulation region on the x-y plane contains two nanopylramids, one pyramid in the center and four quarter-pyramids in the four corners. The simulation region also covers the space along the z-axis from 250 nm below the nanopylramid base to 1000 nm above the nanopylramid tip. Bloch boundary conditions were used in both x- and y-axis of the simulation region because of the periodic structure. The metal boundary condition was set at the bottom for providing a radiation boundary and the perfect matched layers approach was used at the top for providing an absorption boundary condition. The simulated reflection spectra were collected at the zero-order.

To simplify the simulation on the tilted angle setup, the real incident angles at a gold nanopylramid array were calculated by using Snell's law from the incident angle in air (45°) and the refractive indices of air, glass, and liquid as follows: $n_{\text{air}} \times \sin(\theta_{\text{air}}) = n_{\text{glass}} \times \sin(\theta_{\text{glass}}) = n_{\text{liquid}} \times \sin(\theta_{\text{liquid}})$, where n is the refractive indexes and θ is the angle of incidence. As $n_{\text{air}} = 1.00$, $\theta_{\text{air}} = 45.0^\circ$ and $n_{\text{liquid}} = 1.33$, θ_{liquid} is calculated to be 32.1° and the same rule is applied to all testing glycerol solutions with different refractive indices. Only the zero-order signals are collected due to the narrow acceptance angle (24.8° in air) of the reflection probe.

The vertical reflections mode does not require consideration of Snell's law, and the configuration of simulated objects is illustrated in Figure 3-2.

3.2.4 Bioassay of Gold Nanopyramid Sensor

To minimize contamination and enhance the aptamer binding on the sensing surface of the gold nanopylramid arrays, the arrays were cleansed by an air-plasma cleaner (PDC-32G, Harrick Scientific) at low power for 1 min. The gold nanopylramid

array was then treated by Protein A, a protein that resides in the microbial wall of *Staphylococcus aureus*, to enhance conjugation of rabbit immunoglobulin G (IgG) on gold nanopyramid arrays. Lyophilized Protein A (MP Biomedical) was reconstituted to 50 $\mu\text{g}/\mu\text{L}$ with pH 7.4 phosphate buffer saline (PBS) with 0.137M NaCl (Fisher) and stored at -20°C . Prior to use, the stock solution of Protein A was first diluted to 5 mg/mL, then put on a clean gold nanopyramid array sample and subsequently incubated overnight at 4°C . After incubation, the gold nanopyramid array was rinsed three times with phosphate buffered saline (PBS) solution reconstituted from 10X PBS concentrate (BP399-500, Fisher) to wash away un-adsorbed Protein A and incubated with rabbit polyclonal to alcohol dehydrogenase (abcam) at 10 $\mu\text{g}/\text{mL}$ overnight at 4°C . A spectrum was recorded after the incubation. Varied concentrations of alcohol dehydrogenase from yeast (MP Biomedicals) in PBS was then added on the array and incubated for 1 hr at room temperature, followed by three times rinsing with PBS buffer for removing unbound residue. Another spectrum was recorded. After the conjugation of alcohol dehydrogenase, the same array was exposed to 1% casein in PBS (Thermo) to evaluate specificity of the gold nanopyramid sensor.

3.3 Results and Discussions

3.3.1 Fabrication of Gold Nanopyramid Arrays

Figure 3-3 and 3-4 shows tilted SEM images of an array of gold nanopyramids replicated from the silicon template. A simple spin-coating technique enables a fast and scalable method for generating nanostructures by using colloidal particles. A mixture of polymer and 320 nm silica spheres were assembled on the wafer in a long-range hexagonal ordering naturally. These silica spheres then served as the masks for metal

deposition. Once silica spheres were removed, the remaining metal film has numerous nanoholes in a hexagonal ordering, and is ready for the subsequent etching into these nanoholes. The whole process of making the template was finished after inverted pyramid pits were generated within each nanohole.

To create a gold nanopillar array, a thick film of gold was deposited on the template and then peeled off. Figure 3-3 shows the long-range hexagonal ordering of nanopillars results from the property of silica sphere assembly. A magnified SEM image in Figure 3-4 reveals the sharp tips and the smoothness of the nanopillars even though the gold nanopillars were peeled off from the wafer. The template also remained intact for multiple replications.

3.3.2 Gold Nanopillar Sensor in a Tilted Angle Reflection Mode

Since SPPs are localized on the interface of metal and dielectric medium, alterations in refractive index, temperature, material properties, etc. on this surface could change the oscillations of SPPs. This serves as a basis for SPR sensing. The tilted light source used here is easily to generate diffracted light to compensate the momentum of SPPs, and the detection optical probe was also located at the same position due to the design of the probe. To evaluate the sensitivity of the gold nanopillar arrays, reflection spectra were recorded while the array was immersed in various concentrations of glycerol solutions. Different concentrations of glycerol solutions alter the value of refractive index in the SPR sensing region. Therefore, changing concentrations modified the coupling condition of SPR waves, and revealed shifts in reflection spectra. Figure 3-5 shows the reflection spectra obtained from the array immersed in glycerol solutions of different refractive indices. A shift in the

maximum reflection wavelength is observed as the solution refractive index increases. The sensitivity ($\Delta\lambda/\Delta n$) of the nanopyramid array was evaluated to be 239 nm per refractive index unit (nm/RIU), where $\Delta\lambda$ and Δn is alternation of wavelength position and refractive index respectively. The result is favorably comparable to other grating coupler-based SPR sensors.

3.3.3 Finite-difference Time-domain Simulations in Tilted Angle Reflection Mode

A comprehensive analysis from both of the experimental results and theoretical simulations provide a better understanding of this newly developed structure. Figure 3-6 shows FDTD-simulated reflection of plane wave from a gold nanopyramid array with liquid of different refractive indices. A shift of the maximum reflection is observed as the refractive index increases, showing the same trend as the experimental result in Figure 3-5. Figure 3-7 shows a comparison between experimental and theoretical reflection from gold nanopyramid arrays with different tip sharpness. The maximum reflection of the experimental spectrum is closer to the simulation with 10 nm tips while the shape of the spectrum is more similar to the simulation with 50 nm tips. The difference in the maximum reflection may result from difference in geometry between the real gold nanopyramids and the depicted nanopyramids, such as the sharpness of edges and tips. Interference arises when tip radius of curvature is smaller than 10 nm. From the SEM image in Figure 3-4, tip radius of curvature lies in between 10 to 50 nm. Therefore, no interference is observed from the experimental reflection. The broadening of the peak could be caused by the defects in the nanopyramid array. Structural defects such as polycrystalline domains, point and line defects can significantly broaden optical spectrum.

The maximum reflection wavelength of both simulated and experimental reflection with solutions of different refractive indices is summarized in Figure 3-8. Figure 3-8 further shows that the maximum reflection obtained from simulation is 20 to 30 nm larger than that of experiment. The sensitivity of the simulated reflection is calculated to be 314 nm/RIU and is comparable to that of the experimental reflection, which is 239 nm/RIU. The difference in sensitivity can be resulted from the defects and the sharpness of edges in the pyramid arrays.

3.3.4 Gold Nanopyramid Biosensor in Tilted Angle Reflection Mode

We further investigated the biosensing performance of the templated gold nanopyramid arrays by using rabbit IgG to alcohol dehydrogenase and alcohol dehydrogenase, an enzyme to catalyze the oxidation of alcohol. The corresponding normalized reflection spectrum due to the adsorption of anti-alcohol dehydrogenase is shown in Figure 3-9 (black line) with peak wavelength at 595.9 nm. A shift in peak wavelength from 595.9 nm to 602.3 nm is observed after alcohol dehydrogenase is added to the anti-alcohol dehydrogenase-conjugated nanopyramid array. In addition, the detection selectivity was tested by casein, a protein commonly used as a blocking reagent. As expected, the very little binding of nonspecific protein casein didn't cause any significant peak shift (blue line).

3.3.5 Refractive Index Sensing in a Vertical Reflection Mode

To understand the electromagnetic field distribution on the arrays, we used FDTD simulation to model the reflection spectra. Figure 3-2 illustrates the scheme of simulations, where the light source beam was parallel to the surface normal. Figure 3-10 shows the simulated reflection spectra from a gold nanopyramid array immersed in

different RI environments. A red-shift of the maximum reflection wavelength is observed as the refractive index increases. The environmental RI sensitivity is determined from the graph of the value for wavelength shifts versus the amount of altered RI. The line connecting all the points in this graph yields a gradient, which gives the sensitivity reading. The RI sensitivity of the nanopillar array from simulated spectra was calculated to be 176 nm/RIU at the spectrum position near 550 nm and 128 nm/RIU at 665 nm. In addition to the simulation, we evaluate the environmental RI sensitivity experimentally shown in Figure 3-11. The experimental reflection spectra are similar to the simulated spectra, but the experimental spectra have broader peaks. This could result from the fact that simulation setting did not match the experiment perfectly. One difference was the excitation source. The simulation used a 0° polarized angle, but an unpolarized white light was employed in the experiments. Another difference was the integrity of nanopillars. In the simulation, all the nanopillars are designed to be perfectly sharp. However, the real sample has some defects, and the $500 \mu\text{m} \times 500 \mu\text{m}$ light beam used in the experiment might shine on some defects.

The spectrum shift in an altered RI environment was observed in both of simulated and experimental results. Figure 3-11 shows that an increased RI shifted the experimental spectra in three positions including two dips at 525 and 626 nm as well as a peak near 560 nm. The dip near 525 nm was chosen for monitoring shifts in the wavelength because the shape is more defined at this position. The calculated sensitivity was 268 nm/RIU which is similar to the simulated sensitivity. Besides wavelength shifts, the varied intensity in spectra was also related to the RI changes.

However, it should be noticed that the intensity increased in a specific region of spectrum from 575 nm to 625 nm and decreased in the rest from 500 nm to 575 nm.

It is interesting to discover that the position of peaks and dips can be predicted by the BW-SPP equation. This equation is widely applied in nanostructured plasmonic substrates for calculating BW-SPP coupling positions.

$$\lambda_{BW-SPP,1-D} = \frac{p}{n} \sqrt{\frac{\epsilon_{Au}(\lambda)\epsilon_d}{\epsilon_{Au}(\lambda) + \epsilon_d}} \quad (3-1)$$

In Equation 3-1, P is the periodic structure spacing, n is the order of BW-SPP modes, and ϵ_{Au} and ϵ_d are the permittivity of gold and dielectric respectively. The permittivity of the dielectric should be 1.33² in a water medium. The permittivity of gold depends on the monitoring wavelength, and the value was found in the literature. Since the nanopramids are arranged in a 2D periodic structure, the coupling wavelength should be calculated for x- and y- axis individually. Observed from the SEM image, the nanopyramid spacing is 420 nm and $420\sqrt{3}$ nm in the x- and y- axis respectively. Therefore, the calculated 1st BW-SPP coupling position in x-axis is 605 nm which can be identified as the dip shown in Figure 3-11. Although the calculated 1st BW-SPP coupling position in y-axis should appear at 1048 nm, this position is beyond the spectrometer limit. However, we could still observed the 2nd coupling at 524 nm which can be assigned to the dips shown in the spectra.

3.3.6 Finite-difference Time-domain Simulated Electromagnetic Field Distributions

The electromagnetic distribution was further investigated by using FDTD simulation. The calculated electromagnetic field enhancement, $|E_i|^2$, was normalized to the excitation intensity. Figure 3-13 shows the electromagnetic distribution in x-z cross

section, and the resulting simulated electromagnetic field enhancement achieved 200 at the edges around the bottom of pyramids. It can be explained that the pyramid edge created a concentrated and localized SPPs, which are called the hot spot areas. Figure 3-13 shows that these hot spot areas only occupy a limited space, and provides a straightforward illustration of the property of surface confined SPPs. It is believed that the biomolecules bound on these areas will modulate the SPP oscillations dramatically. Figure 3-14 shows the electromagnetic distribution on the x-y plane of nanopyramid tips. Seven concentrated spots in a hexagonal arrangement represent tips of the nanopyramids. The electromagnetic field is tightly confined around the tip and the corresponding enhancement is 50.

In summary, the experimental results demonstrate that the gold nanopyramid arrays are sensitive to environmental RI changes. The simulated spectra and figures further suggest the existence of concentrated SPPs. As concentrated SPPs are more sensitive to environmental changes than weak concentrated SPPs, it is assumed that the biomolecule binding events happening in concentrated SPP areas such as pyramid bottom and pyramid tips produce a dramatic signal.

3.3.7 Gold Nanopyramid Biosensor in a Vertical Reflection Mode

The biosensing performance was demonstrated by using anti-alcohol dehydrogenase antibody for targeting alcohol dehydrogenase. The process involved Protein A modification and followed by anti-alcohol dehydrogenase antibody incubation on the gold pyramid array. After the substrate was put on the apparatus, the baseline reflection spectrum was recorded when the array was immersed in PBS. After the spectrum was stabilized after 30 min, different concentrations of alcohol dehydrogenase

in PBS solution were injected into the flow cell and contacted the anti-alcohol dehydrogenase conjugated on the pyramid surface. Each spectrum was recorded after 30 min incubation. Figure 3-15 shows a significant change in the spectra after adding alcohol dehydrogenase at 0.2 ng/ml. The spectrum conformation was slightly different, and the dip and peak positions shifted to the left, a shorter wavelength. Moreover, the spectrum intensity became lower in the region below 500 nm and higher in the region beyond 500 nm than the spectrum intensity in the beginning. Increasing the concentration of added alcohol dehydrogenase shifted the dip and peak positions as well as the spectrum intensity. Casein, a common blocking protein from milk, was selected as a control reagent, and this protein was diluted in the same buffer as the alcohol dehydrogenase.

After incubated 20 ng/ml of alcohol dehydrogenase on the array and washed away unfound alcohol dehydrogenase, casein was added to the array. Within 30 min of the spectrum recording after adding casein, no substantial changes in the reflection spectrum were observed even though the concentration of casein is 5×10^5 times higher than the concentration of the alcohol dehydrogenase solution. The result suggest that the shifts should mostly relate to the antibody-antigen binding reaction instead of a non-specific binding or a system instability. The intensity change upon the addition of the alcohol dehydrogenase solutions is more significant at a higher wavelength position than at a lower wavelength position in the spectrum. The reason is that the lower order of BW-SPPs appears at a higher wavelength position, and thus enables a higher sensitivity. To associate spectrum shifts to the amount of bound protein. The plot of spectrum shifts at 525 nm versus the amount of bound protein is illustrated in Figure 3-

16. Although the spectrum shift is not significant when the protein's concentration was increased from 2×10^{-9} g/ml to 2×10^{-8} g/ml, it is because the peak fitting statistic method provided by Origin software failed to determine the dip position in the dull shape of the spectrum.

3.4 Summary

In conclusion, a new class of plasmonic crystal was developed to fulfill the need for highly engineered configuration and cost-effective fabricating method. Both of two kinds of excitation, 45° and 0° to the surface normal, generate a spectrum shifts by changing environmental refractive index. FDTD simulation also suggests the same concept in simulated reflectivity and localized electromagnetic field surrounding the nanopyrramids. In addition to the environmental refractive index testing, a specific biomolecule binding reaction was monitored on the gold nanopyramid arrays.

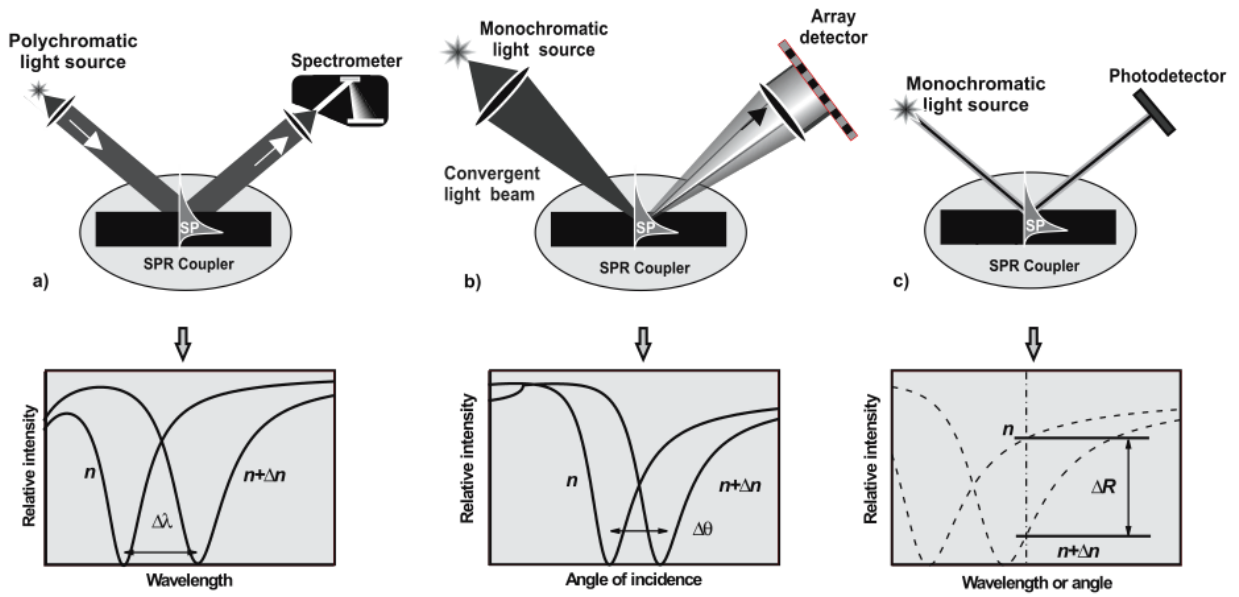


Figure 3-1. Scheme of various interrogations to monitor shifts in coupling wavelength, coupling angle, and light intensity generated by biomolecular binding events [100].

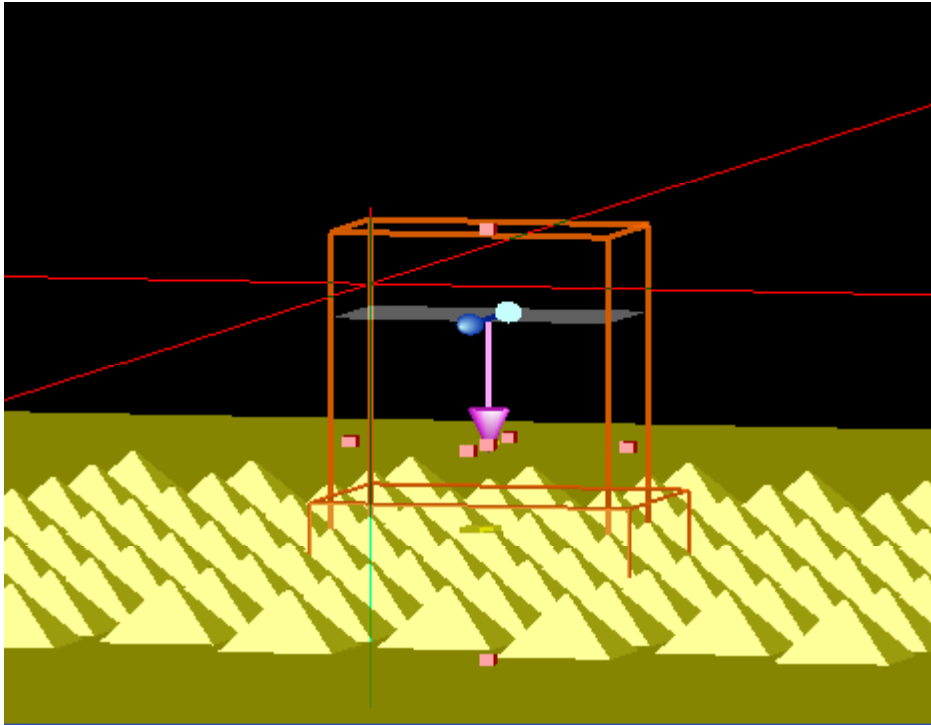


Figure 3-2. Scheme of excitation of SPPs by using a polarized light source along the surface normal. The size and properties of gold nanopillar arrays were set to mimic the real conditions.

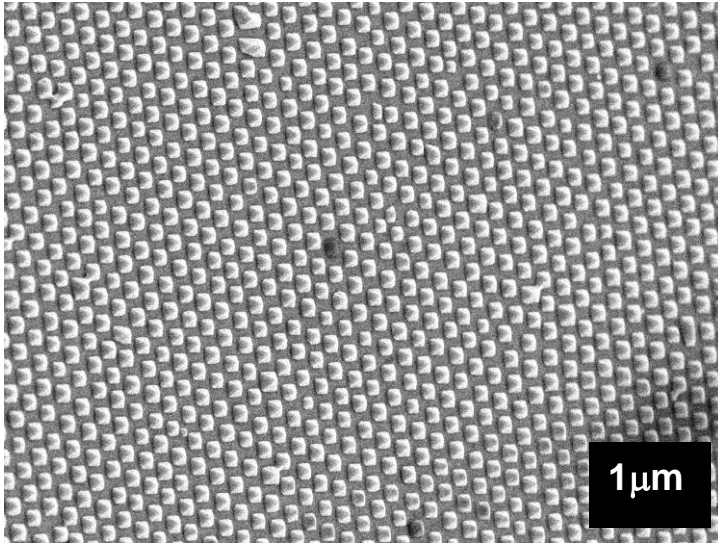


Figure 3-3. Tilted-view at 35° of SEM image of a templated gold nanopillar arrays. 320 nm of silica spheres were used to generate the template.

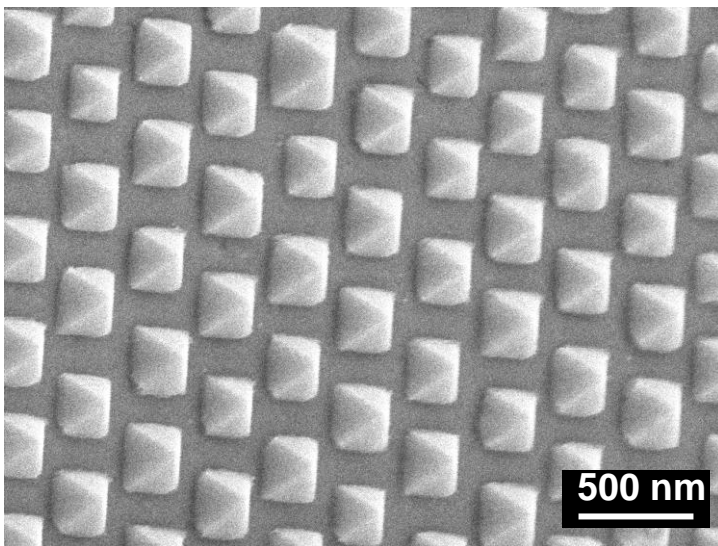


Figure 3-4. Magnified view of SEM image of the gold nanopillar arrays.

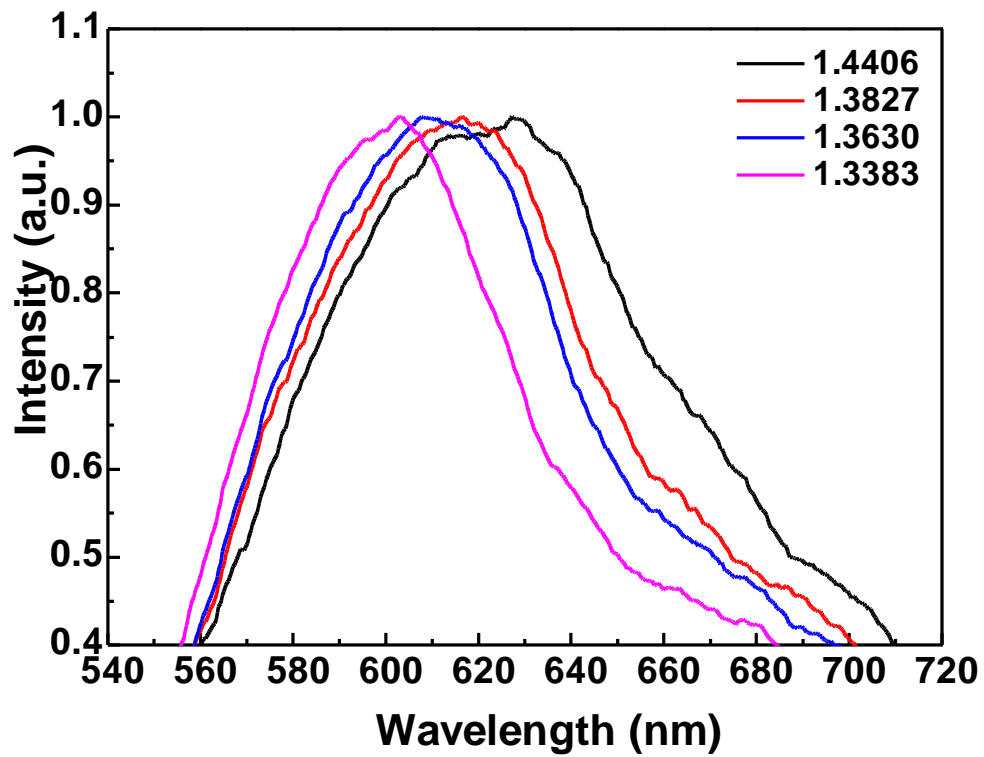


Figure 3-5. Optical reflection of white light excited at 45° on the gold nanopyramid array immersed in glycerol solutions of different refractive indices.

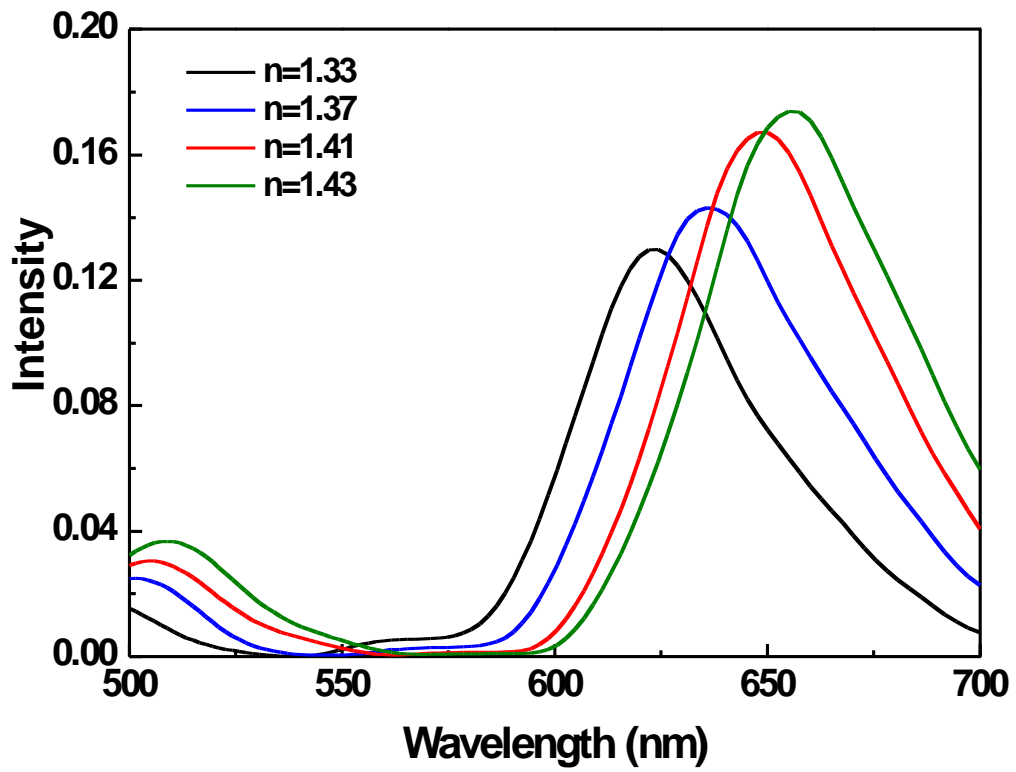


Figure 3-6. FDTD-simulated optical reflection of plane wave from a gold nanopyramid array immersed in liquids of different refractive indices.

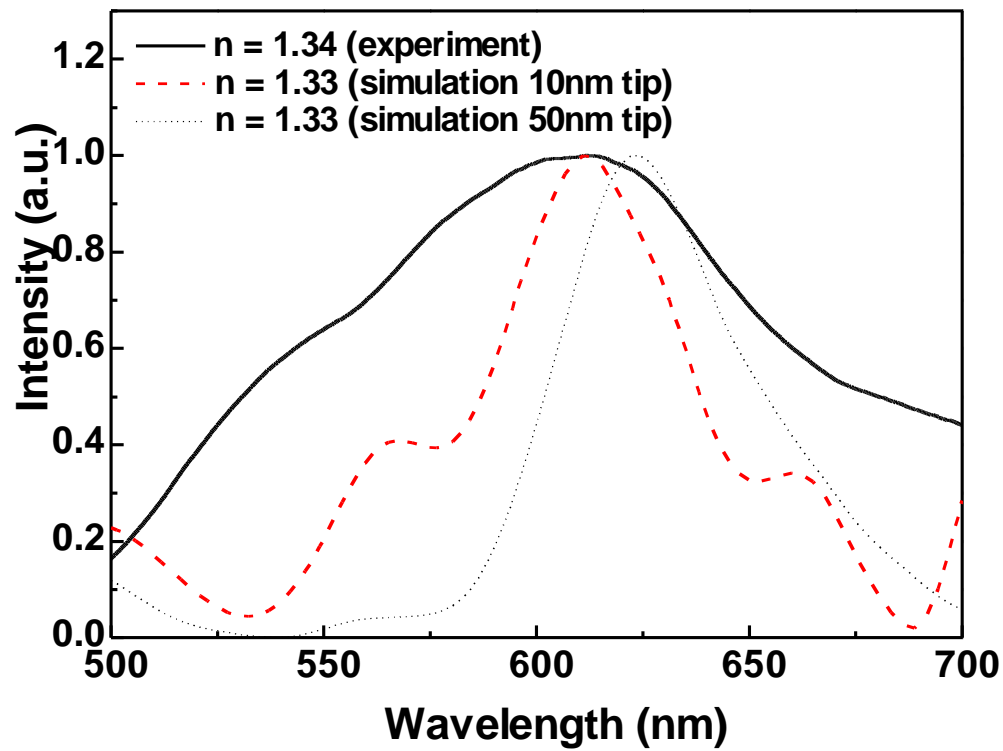


Figure 3-7. Comparison between normalized experimental (black solid line) and FDTD-simulated optical reflection from nanopillars with 10 nm (red dotted line) and 50 nm (blue dashed line) tips.

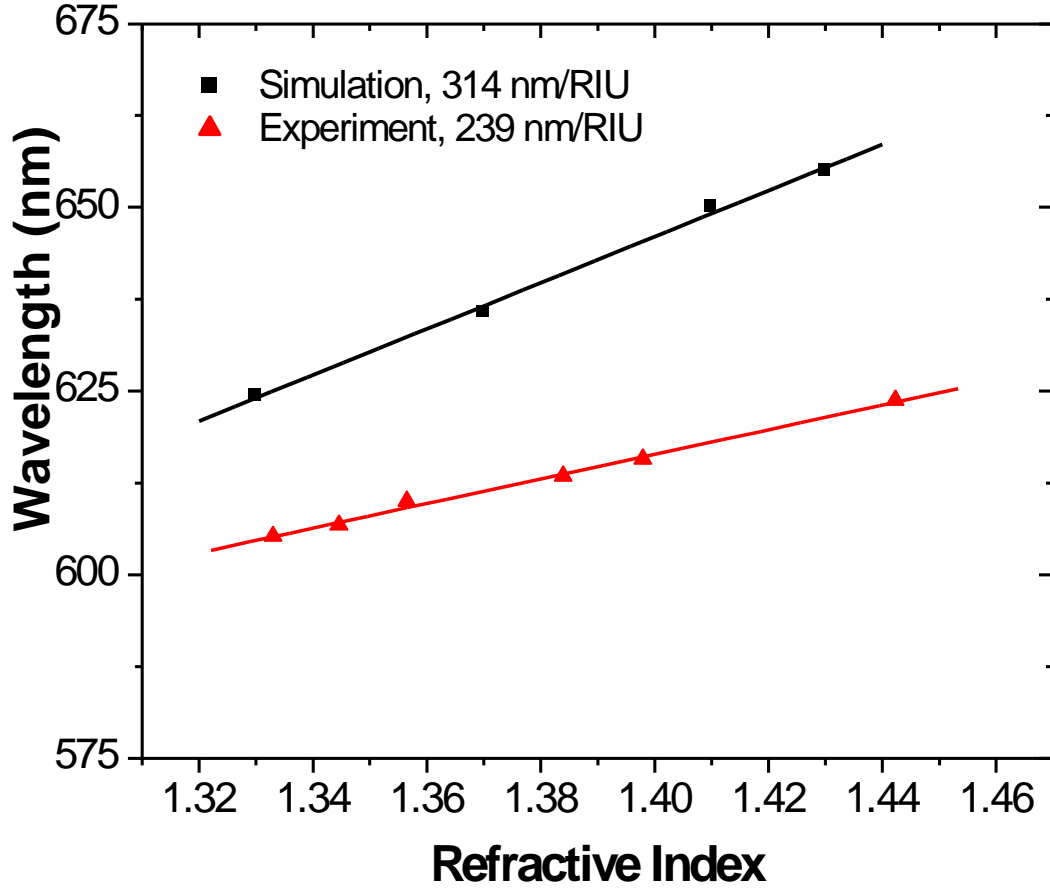


Figure 3-8. Comparison of detection sensitivity between the experimental result and FDTD simulation.

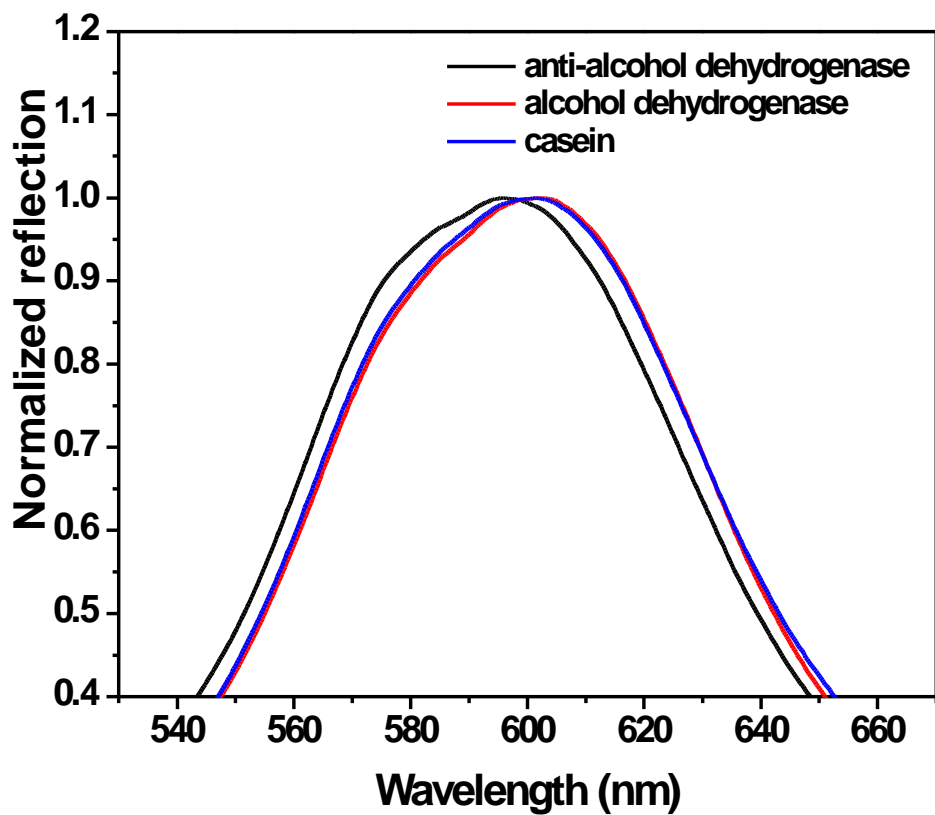


Figure 3-9. Normalized reflection spectra obtained from a gold nanopyramid array with adsorbed anti-alcohol dehydrogenase shown as the first spectrum from the left, followed by the addition of specific alcohol dehydrogenase, and nonspecific protein casein. The spectrum shows a red shift after the alcohol dehydrogenase addition, and a slightly blue shift is observed after the nonspecific protein binding

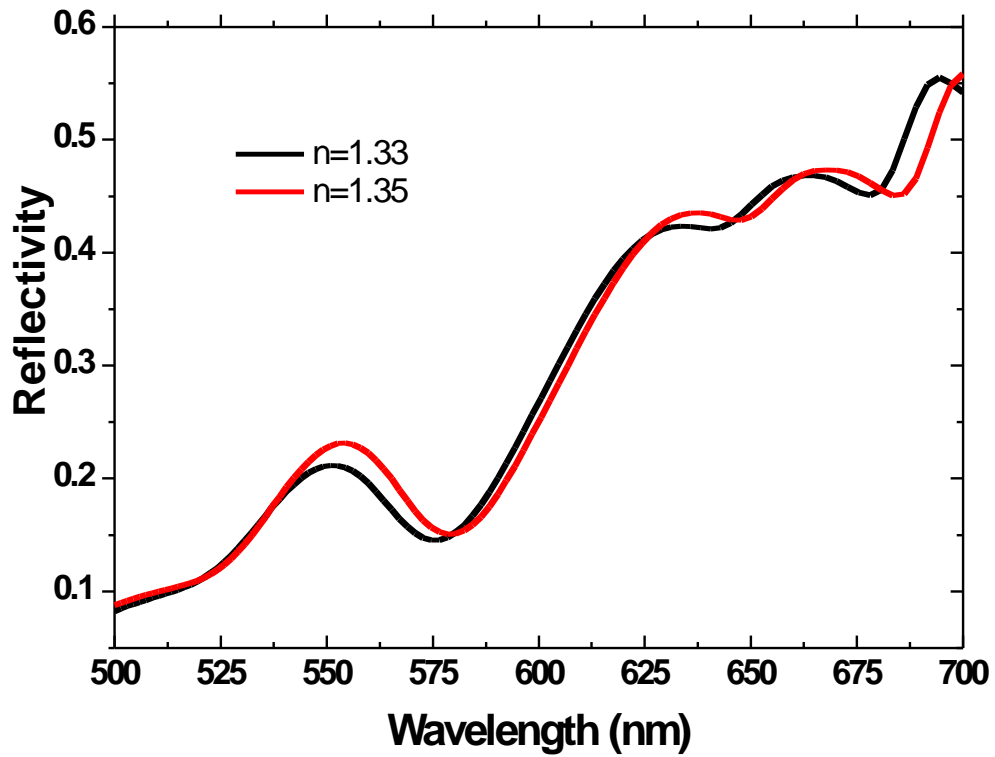


Figure 3-10. The simulated reflectivity. The normal incident light source was shone on the gold nanopillar arrays, and the environmental refractive indices were set as 1.33 and 1.35 respectively.

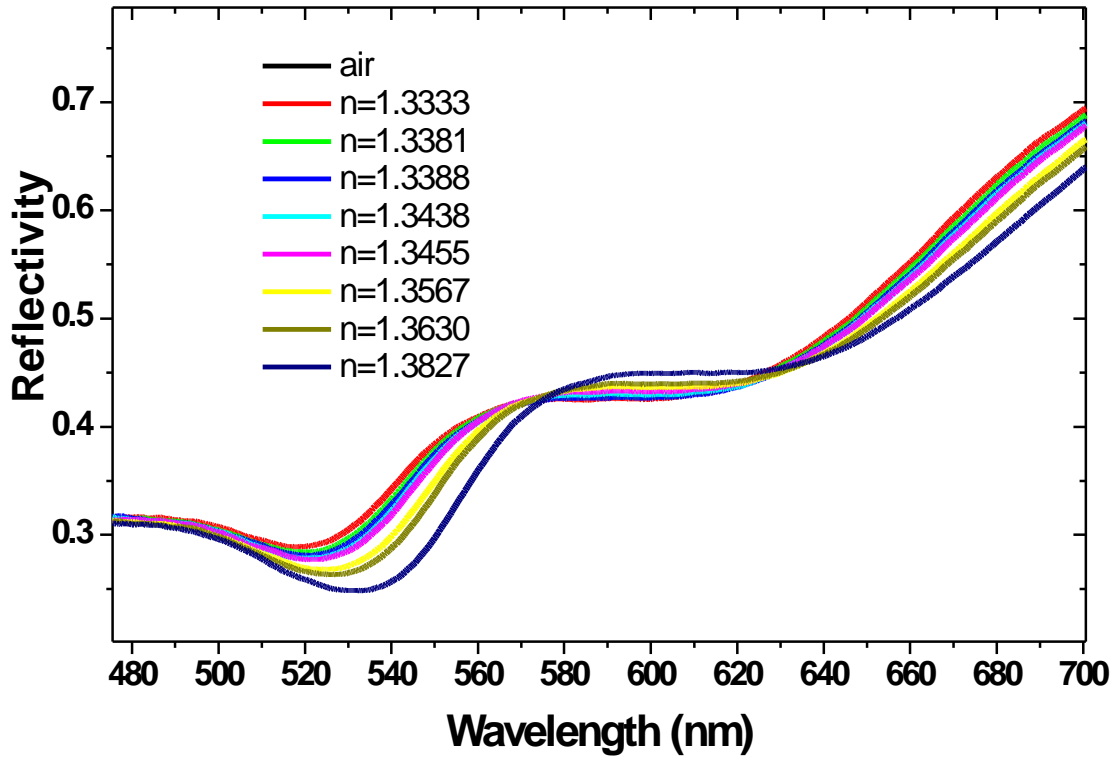


Figure 3-11. The experimental reflectivity changes in different environmental refractive indices.

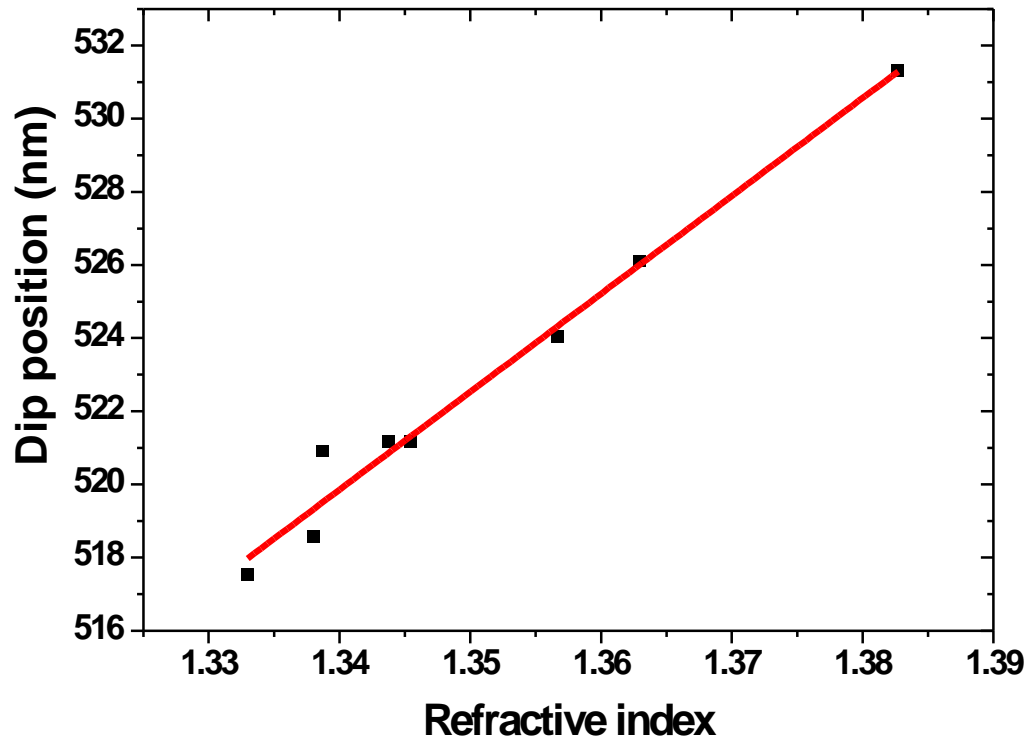


Figure 3-12. The sensitivity to the environmental refractive index. The linear fit of reflection spectra dip position to the environmental refractive indices is 268 nm/RIU.

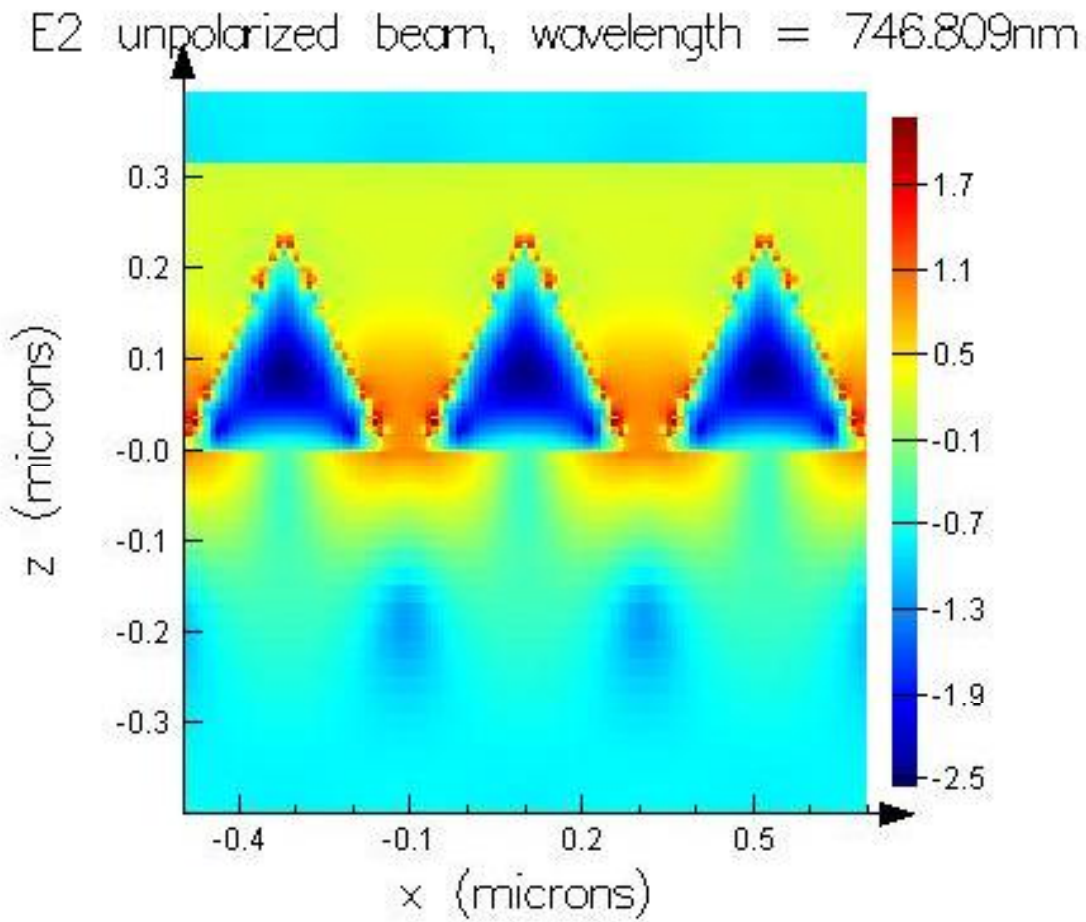


Figure 3-13. The FDTD-simulated electromagnetic field distribution in x-z cross section.

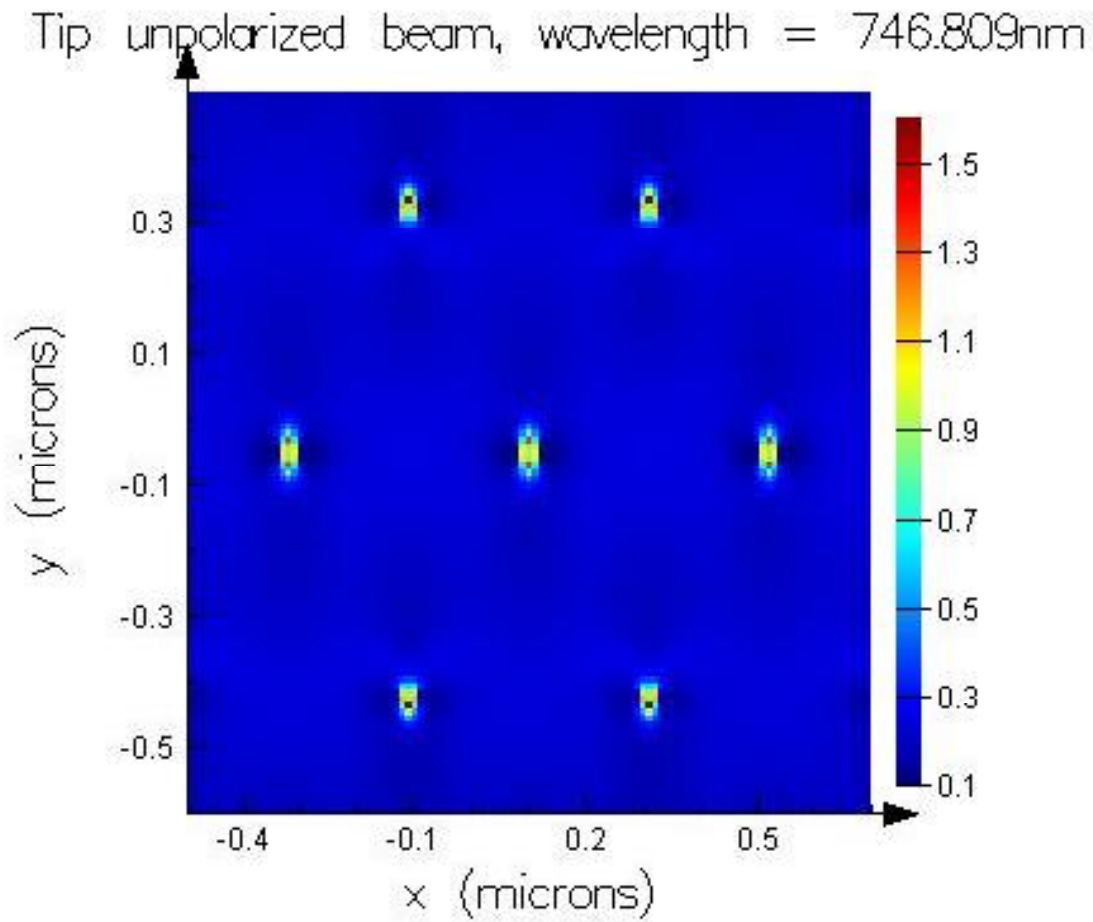


Figure 3-14. The FDTD-simulated electromagnetic field distribution in x-y cross section. The vertical position of the monitor is at the tip of nanopramids.

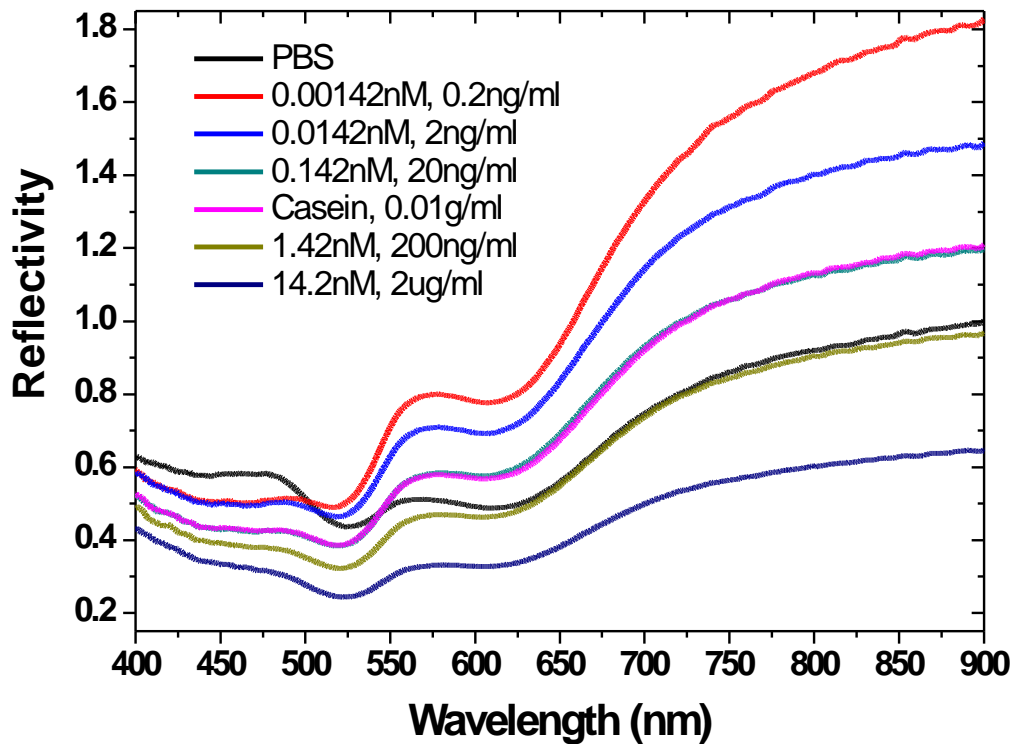


Figure 3-15. The biomolecule detection on an anti-alcohol dehydrogenase (AD) antibody modified nanopyramid array by using a 0° mode. At the beginning, 0.2 ng/ml of AD was added, and the spectrum was distorted due to the environmental RI changes. Later on, the concentration of AD was increased from 2 ng/ml to 2 μ g/ml and the obtained spectra were shifted in the same direction. The casein protein was added after incubating 20 ng/ml of AD, and the spectrum of casein was overlapped with 20 ng/ml AD. This represents adding casein did not generated any signal.

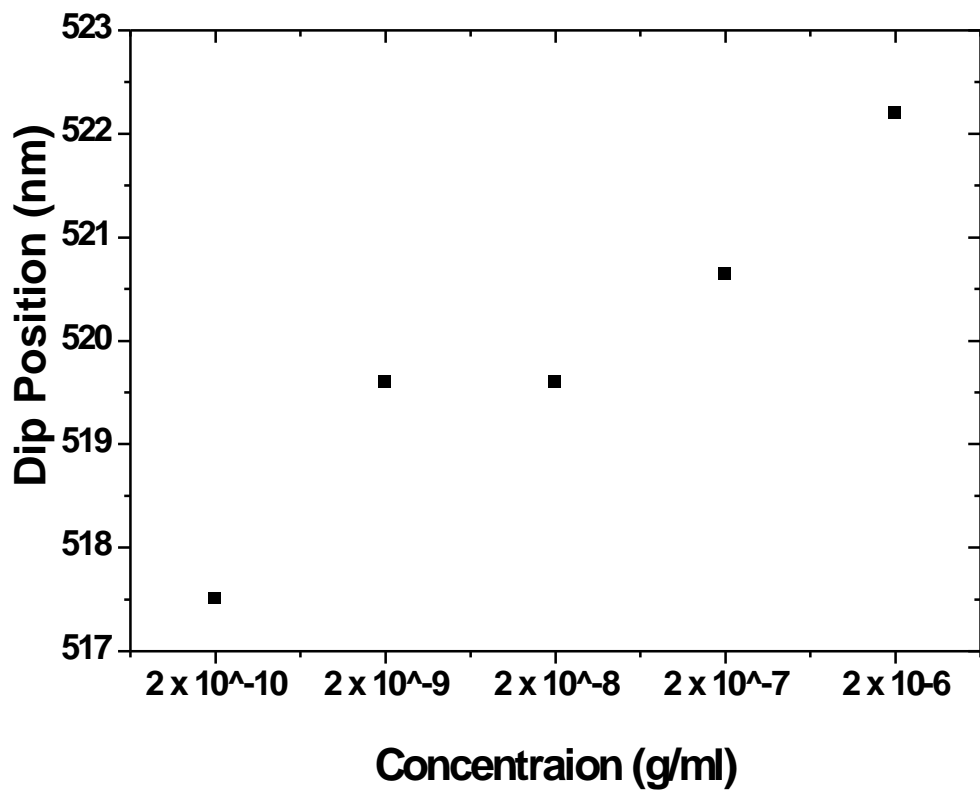


Figure 3-16. The plot of AD concentration versus the shifts in the spectra based on a single run.

CHAPTER 4 GOLD-POLYMER HYBRID PYRAMID BIOSENSORS

4.1 Background

In chapter 3, we reported the fabrication and application of the gold nanopyramid array with a highly engineered periodic structure. Most notably, they were fabricated by a scalable and cost-effective method developed by Dr. Peng Jinag's research group. The FDTD simulation shows the effect of SPPs on the gold nanopyramid arrays, and the experimental results validate the possibility of applying gold nanopyramid arrays as a SPR sensor. In Chapter 4, another composition of nanopyramid array, the gold-polymer hybrid nanopyramid array, is studied. The use of a gold-polymer hybrid composition benefits overall cost because only a 30 nm-thick layer of gold is deposited compared with a 500 nm-thick layer of gold used on the previous type of nanopyramid arrays. Furthermore, due to the weak mechanical strength of gold and the adhesion of gold on the sidewalls of inverted pits, a large number of the resulting gold nanopyramids are damaged after being peeled off from the silicon template. On the other hand, the gold-polymer hybrid nanopyramid preserves the shape very well. Although there is only a thin layer of gold, a localized electromagnetic field simulated by FDTD modeling predicts that this thickness is sufficient to generate SPPs.

Nanoscale metallic gratings, such as the nanopyramid structure, exhibit an extraordinary transmittance generated from the interaction between light and the SPPs [14, 61]. Because the metal film of gold-polymer hybrid nanopyramids is much thinner than the decay length of SPPs in metal (100-200 nm), SPPs can bounce back and forward within the metal film before decay. Therefore, SPPs generated at two interfaces can overlap with each other and therefore enhance the transmittance intensity. The

effect of extraordinary transmittance can be utilized for several applications including a SPR biosensor. When the biomolecular binding event is happening near the sensor's surface, an increased or decreased amount of bound proteins will vary the surface refractive index. This change results in transmission spectrum shifts. Compared with traditional bioassays using labeling such as with a fluorescent molecule or a protein tag, this SPR sensor enables an ideal label-free approach [13, 101]. Moreover, the extraordinary transmittance can be excited in the periodic metallic nanoscale grating by a vertical light without the use of prisms [79, 102], and therefore provides the advantage of a simple optical alignment for developing a portable, point-of-care and cost-effective system.

To fabricate a periodic metallic nanoscale grating by a cost-effective and scalable method, the colloidal templating technique was used to generate the wafer-scale hybrid nanopyramid arrays. In brief, inverted silicon pyramidal pits were etched from a non-close packed silica particle colloidal after particles were assembled on a wafer by a spin-coating technology. This mold was then used as a structural template to replicate arrays of polymer nanopyramids with nanoscale sharp tips. The last step involves the deposition of a thin layer of gold on the polymer nanopyramids and leads to the formation of gold nanopyramid arrays. As the result, the sharp nanotips can enhance the local electromagnetic field in its vicinity, and cavity effect can also localize the field by trapping SPPs within the cavities [79, 103] Due to the continued oscillation of light and free charge, SPPs should propagate on the surface of this periodic nanopyramid grating structure [56, 78, 104].

While the gold nanopyramid array can generate only reflected light, the gold-polymer hybrid nanopyramid array enables transmitted light that penetrates through thin gold film deposited on the top of polymer nanopyramids. Therefore, a transmission mode is used in this type of SPR sensor. The extraordinary transmittance effect in these arrays provides an opportunity for a simple microscopy-based apparatus [13]. For a higher sensitivity and resolution, the multispectral analysis [37, 105] used in Chapter 3 was also employed here. Reproducibility and repeatability of obtained sensing data were tested to evaluate the refractive index sensitivity. To demonstrate the effectiveness of the biosensing in a real-time, label-free approach, both of the anti-bovine serum albumin (anti-BSA) and thrombin binding aptamer were conjugated on the surface for targeting bovine serum albumin (BSA) and thrombin respectively. This chapter also presents the result of analyzing the thrombin binding aptamer conjugated on the nanopyramid array by SERS technique. The strong plasmonic effect on the array also enables enhanced Raman signals.

4.2 Experimental

4.2.1 Fabrication of Gold-polymer Hybrid Nanopyramids

Periodic gold-polymer hybrid nanopyramids were fabricated by a simple templating technology using spin-coated monolayer colloidal crystals as structural templates. The method of fabricating the inverted nanopyramid pit templates is described in Chapter 3. Simply put, mono-dispersed silica particles in UV-curable ethoxylated ETPTA (Sartomer USA, LLC) were spin-coated on a silicon wafer to form a non-close packed monolayer. Silica particles were then released by etching out ETPTA matrix and served as shadow masks for the deposition of chromium nanohole arrays. After removing silica particles, the silicon wafer with chromium nanohole arrays was subjected to an anisotropic wet

etching to generate inverted pyramid pits on silicon wafers. The wafers were then rinsed with deionized water and then wet etched with a chromium etchant (type 1020, Transene) to remove the chromium template. For protecting the surface, wafers were modified with octadecyltriethoxysilane (OTE) (Alfa Aesar) by immersing the wafer into the hydrolysis solution of OTE at 0.02 M, DI water at 0.28 M, and HCl at 0.0066 M in tetrahydrofuran (THF) for 30 min. ETPTA monomer was then used to fill up the pyramid pits and cured in contact with an (3-acryloxypropyl)trichlorosilane (APTCS)-primed glass slide, followed by a peeling-off process to reveal polymer nanopyramid arrays. After that, a thin layer of gold is sputter-deposited onto the polymer film to generate the gold/polymer nanopyramid arrays. Atomic force microscopy (AFM) is conducted on a Digital Instruments Dimension 3100 unit to visualize the structures formed.

4.2.2 Apparatus for Using the Gold-polymer Hybrid Sensor

Figure 4-1 shows the experimental setup for a transmission measurement adapted from an inverted microscope (Ti-U, Nikon). The sensor device consists of a hybrid nanopyramid array and integrated fluidics, and is set on the microscope stage for characterizing contacting fluids. A collimated white light along the surface normal was used to illuminate the metal side of the hybrid pyramid arrays. The transmitted optical signals that contain spectroscopic information of SPPs on the array are focused by a 10X microscope objective lens and then detected by a spectrometer (HR-4000, Ocean Optics) through an optical bundle (QP400-2-SR, Ocean Optics). As solutions passed through a fluidic flow cell and contacted the nanopyramid substrate, a multispectral analysis was used to calculate the total response from shifts in the transmission intensity and wavelength position. The sensitivity is determined by dividing the total

response by the refractive index changes in a “RIU” unit. The refractive indexes of glycerol solutions were checked by a refractometer.

4.2.3 Surface-enhanced Raman Spectroscopy

The SERS measurements were carried out by using thrombin binding aptamer synthesized by Dr. Weihong Tan’s research group in Department of Chemistry at University of Florida. The synthesized thrombin aptamer is a 29-base single strand oligonucleotides with 5-base spacer as AGT CCG TGG TAG GGC AGG TTG GGG TGA CTT TTT T-SH. To minimize contamination and enhance the aptamer binding on the surface of the gold-polymer hybrid nanopyramid arrays, the arrays were cleansed by an air-plasma cleaner (PDC-32G, Harrick Scientific) at medium power for 3 min. 40 μ l of thrombin aptamer at 76.8 μ M was incubated on the cleansed hybrid nanopyramid arrays. After an overnight incubation, the arrays were gently washed with PBS solution, and then put on Renishaw inVia Raman microscope equipped with a 785 nm high power near infrared diode laser. At the beginning, a calibration step was run with a Si sample. Raman spectra of the thrombin binding aptamer on arrays were excited by a 785 nm laser at 0.5 mW through a 50X objective lens. The signal integration time is 30 s, and spectra were accumulated 5 times for improving the signal to noise ratio. The control spectrum was collected from the nanopyramid array without the aptamer conjugation.

4.2.4 Finite-difference Time-domain Simulation

We used Lumerical FDTD Solution software (from Lumerical Solution, Inc, Canada) to simulate the distribution of the electromagnetic field around the nanopyramid arrays. FDTD is a numerical solution of Maxwell’s equations useful for

complex geometries. The geometrical parameters of simulated structures were chosen to mimic the experimental situation which included a 30 nm-thick gold layer on the top of ETPTA nanopyramids with a base length, a height, and a tip length set as 300 nm, 200 nm and 50 nm, respectively. The angle between x-axis and y-axis is changed to 60 degrees for the hexagonal ordering of nanopyramids. The lattice length between two adjacent nanopyramids is 420 nm, which can be obtained from the SEM image. The structures were attached to a glass substrate.

Symmetry and asymmetry boundaries were used on x- and y-axis of the simulation region respectively. A perfect matched layers (PML) boundary was used at the top and the bottom for providing an absorption boundary condition so that little or no electromagnetic radiation is reflected back into the simulation region. A dz mesh refinement of 5 nm was set in order to make sure the mesh is fine enough to resolve the nanopyramid structures. A light source consisting of planar electromagnetic waves was placed 70 nm above the nanopyramid tips, with intensity amplitude of 1.0. The size of the light is 1200×1200 micron to cover all structures, and the wavelengths were set from 300 nm to 1300 nm. Because an unpolarized beam was used in the experiment, we designed the same condition in the simulation. The resulting profiles excited from 0° and 90° polarized light sources were averaged to plot the electromagnetic field distributions by an unpolarized excitation.

4.3 Results and Discussions

4.3.1 Fabrication of Gold-polymer Hybrid Nanopyramid

Figure 4-2 shows AFM image of an array of gold-polymer hybrid nanopyramids fabricated by the colloidal templating method. The ETPTA nanopyramid arrays were

templated from the patterned silicon wafer by filling ETPTA monomer into the pyramid inverted pits on the silicon wafer, then curing ETPTA in contact with an APTCS-primed glass slide, and finally peeling off ETPTA from the wafer. To prevent the breaking of the sharp nanotips during peeling off the polymer nanopyramids from the silicon template, the sidewalls of the silicon pits are modified by OTE. Polymer nanopyramid arrays can then be easily replicated by using the patterned silicon wafer as a reusable mold.

To create an interface of metal and dielectric materials, a 30 nm thick of gold film was deposited on the top. Figure 4-2 shows that these hybrid nanopyramids have defined tips and edges, and curvature radius of most of the tips are less than 5 nm. Because the size of nanopyramids is nano-scale, the arrays contain a high packing density of nanopyramids as SPR sensing elements, and therefore increase contacting area as well as localized electromagnetic field so called “hot spot” area. Notably, a single one-inch-sized array carries $50,000 \times 50,000$ nanopyramids. The size of array is even scalable up to the size of a silicon wafer.

Striking iridescent colors showed in Figure 4-3 is due to the periodic orientation of hybrid nanopyramids that generates the diffraction. The diffracted wave can couple with SPPs by providing a wave vector.

4.3.2 Extraordinary Transmission of Gold-polymer Hybrid Nanopyramid

The effect of extraordinary transmission generates a higher intensity of light through subwavelength aperture than the predicted value from Bethe’s theory, which derives the transmission efficiency for a system containing a single hole milled in a metal film as:

$$\eta_B = 64(kr)^4 / 27\pi^2 \quad (4-1)$$

where η_B is the transmission efficiency, $k = 2\pi/\lambda$ is the wavevector of the incoming light, and r is the radius of the hole. This phenomenon is attributed to the role of SPPs as the concentrated electromagnetic waves resonantly interact with free charges on the metal. In addition, if a single hole is surrounded by a periodic structure, the intensity of transmitted light is even higher because the periodic structure acts as an antenna and generates a strong coupling. However, only a limited amount of structures can be created on the nanohole arrays due to the issues in cost and time of focused ion beam or e-beam lithography.

On the other hand, colloidal templated technology generates a high density of a periodic structure in the nanopillar array, and therefore results in a strikingly strong coupling. A thin layer of metal coated on the ETPTA also contributes to stronger oscillation compared with other metallic nanostructured substrates. As the decay length of SPPs is usually only 100-200 nm in a metal, most of the SPP energy is absorbed in metallic nanostructured substrates. However, since the thickness of the metal film is only 30 nm on hybrid nanopillars, SPPs generated at the water/metal interface can penetrate the metal and arrive at the glass/metal interface. It is likely that SPPs generated at two interfaces can bounce back and forward with a minimal energy decay. Therefore, this resonant oscillation further enhances the effect of extraordinary transmission.

To evaluate the effect of extraordinary transmission, the measured intensity of transmitted light through hybrid nanopillar arrays was divided by the intensity for the same thickness of a flat gold substrate. As a result, this ratio exceeded 3.5 at around 800 nm in the spectra. This enhancement was even stronger when both of hybrid

nanopyramid arrays and flat gold substrate were immersed in a higher RI solution as shown in Figure 4-4. In Figure 4-4, the baseline transmission spectrum obtained in the air was subtracted from all the spectra to reduce the background noise. The stronger transmission in an increased RI environment is related to the longer optical path which causes a tight SPP confinement within the cavity [105]. Therefore, a stronger transmission induced by increased RI gives rise to the possibility of utilizing the hybrid nanopyramid arrays for a sensor that detects the varied RI near the metal/water interface.

4.3.3 Finite-difference Time-domain Simulation

To understand the mechanisms of the hybrid nanopyramid arrays, the three-dimensional FDTD simulation was used to model the electromagnetic field distribution at an assigned surface. The simulated electromagnetic field enhancement, $|E_i|^2$, was normalized to the intensity of light incidence. Figure 4-5 illustrates the field distribution on the x-y plane at the bottom of hybrid nanopyramids. A strong electromagnetic field was observed surrounding the edges of pyramids, and these areas are called “hot spot” areas due to the high enhancement. Since these concentrated SPPs generated on arrays are especially sensitive to the alteration in RI, the hybrid nanopyramid array can be applied for a high sensitivity SPR biosensor. The varied RI caused by biomolecular binding events at hot spot areas intensively modulates the properties of SPPs and results in shifts in transmission spectra. Furthermore, a limited surface of hot spot area is likely to achieve a low detection limit.

Interestingly, the tip of hybrid nanopyramid exhibits a much higher electromagnetic field enhancement, $|E_i|^2$, by a value of 500 in the x-z cross sectional profile as shown in

Figure 4-6. The similar enhancement surrounding protrusions is also observed in other types of plasmonic nanostructured substrates. To verify whether the enhancement happens at a specific nanopyramid or the majority of nanopyramids, the simulation monitor was set in the x-y cross-section at the height of the tips as illustrated in Figure 4-7. The simulated result shows that all of the nanopyramids exhibit the same enhancement and suggests that the concentrated electromagnetic field is generated at most of the nanopyramids.

It can be concluded that the biomolecular interactions happening at hot spot areas such as edges and tips of nanopyramids will amplify the signal in a sensogram. Moreover, the more amounts of nanopyramids increase the area of hot spots and benefit the sensing application. The cost-effective and high-throughput nanofabrication used here is able to create numerous nanopyramids. A large area of hot spots on the hybrid nanopyramid arrays therefore increases the sensitivity and lowers detection limit for biosensing application.

4.3.4 Refractive Index Sensing of Gold-polymer Hybrid nanopyramid

To increase the RI sensitivity, a multispectral analysis mentioned in Chapter 2 is utilized here and integrates shifts of multiple resonances in spectra. The integrated response [105] is calculated by the equation:

$$R = \int |\Delta T_{norm}| d\lambda = \int \left| \frac{T_{solution} - T_{baseline}}{T_{baseline}} \right| d\lambda \quad (2-2)$$

where $T_{solutions}$ is the measured transmission of the arrays in a given solution, and $T_{baseline}$ is the baseline transmission in water or air. Because the transmission subtraction is normalized to the baseline transmission, the unit of the integrated

response is still “nm”, the same as the unit of conventional method. The value calculated by this equation can be pictured as the shifted area of spectra in Figure 4-4.

The RI sensitivity is obtained by injecting mixtures of glycerol and DI water at different concentrations into the flow cell consisting of the gold nanopyramid arrays. At the beginning, the transmission in the air was recorded as the baseline. Increased concentrations of glycerol solutions were then injected sequentially to vary the refractive index from 1.3425 to 1.3743. The transmission spectrum was recorded at the end of each injection and calculated the total response according to Equation 4-2. Since an increasing RI enhances the intensity of transmission, the calculated value for the total response also becomes greater as shown in Figure 4-8 and 4-9. These figures plot the total response versus the RI variation, and the gradient of trend line yields the bulk refractive index sensitivity in a unit of nm/RIU. By using the multispectral analysis, the performance of hybrid nanopyramid arrays achieves a remarkable sensitivity of 2000 nm/RIU, which is comparable to the sensitivity of a prism-based SPR sensor for a value of 12000 nm/RIU.

As mentioned before, nanoparticle conjugated-substrate is usually suffered from the instability of particle configuration, inter-particle distance, and inconsistent data. On the other hand, the templating technology used here for fabricating nanopyramid arrays preserves the configuration well, and therefore increases the data stability and reproducibility. To evaluate the stability of the detected signals, date to date variation on substrates and area to area variation in the whole sensing system are demonstrated in Figure 4-8 and 4-9 respectively. In Figure 4-8, data was collected on three different dates by using the same. The result shows the reproducibility, and the standard error is

130 nm/RIU. On the other hand, the repeatability shown in Figure 4-9 was determined by data obtained from three different sensing areas on the arrays in the same day. The calculated standard error is 37 nm/RIU, and it is lower than the standard error of reproducibility test. These results suggest a good data reproducibility and a durability of the hybrid nanopyramid array for a repeated use.

4.3.5 Surface-enhanced Raman Scattering Peak Identification of DNA aptamer

Although SERS technique is a powerful method for detecting biomolecules, studying their structures, and monitoring conformation changes based on their characteristic SERS peaks, the use of SERS-active labels limits the data reproducibility. On the other hand, a SERS-active substrate which exhibits the enhancement inherently enables a label-free alternative. In this study, thrombin binding aptamer and thrombin were conjugated on the SERS-active hybrid nanopyramid substrate for obtaining SERS signals.

Figure 4-10 reveals the SERS spectra of thrombin aptamer on the hybrid nanopyramid array and on the flat silicon wafer. Thrombin aptamer is a 27-base DNA for binding with the thrombin protein. Aptamers are considered to be substitutes for biomolecules such as antibodies, peptides or other recognition probe. They are selected from a large random sequence library by the process of Systematic Evolution of Ligands by Exponential Enrichment (SELEX). The process is conducted by incubating a random nucleic acid library with target molecules followed by the enrichment of bound nucleic acid by PCR amplification. The enrichment continues for several times until a strong aptamer candidate with a low dissociation coefficient was selected. Compared with

antibodies, aptamers can be generated in a cost-effective synthesis, and they are relatively stable.

The target protein, thrombin, is a serine protease which exhibits both of the enzyme- and hormone-like properties and plays a major role in regulating cell signals and in the process of blood clotting. Therefore, it is a key substance involved in coagulation-related processes and also a useful tumor marker for the diagnosis of pulmonary metastasis. Although an efficient thrombin detection is of great concern, a majority of diagnostic method involves an indirect detection by measuring fibrinogen which could be converted from soluble fibrinogen into insoluble fibrin by thrombin protein. Therefore, a direct, real-time, and even cost-effective alternative will benefit the clinical application.

The thrombin aptamer was dried on the pyramid array for SERS characterization. To increase the concentration of thrombin aptamer contacting the silicon wafer, the wafer was immersed in a higher concentration of aptamer solution. Figure 4-10 shows that the hybrid nanopyramid array generated several characteristic SERS peaks, but the silicon wafer did not produce significant SERS peaks. Figure 4-11 further examines a detailed result by subtracting the control spectrum from obtained spectrum. The SERS peak at 998 cm^{-1} is related to phenylalanine or the deoxyribose vibration. The peak around 1098 cm^{-1} is associated to the backbone stretching or the characteristic peak of guanidine triphosphate and the G-quadruplex. Another peak observed near 1245 cm^{-1} is attributed to the deoxythymidine. In addition, peaks surrounding 1396 cm^{-1} is due to the two different mechanisms lying behind. One is the CH_2 deformation, and the other one is contributed from the ring stretching mode of the guanine. Figure 4-11 also compares

the spectra of pure aptamer and a complex of aptamer and thrombin protein. The result shows that the characteristic SERS peaks did not shift significantly after adding thrombin protein because the over dried aptamer might lose the reactivity to the thrombin protein. Although the wave number shifts were not apparent, the Raman intensity was increased after adding thrombin protein.

4.4 Summary

In summary, we have successfully fabricated a new hybrid plasmonic crystal, the gold-polymer nanopyramid array, using a cost-effective templating method. The technique preserves the uniformity of the sharp nanopyramid with reproducible features, and thus suggests a platform for high quality array fabrication. Moreover, the cost is greatly reduced due to an extremely thin layer of gold deposited on the polymer, and the miniature system becomes achievable because of the straightforward optical path. The nature of the coupled resonance at both gold-polymer and gold-solution interfaces exhibits an extraordinary transmission. Theoretical modeling illustrates the strong coupling at limited surface of hot spot areas which are beneficial to high RI sensitivity, and a multispectral analysis even further increases the sensitivity. To evaluate the applicability of label-free SERS biosensing on the hybrid nanopyramid arrays, thrombin aptamer and thrombin were tested. The reported result in SERS characterization suggests a wider application of nanopyramid arrays.

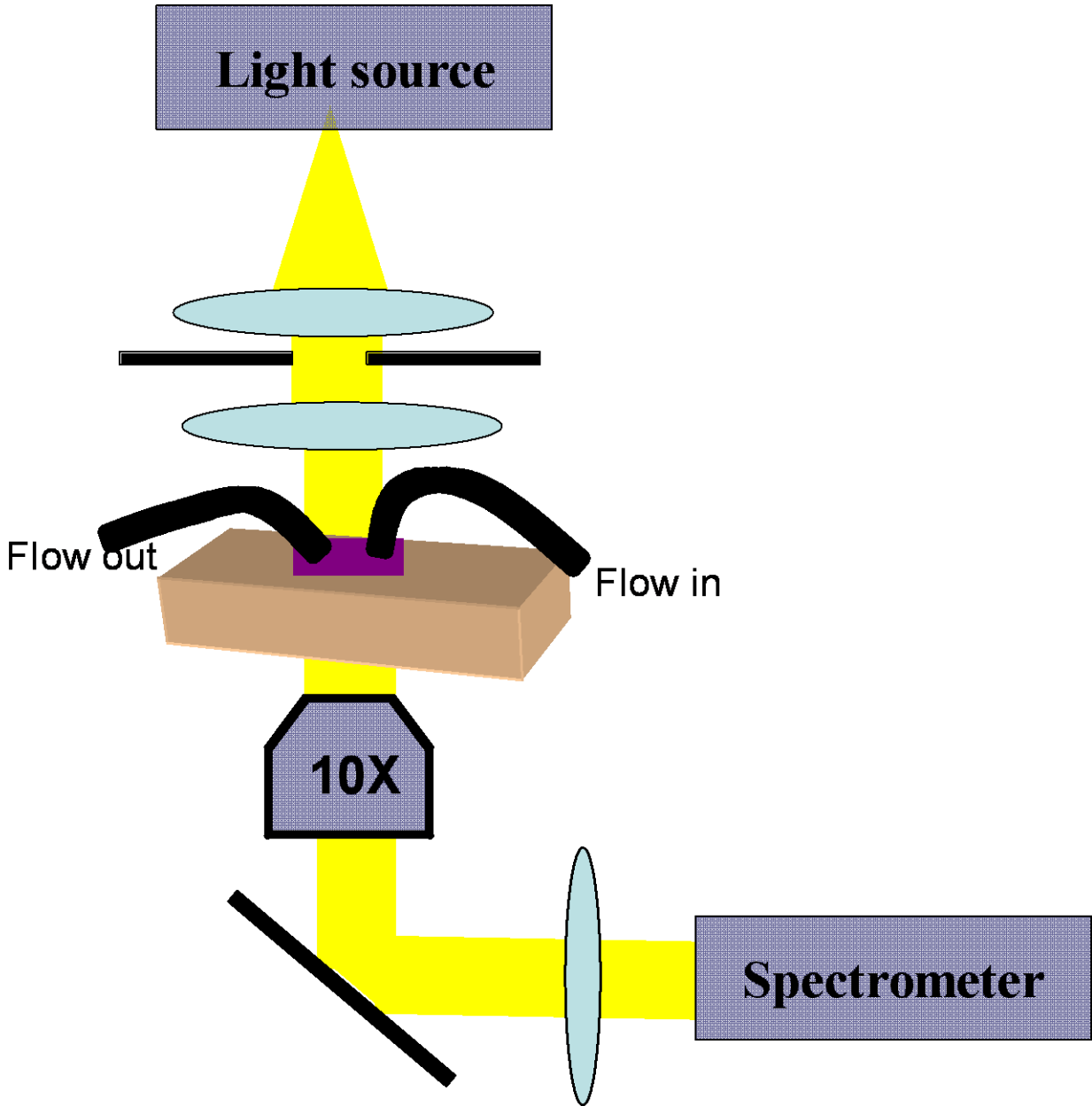


Figure 4-1. Schematic of the optical SPR measurement system adapted from a bright-field inverted microscope. The lamp radiates the broadband white light on the sensor device that contains a nanopillar array and flow cell. Transmitted light through the device is focused by a 10X microscope objective, and then transmitted to a spectrometer through optical bundles.

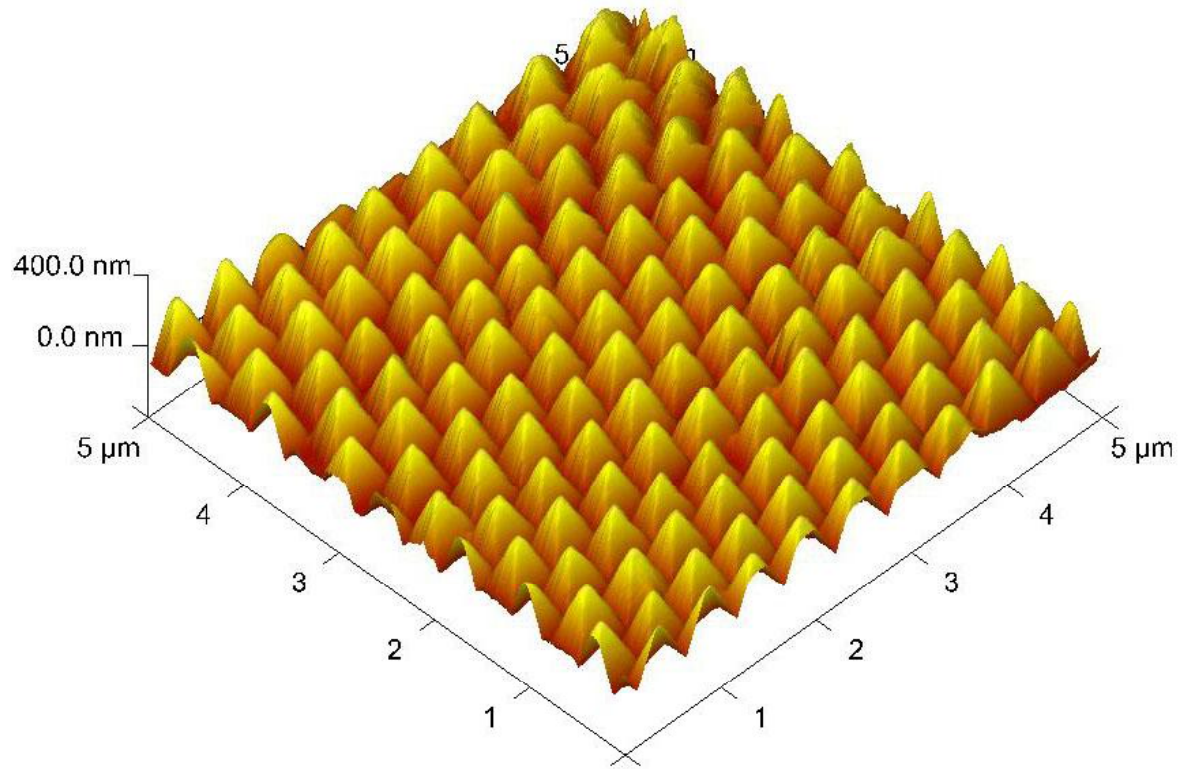


Figure 4-2. AFM images of nanopyramid arrays templated from the inverted silicon pyramidal pits.

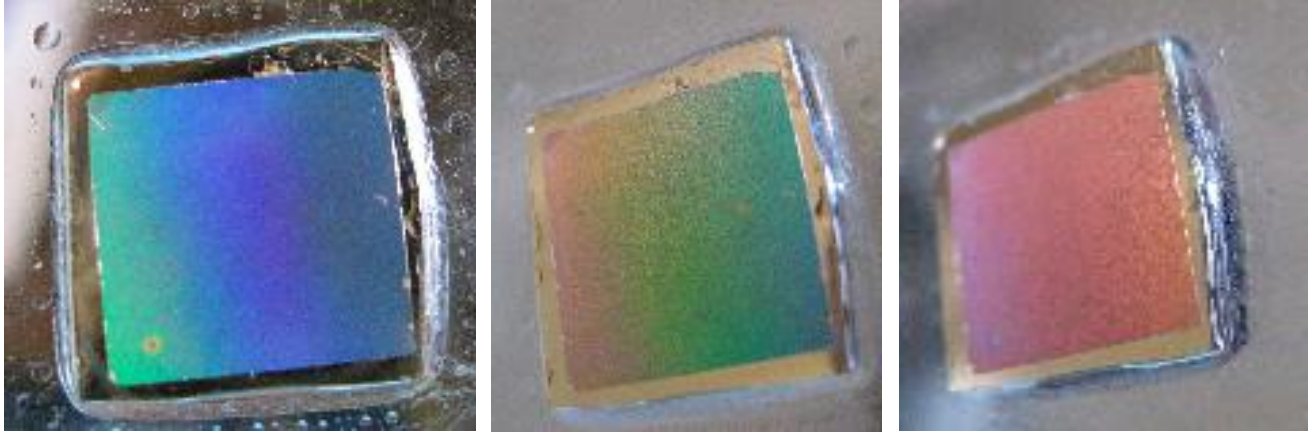


Figure 4-3. Photos of a one-inch-sized hybrid nanopillar arrays. Due to the hexagonal ordering of nanopillar arrays, diffracted light is generated at varied angle, and therefore illuminates iridescent colors.

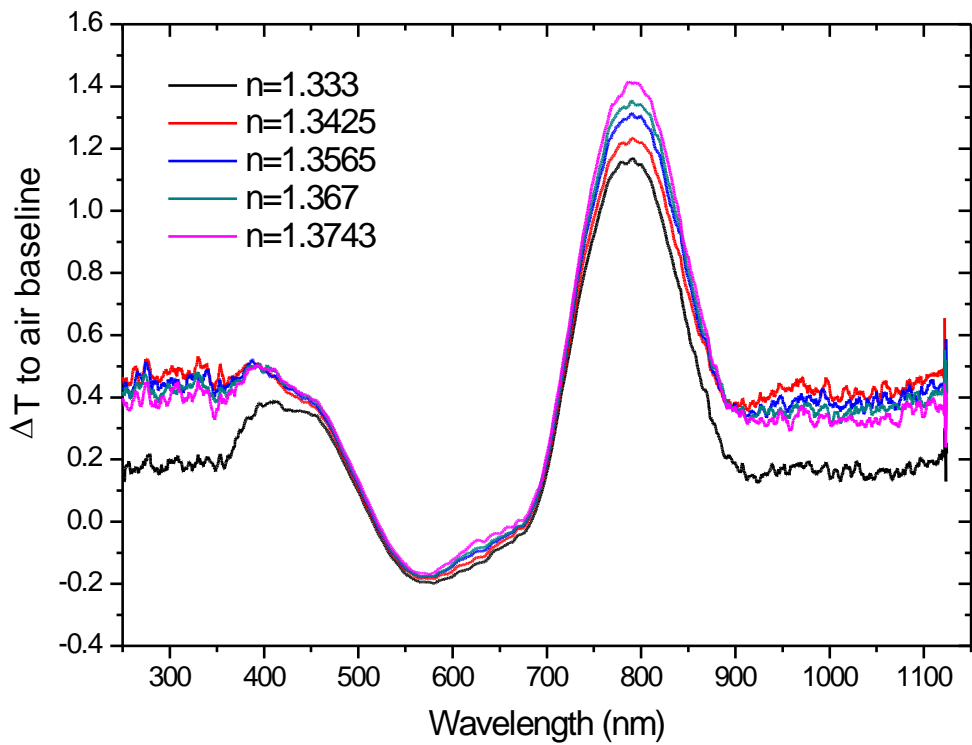


Figure 4-4. Transmission spectra through hybrid nanopyramid arrays immersed in various refractive index solutions. Baseline spectrum for air medium was subtracted from other transmission spectra.

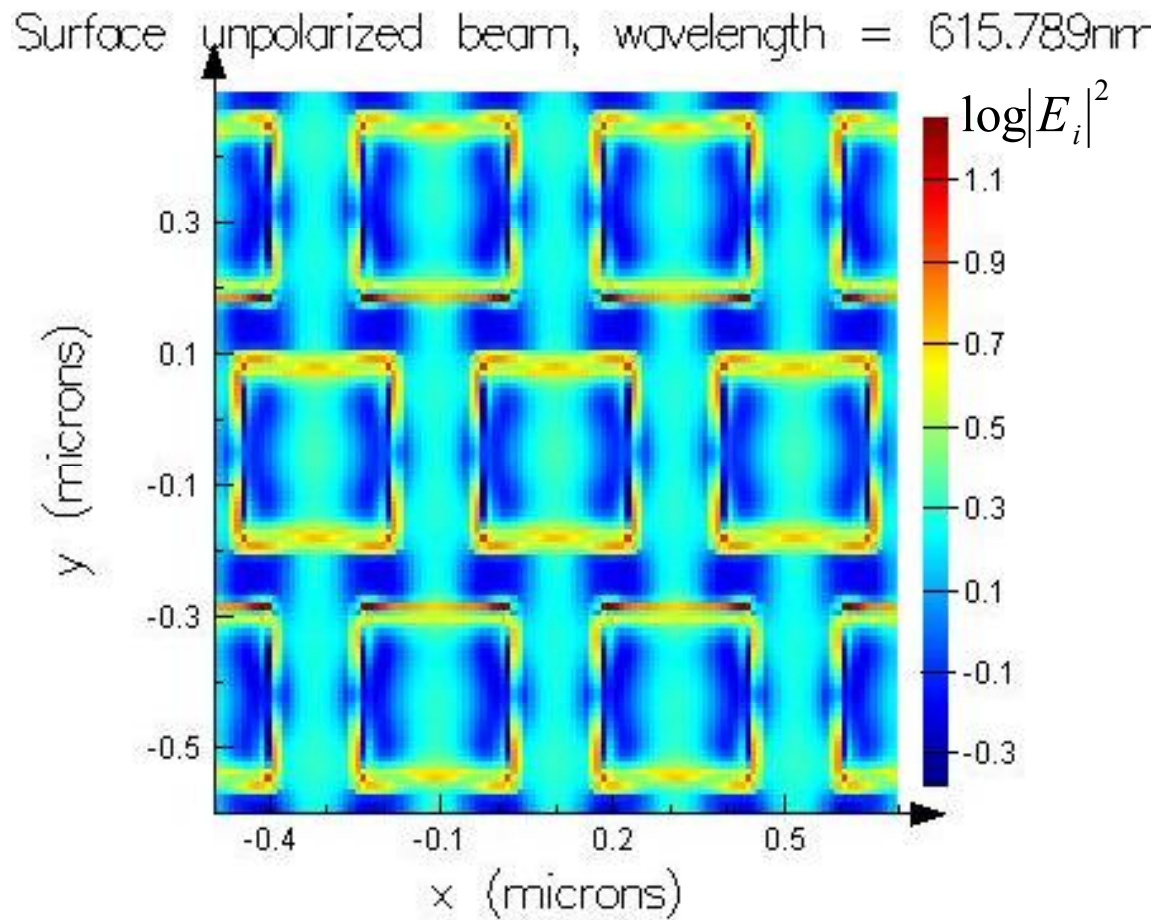


Figure 4-5. Simulated electromagnetic field enhancement by FDTD modeling. Cross-sectional x-y profile at the nanopyramid bottom shows the focused electromagnetic field at the edge surrounding nanopyramids.

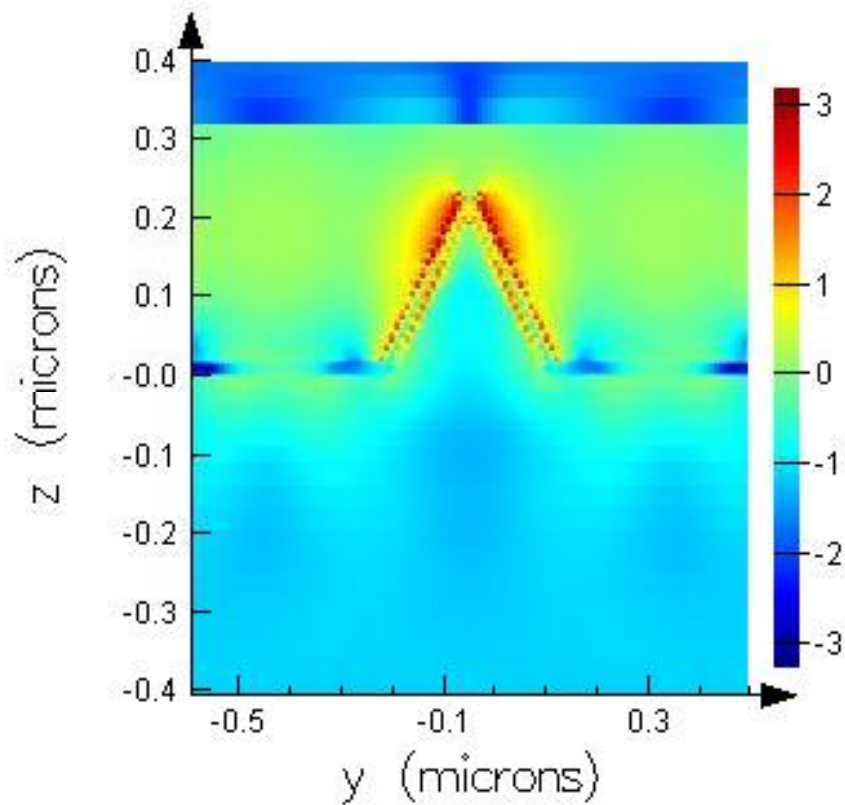


Figure 4-6. Simulated electromagnetic field enhancement by FDTD modeling. The logarithm of electromagnetic field was plotted versus the position at cross-sectional of x-z surface. The particularly strong field shown as red color is surrounding the tip of nanopillars.

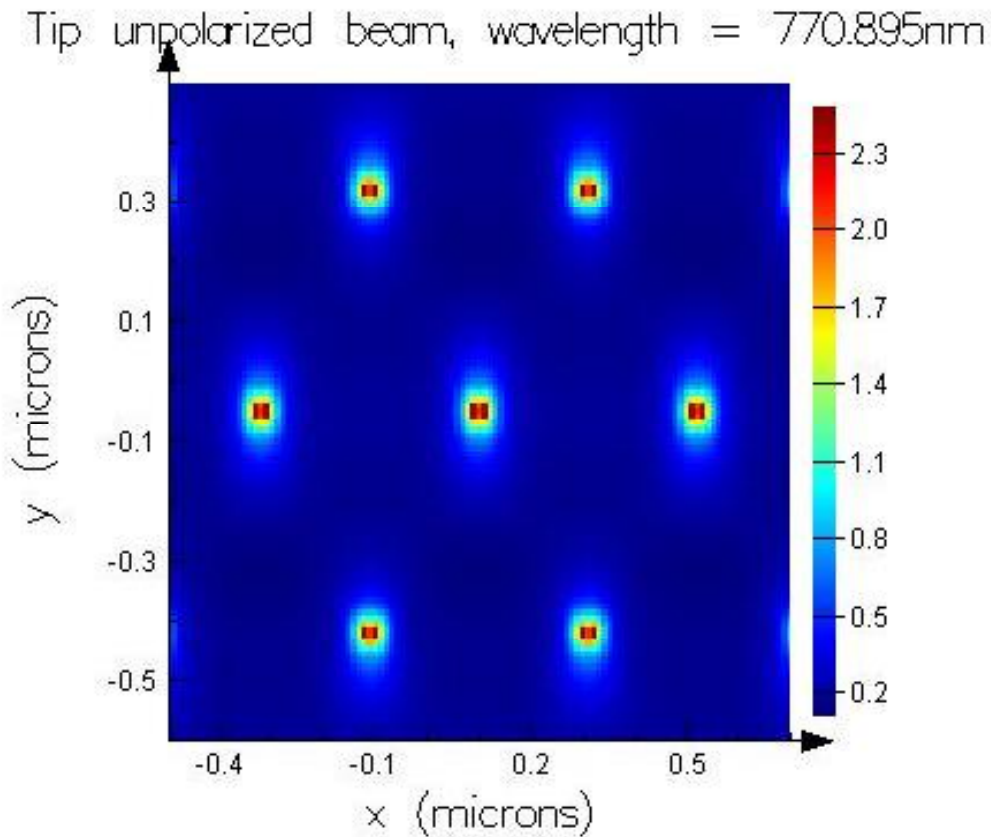


Figure 4-7. Simulated electromagnetic field enhancement by FDTD modeling. The logarithm of electromagnetic field was plotted versus the position at cross-sectional of x-y surface. The height is located at the tip of nanopyramids. The focused electromagnetic field shown as red color is also surrounding the tip of nanopyramids.

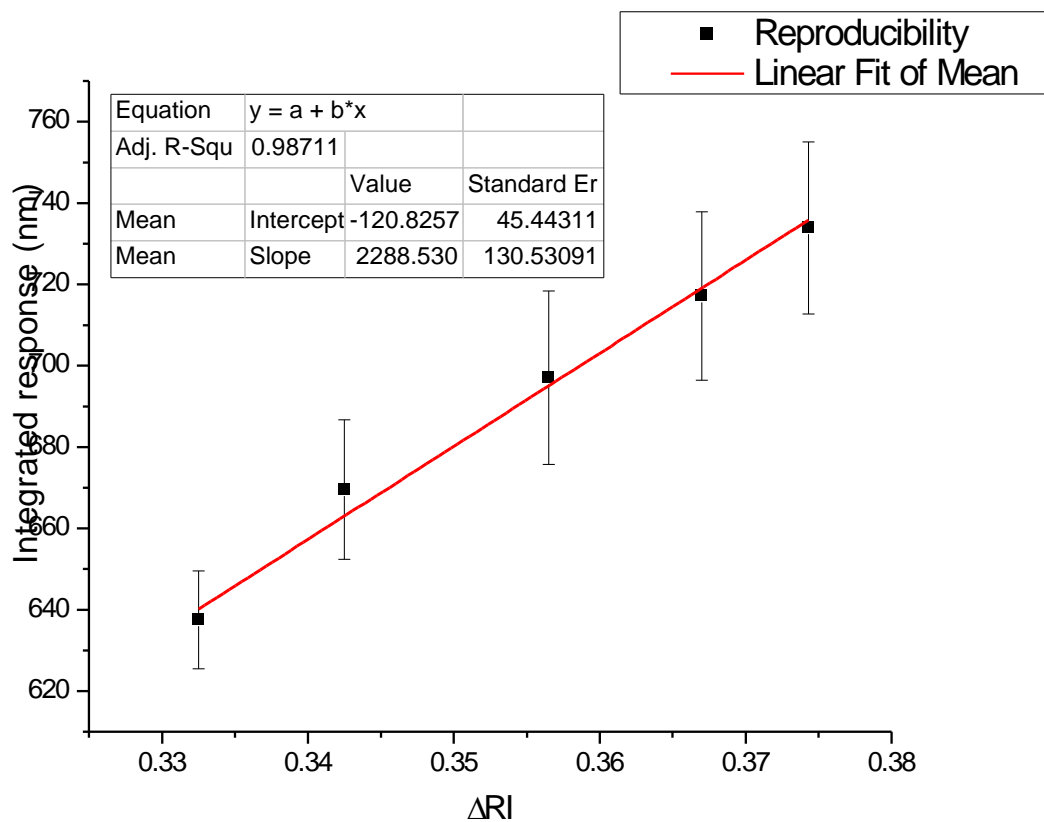


Figure 4-8. Evaluation of refractive index sensitivity and reproducibility for hybrid nanopyramid arrays. The integrated total response was obtained from the area shifts from baseline spectrum to each spectrum. Standard deviation was calculated from triplicate measurements on three different days.

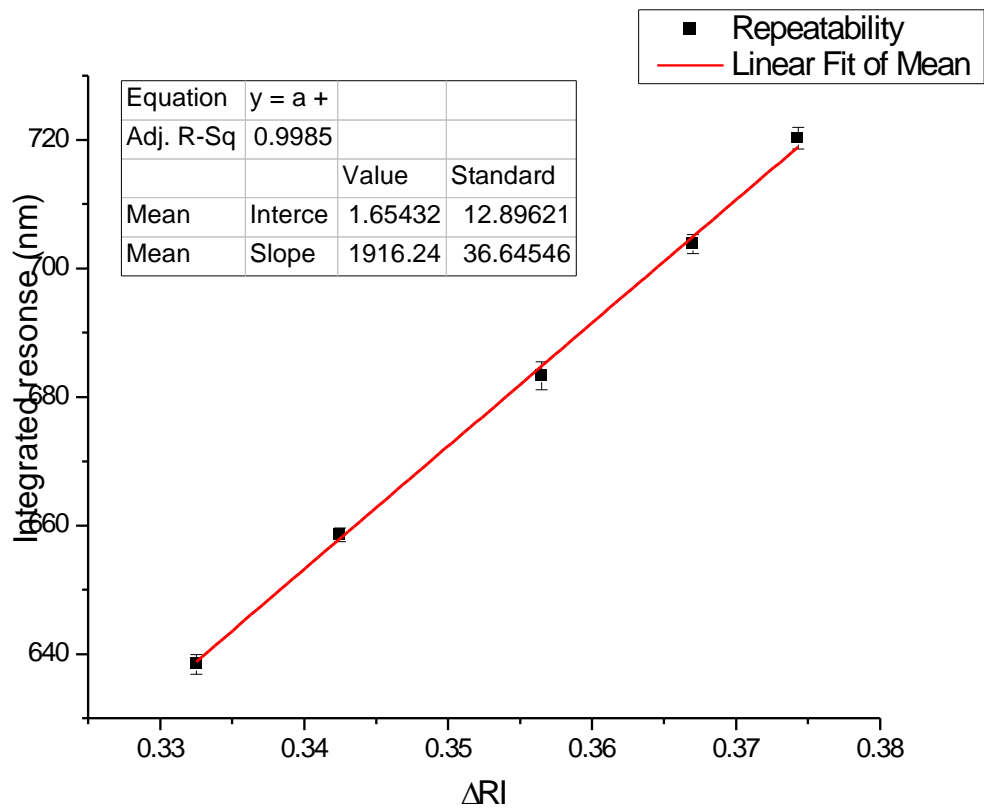


Figure 4-9. Evaluation of refractive index sensitivity and repeatability for hybrid nanopyramid arrays. The integrated total response was obtained from the area shifts from baseline spectrum to each spectrum. Standard deviation was calculated from triplicate measurements of three different areas on the array.

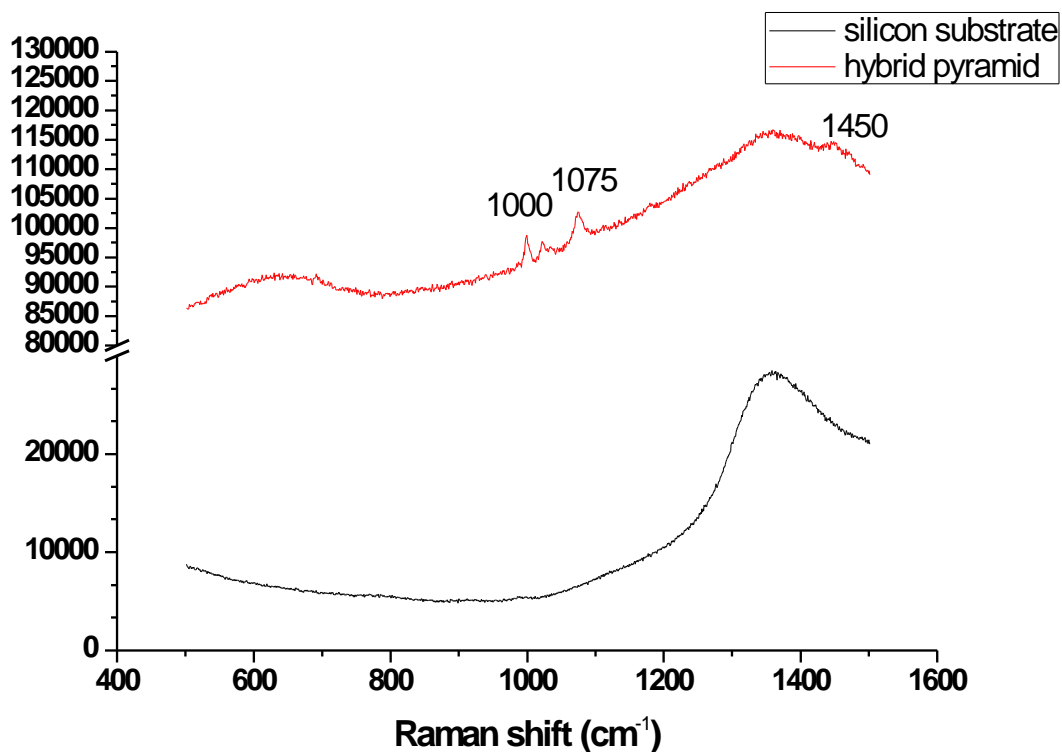


Figure 4-10. SERS spectra for characterizing the thrombin aptamer which is modified on the hybrid nanopyramid array and filled in the silicon wafer. The spectra were taken using a 785 nm diode laser with an integration time of 30 s. The Raman shift at 1000 cm^{-1} is associated with the phenylalanine protein and the deoxyribose vibration of the aptamer, the 1075 cm^{-1} shift was assigned to Guanidine triphosphate and the G-quadruplex, and the 1450 cm^{-1} shift is likely to result from CH₂ stretching mode or the G-quadruplex formation.

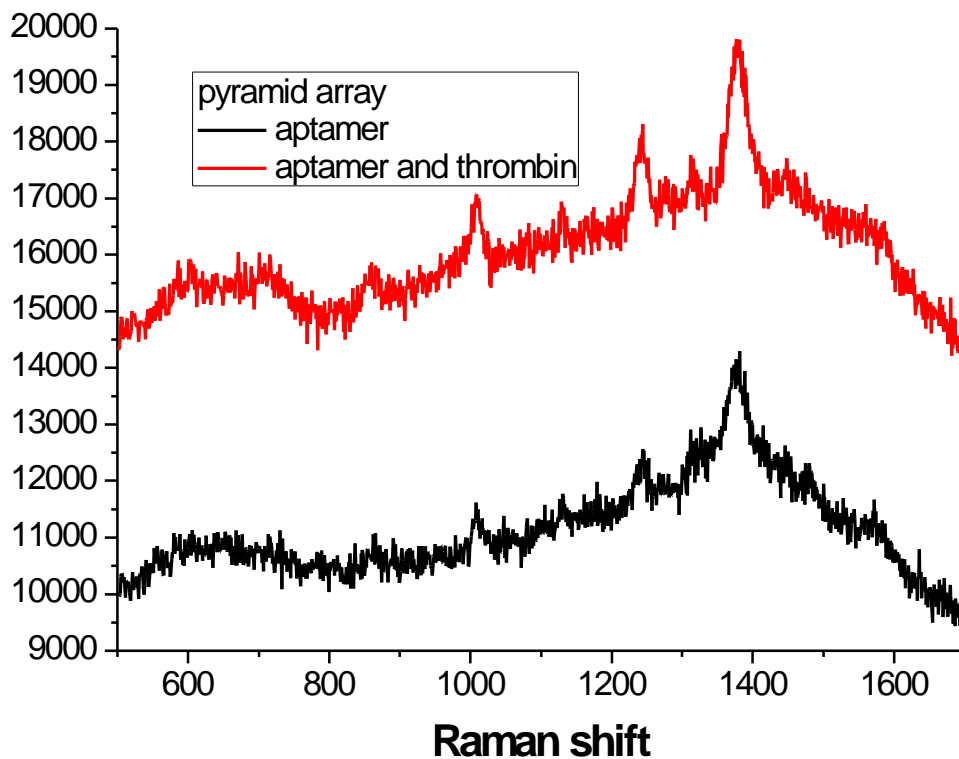


Figure 4-11. SERS spectra for characterizing the thrombin aptamer and the complex of thrombin aptamer-thrombin protein. The aptamer was already modified on the hybrid nanopyramid array. After characterizing this aptamer by using surface-enhanced Raman spectroscopy, thrombin protein solution was incubated for 30 min, and the corresponding SERS spectrum was recorded.

CHAPTER 5 CONCLUSIONS

Three types of chip-based plasmonic materials, gold nanoslit arrays, gold nanopyramid arrays, and hybrid nanopyramid arrays, are studied in this dissertation. All of the plasmonic materials generate strong SPP waves, and therefore enjoy a wide array of applications. This research particularly focuses on applying these plasmonic materials for label-free, high sensitivity, and real-time UV-Vis SPR and SERS sensing. The discussions in geometry designs, analysis method improvement, sensitivity optimization, cost-effective nanofabrication, and straightforward optical path are important for the development in a point-of-care SPR biosensors.

To enhance the understanding of the plasmonic effect, the relationship between various slit periodicity, different refractive indices, and corresponding spectra was carefully investigated. As a result, different types of SPP oscillations including BW-SPPs, slit-slit interference, LSPR, and Wood's anomalies were observed on the gold nanoslit array. Because of the multi-resonances generated by subwavelength apertures and the use of the multispectral analysis, the sensitivity of the gold nanoslit array is greatly improved. Of all the arrays tested, the 2 μm - periodicity array exhibits the best sensitivity for a value of 12000 nm/RIU which is the same as the prism-based SPR sensor. Moreover, the strong plasmonic effect also enables the application of SERS for qualitative biomolecular measurements.

Gold nanopyramid arrays were fabricated by the colloidal templating method, which offers advantages in its cost-effectiveness, tunable feasibility, and scalable fabrication. The simulated electromagnetic distributions by FDTD modeling showed a strong enhancement effect on the gold nanopyramid arrays, and the theoretical

computations also depicted spectrum shifts by altering the value of RI. The experimental results demonstrate that both of 45° and 0° excitations are capable of sensing trivial RI changes near the sensor surface and transduce RI changes into shifts in spectra. The sensitivity of the nanopyramid is 4000 nm/RIU and 2400 nm/RIU by using a 45° and 0° excitation mode respectively. To evaluate the efficacy of applying these arrays for biomolecular detections, one type of antibody, anti-alcohol dehydrogenase, was conjugated on the sensor surface to capture the target protein, alcohol dehydrogenase from yeast. The binding of anti-alcohol dehydrogenase and alcohol dehydrogenase shifted the peak wavelength from 595.9 nm to 602.3 nm with an excellent specificity.

Hybrid nanopyramid arrays composed of ETPTA polymer and a 30 nm thick of gold were fabricated by the same templating technology. FDTD modeling revealed the strong localized SPR surrounding the edges and tips of nanopyramids. Although the thickness of gold is only 30 nm, the strong enhancement for a value of 500 is achieved. The observed extraordinary transmission is 3.5 times higher than a flat gold substrate. By using the multispectral analysis, the sensitivity of hybrid nanopyramid arrays is 2000 nm/RIU with a good reproducibility and repeatability. The standard error of date to date variation and sensor to sensor variation is 130 nm/RIU and 37 nm/RIU respectively. Label-free and real-time bio-SERS sensing to thrombin DNA aptamer was also demonstrated on the hybrid arrays. The applicability of combining both of UV-Vis SPR and SERS techniques suggests a promising development in chip-based and label-free bioassay.

CHAPTER 6 FUTURE WORK

A bench top SPR system, Biacore from GE Healthcare, has been applied in studying biomolecular reactions for decades. The high sensitivity of up to 12000 nm/RIU and the real-time sensing are the most fascinated advantages. Although this system is powerful in a laboratory setting, it could not be applied for a point-of-care biosensor because of the issues in bulky instrument, the cost, and the throughput. The cost of each chip with only four sensing channels is 200 to 400 USD.

This study has demonstrated that a composition of nanostructured polymer and a thin metallic film can excite SPR without the use of a prism. Therefore, the instrumentation size can be scaled down. Moreover, the cost for making this hybrid substrate is greatly reduced. In general, the cost for making the substrate in a size of one inch by one inch is 10 USD, and this substrate can be broken down to hundreds of sensing arrays.

In this chapter, the hybrid nanopyramid array was applied for monitoring the biomolecular binding of antibody/protein and DNA aptamer/protein. The preliminary results are encouraging and should be validated in repeated acquisitions. The future work should also focus on an efficient generation process to wash away both of unabsorbed and adsorbed target protein. These improvements are needed for applying the hybrid nanopyramid array for detecting proteins in a complex biological samples such as tears, serum, or plasma.

6.1 Preliminary Experiments

The fabrication of hybrid nanopyramid arrays was described in section 4.2.1. Before the conjugation of biomolecules, the substrate was cleansed by an air-plasma

cleaner (PDC-32G, Harrick Scientific) at low power for 1 min to minimize contamination and enhance the binding. For the BSA detection, 20 μl of anti-BSA at 100 $\mu\text{g}/\text{ml}$ was incubated on the sample overnight at 4°C. After incubation, the gold nanopyramid substrate was rinsed three times with pH 7.4 PBS reconstituted from 10X PBS concentrate (BP399-500, Fisher) to wash away unabsorbed protein. After the substrate was assembled with a fluidic device and tubing, the integrated device was put on the sensing apparatus described in Chapter 4.2.2 for the transmission measurement. PBS was first injected to the device for recording a baseline spectrum, followed by different concentrations of BSA. At the final step, 0.1% casein diluted from 1% casein in PBS (PI-37528, Thermo) with PBS was injected to the device for evaluating the specificity.

For the thrombin detection, 30 μl of thrombin aptamer at 2 μM was incubated on the hybrid nanopyramid arrays overnight at 4°C. After incubation, the gold nanopyramid substrate was rinsed three times with pH 7.4 PBS to wash away unabsorbed protein. The assembled device was then put on the sensing apparatus for the transmission measurement. PBS was first injected to the device for recording a baseline spectrum, followed by different concentrations of thrombin solutions, and PBS was injected in the final step. To evaluate the effect of nonspecific binding, one of the thrombin detections was carried after adding a series dilution of BSA.

The monitoring of biomolecule binding event on the nanopyramid array is relatively straightforward compared with other immunoassay such as ELISA and Western blot. It is attributed to the label-free detection which overcomes the problems of interference and extensive labeling time. While the conjugation of biomolecules is happening at the metal/solution interface, an altered refractive index near the interface affects the

properties of SPPs, and therefore results in changed spectra obtained by a microscope-based measurement system [102]. The optical transmission system was chosen for hybrid nanopyramid arrays because of the unique property of extraordinary transmission and also an opportunity to integrate microfluidic system for rapid bioanalytical measurements.

6.2 Preliminary Results

To demonstrate the biosensing application on the hybrid nanopyramid arrays, anti-BSA and BSA were first used in the system. Figure 6-1 shows the preliminary real-time response to BSA and non-specific protein, casein. The total response is the integrated spectrum shift calculated by Equation 4-2. The baseline transmission applied in the equation was obtained from immersing arrays in PBS. At the beginning, adding PBS generated an attenuated total response which could result from losses of the weakly bound antibody. However, the total response stopped to decrease after adding 1.5 pM of BSA. Interestingly, when the array was exposed to 150 pM of BSA, the total response suddenly increased. It is possible that the captured BSA layer on the gold nanopyramid is thick enough to increase the effective optical length, and therefore enhances the transmission. As the concentrations of the BSA solutions increased, the total responses kept growing. However, the signal turned to a plateau because BSA gradually saturated the reaction sites.

It is important to validate the specificity for the transmission acquisition system because transmitted light through liquid solutions may be affected by a varied RI or by unbound protein residues in a solution. To evaluate the specificity of the BSA sensing on the hybrid nanopyramid array, a casein solution in PBS was injected after finishing the incubation of BSA at the highest concentration of 150 μM . Casein protein is a

common blocking protein from milk and should not react with either anti-BSA or BSA. It is worthwhile to mention that the concentration of casein is 435 μM which is much higher than any of the BSA solutions tested in Figure 6-1. After adding the casein solution, the total response was decreased to the same level as 15 nM of BSA and eventually stabilized. It is possible that 15 nM of BSA had already saturated the sensor, and the following BSA did not strongly bind to antibody. Meanwhile, the casein solution served as a washing solution and washed loosely bound. Figure 6-2 depicts the linear relationship between the concentration of BSA and the variation of total response. However, the result should be reproduced to verify this assumption.

To expand the variety of applicable biomolecules, the thrombin aptamer was also used on the hybrid nanopyramid array for detecting the thrombin protein. The reaction between the target analyte, thrombin protein, and the conjugated thrombin aptamer changes the configuration of biomolecular complex, and therefore results in an altered RI. Figure 6-3 shows the real-time thrombin detection on the hybrid nanopyramid arrays conjugated with a thrombin aptamer, and the total response is also calculated by Equation 4-2. The decreased total response after adding PBS can be explained by the detachment of the unabsorbed thrombin aptamer. The following injection of thrombin at 1 pM generated an increased signal and might be related to the binding of thrombin aptamer and thrombin. In addition, adding thrombin at 100 pM and 100 nM also created increased signals. The decreased signal shown in the final PBS washing holds a promise of specific detection, but the experiment should be replicated in the future.

A control experiment was also conducted on the thrombin aptamer modified arrays. Instead of adding thrombin protein, a serial dilution of BSA was injected to the

thrombin sensor for examining the specificity and also for blocking the free surface.

Figure 6-4 shows that the signal decreased continuously after adding the BSA solutions at a concentration ranging from 1 pM to 100 nM. This result is opposite to the signal obtained by adding thrombin protein to the sensor as shown in Figure 6-3.

A trivial amount of thrombin from 1 aM, 10 fM to 100 pM was also added on the array. As shown in Figure 6-5, a decreased signal was observed after adding PBS and casein. It should be noticed that Figure 6-3, 6-4, and 6-5 share the same characteristic that the signal reduced in a buffer or non-specific protein solution. Figure 6-5 shows that adding thrombin protein at 1 aM caused an increased signal at the beginning, but later went back to the baseline. The flat line that connects the starting and the ending point of this incubation explains the binding was not sensed on the arrays. On the other hand, the gradient of connected line was increased for the incubation of thrombin protein at 10 fM and 100 pM.

In summary, the hybrid nanopyramid SPR sensor provides compelling advantages in the cost-effective fabrication and high sensitivity to RI changes. To develop this array for a point-of-care biosensor, both antibody and aptamer were applied on the arrays and generated encouraging results. The data shown here is a good starting point, and the next stage is to reproduce the results, design an optimal protocol for antibody and aptamer conjugation on the sensor, and apply an effective regeneration procedure for a wider sensing dynamic range. An important question for future studies is to determine the detection limit and the dynamic range of the nanopyramid array. Future work of developing a dual sensing system is also important for applying complex samples such as human plasma or blood. As shown in Figure 6-6, the dual sensing system is

designed to subtract the control spectra from the spectra generated from the real binding. The control spectra are obtained from the sensing channel without antibody conjugation, and the purpose of this design is to reduce the noise generated from the non-specific protein residues in the solution.

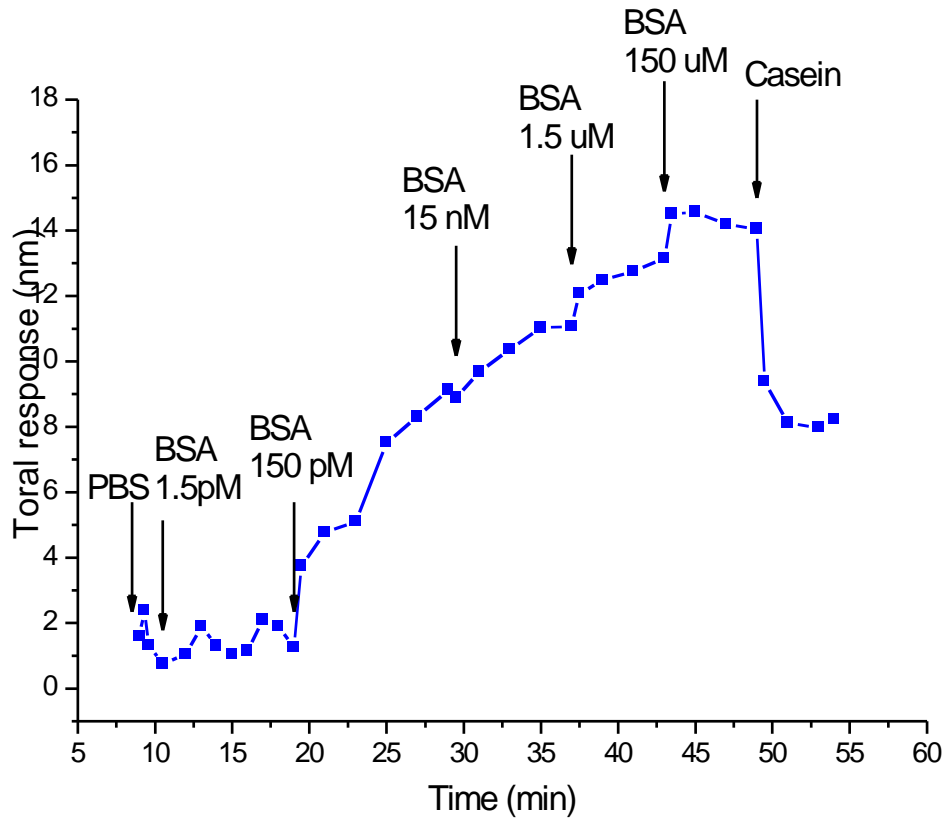


Figure 6-1. Real-time biosensing for anti-BSA and BSA binding. Total response was obtained from the multispectral analysis. Casein protein is used to verify the specificity of the sensor. After adding casein, the total response was decreased and eventually stabilized.

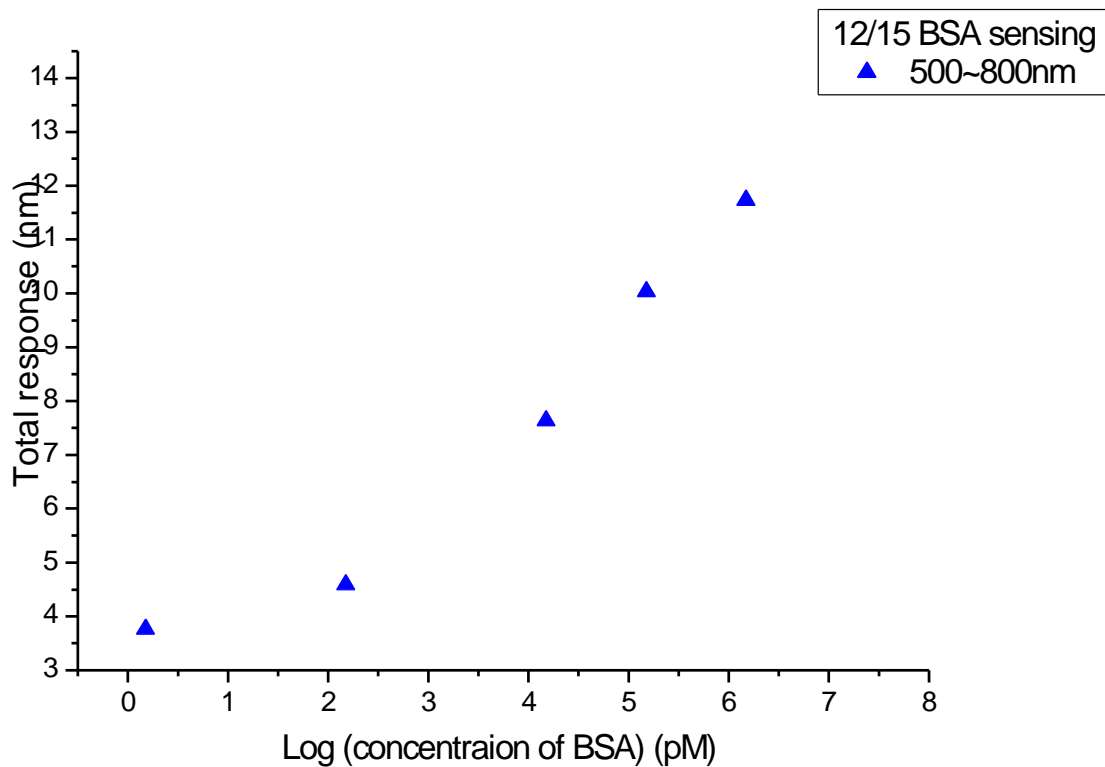


Figure 6-2. Concentration calibration of BSA detection. Detected total response versus the logarithm of concentrations of BSA was plotted to obtain the detection

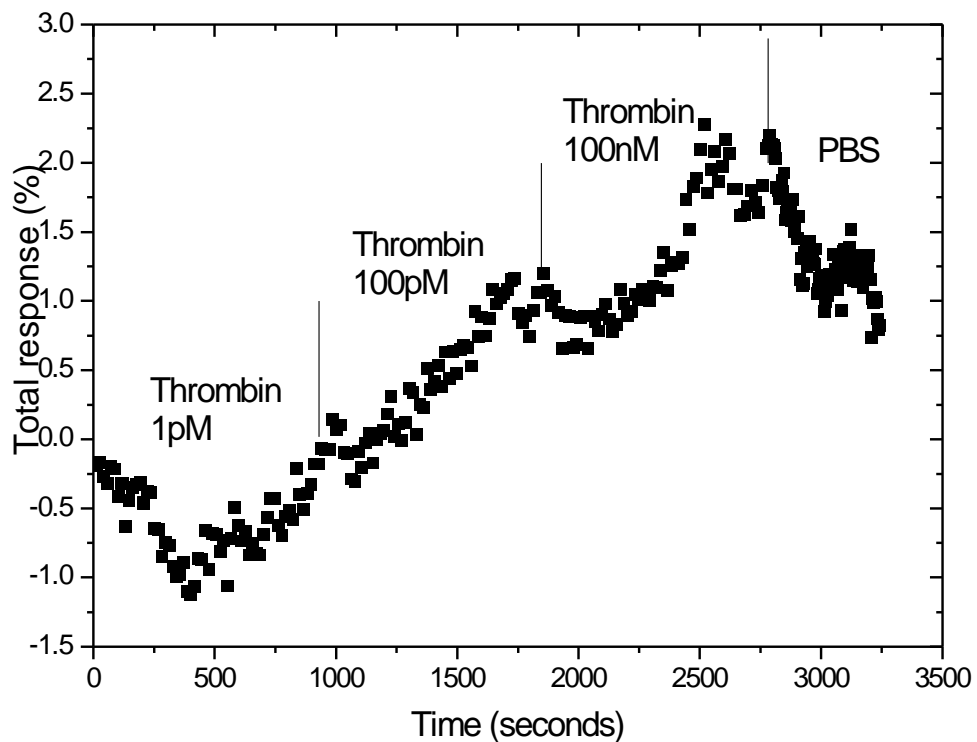


Figure 6-3. Real-time human thrombin detection. To conjugated thrombin aptamer on the surface, the hybrid nanopyramid substrate was immersed in thrombin aptamer solution overnight. The substrate was then washed by sufficient PBS at and exposed to a serial dilution of thrombin protein. The total response was calculated by using the multispectral analysis equation.

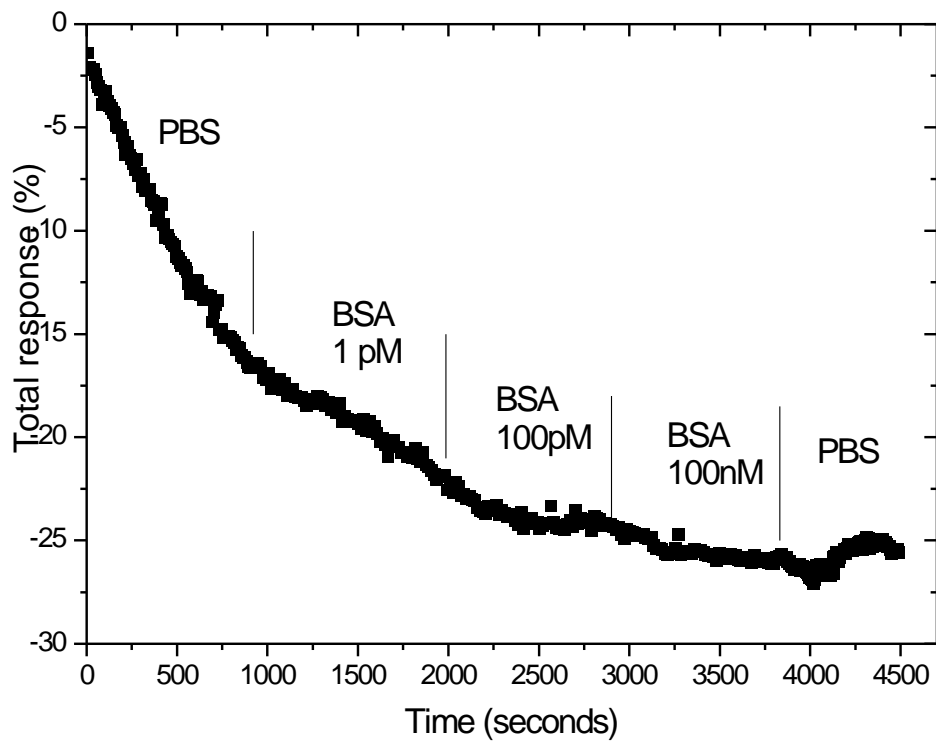


Figure 6-4. Adding BSA to the thrombin sensor.

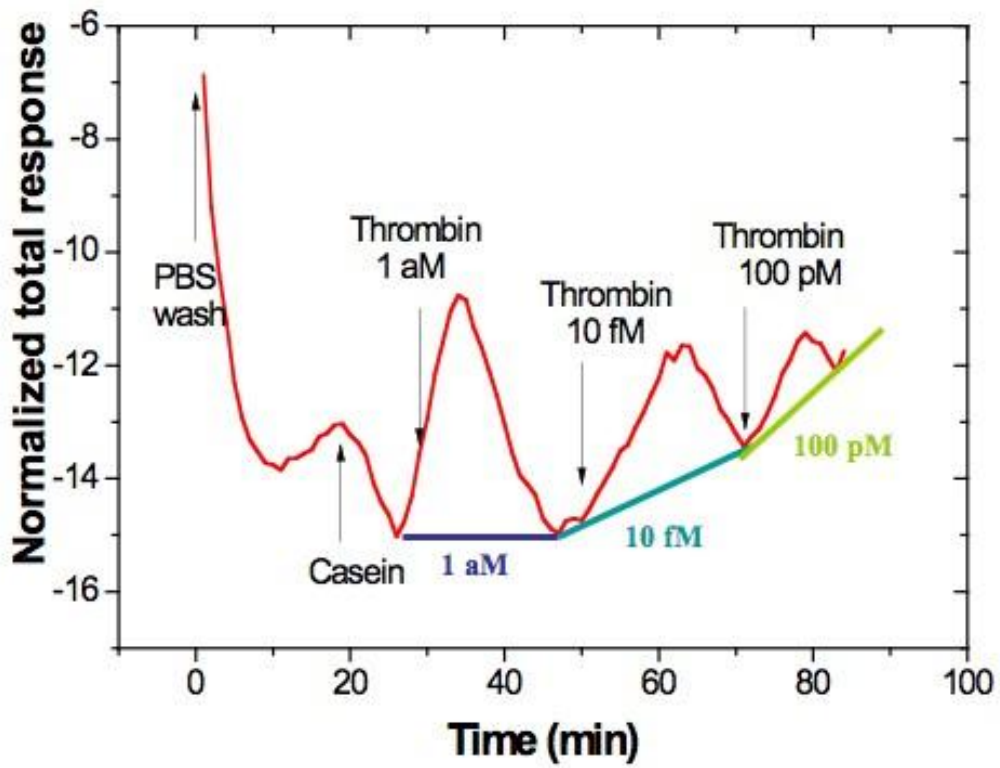
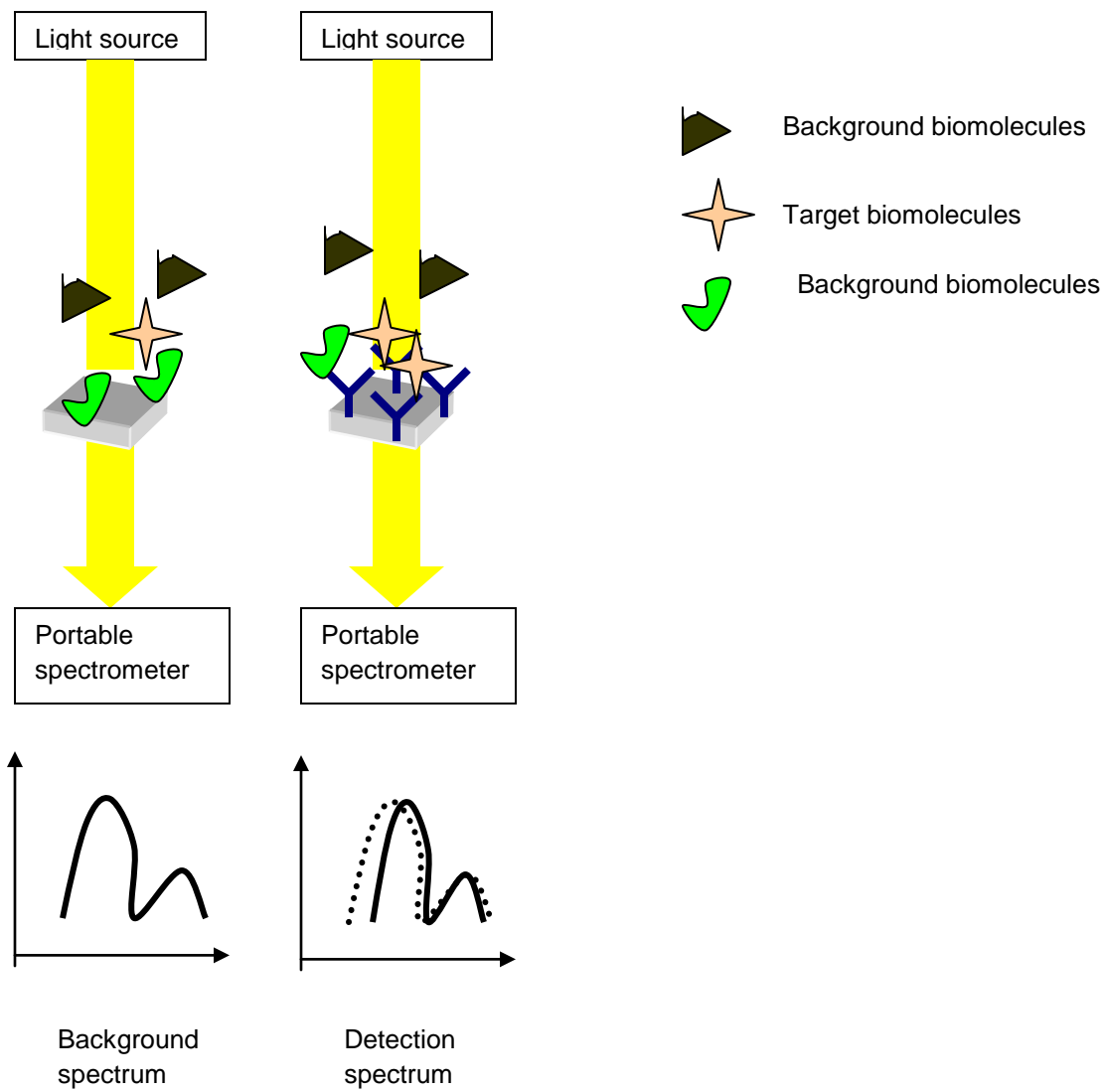


Figure 6-5. The trivial amount of thrombin protein on the sensor.



Real spectrum = Detection spectrum – Background spectrum

Figure 6-6. Schematic of a dual sensing system.

LIST OF REFERENCES

- [1] N. A. Campbell and J. B. Reece, *Biology*, 7th ed. San Francisco: Pearson Benjamin Cummings, 2005.
- [2] J. M. Berg, J. L. Tymoczko, L. Stryer, and L. Stryer, *Biochemistry*, 6th ed. New York: W., 2007.
- [3] M. P. Hacker, W. S. Messer, K. A. Bachmann, and ScienceDirect (Online service), *Pharmacology principles and practice*. London: Academic, 2009.
- [4] S. R. Mikkelsen and E. Cort on, *Bioanalytical chemistry*. Hoboken, N.J.: John Wiley & Sons, 2004.
- [5] G. œ. Marko-Varga and P. Oroszlan, *Emerging technologies in protein and genomic material anaylsis*, 1st ed. Amsterdam ; Boston: Elsevier, 2003.
- [6] A. Brajter-Toth and J. Q. Chambers, *Electroanalytical methods for biological materials*. New York: Marcel Dekker, 2002.
- [7] A. Rasooly and K. E. Herold, *Biosensors and Biodetection Methods and Protocols, Volume 2: Electrochemical and Mechanical Detectors, Lateral Flow and Ligands for Biosensors*. New York Secaucus: Humana Press Springer Distributor, 2009.
- [8] A. Offenhausser and R. Rinaldi, *Nanobioelectronics for electronics, biology, and medicine*. New York: Springer, 2009.
- [9] N. J. d. Mol and M. J. E. Fischer, *Surface plasmon resonance : methods and protocols*. New York: Humana Press, 2010.
- [10] P. N. Floriano, *Microchip-based assay systems methods and applications*. Totowa, N.J.: Humana Press, 2007.
- [11] N. Raghunathan and O. S. Wolfbeis, *Optical sensors : industrial, environmental and diagnostic applications*. Berlin ; London: Springer, 2004.
- [12] A. L. Hook, H. Thissen, and N. H. Voelcker, "Surface plasmon resonance imaging of polymer microarrays to study protein-polymer interactions in high throughput," *Langmuir*, vol. 25, pp. 9173-81, Aug 18 2009.

- [13] H. Im, A. Lesuffleur, N. C. Lindquist, and S. H. Oh, "Plasmonic nanoholes in a multichannel microarray format for parallel kinetic assays and differential sensing," *Anal Chem*, vol. 81, pp. 2854-9, Apr 15 2009.
- [14] J. Ji, J. G. O'Connell, D. J. Carter, and D. N. Larson, "High-throughput nanohole array based system to monitor multiple binding events in real time," *Anal Chem*, vol. 80, pp. 2491-8, Apr 1 2008.
- [15] S. L. Lai, S. Huang, X. Bi, and K. L. Yang, "Optical imaging of surface-immobilized oligonucleotide probes on DNA microarrays using liquid crystals," *Langmuir*, vol. 25, pp. 311-6, Jan 6 2009.
- [16] I. Mannelli, L. Lecerf, M. Guerrouache, M. Goossens, M. C. Millot, and M. Canva, "DNA immobilisation procedures for surface plasmon resonance imaging (SPRI) based microarray systems," *Biosens Bioelectron*, vol. 22, pp. 803-9, Jan 15 2007.
- [17] G. J. Wegner, A. W. Wark, H. J. Lee, E. Codner, T. Saeki, S. Fang, and R. M. Corn, "Real-time surface plasmon resonance imaging measurements for the multiplexed determination of protein adsorption/desorption kinetics and surface enzymatic reactions on peptide microarrays," *Anal Chem*, vol. 76, pp. 5677-84, Oct 1 2004.
- [18] R. Wood, "Uneven Distribution of Balance," in *Philosophical Magazine*. vol. 4, 1902, p. 396.
- [19] U. Fano, "The Theory of Anomalous Diffraction Gratings and of Quasi-Stationary Waves on Metallic Surfaces (Sommerfeld's Waves)," *J. Opt. Soc. Am.*, vol. 31, pp. 213-222, 1941.
- [20] T. Turbadar, "Complete Absorption of Light by Thin Metal Films," *Proceedings of the Physical Society*, vol. 74, 1959.
- [21] A. Otto, "Excitation of nonradiative surface plasma waves in silver by the method of frustrated total reflection," *Zeitschrift für Physik A Hadrons and Nuclei*, vol. 216, pp. 398-410, 1968.
- [22] R. H. Ritchie, "Plasma Losses by Fast Electrons in Thin Films," *Physical Review*, vol. 106, p. 874, 1957.
- [23] W. L. Barnes, A. Dereux, and T. W. Ebbesen, "Surface plasmon subwavelength optics," *Nature*, vol. 424, pp. 824-30, Aug 14 2003.

- [24] J. Homola, S. S. Yee, and G. n. Gauglitz, "Surface plasmon resonance sensors: review," *Sensors and Actuators B: Chemical*, vol. 54, pp. 3-15, 1999.
- [25] E. Kretschmann, "The angular dependence and the polarisation of light emitted by surface plasmons on metals due to roughness," *Optics Communications*, vol. 5, pp. 331-336, 1972.
- [26] R. Bruns and H. Raether, "Plasma resonance radiation from non radiative plasmons," *Zeitschrift für Physik A Hadrons and Nuclei*, vol. 237, pp. 98-106, 1970.
- [27] A. Dahlin, M. Zach, T. Rindzevicius, M. Kall, D. S. Sutherland, and F. Hook, "Localized surface plasmon resonance sensing of lipid-membrane-mediated biorecognition events," *J Am Chem Soc*, vol. 127, pp. 5043-8, Apr 13 2005.
- [28] T. Akimoto, S. Wada, and I. Karube, "A surface plasmon resonance probe without optical fibers as a portable sensing device," *Anal Chim Acta*, vol. 610, pp. 119-24, Mar 3 2008.
- [29] A. Battula, S. Chen, Y. Lu, R. J. Knize, and K. Reinhardt, "Tuning the extraordinary optical transmission through subwavelength hole array by applying a magnetic field," *Opt Lett*, vol. 32, pp. 2692-4, Sep 15 2007.
- [30] J. Henzie, J. Lee, M. H. Lee, W. Hasan, and T. W. Odom, "Nanofabrication of plasmonic structures," *Annu Rev Phys Chem*, vol. 60, pp. 147-65, 2009.
- [31] J. Henzie, M. H. Lee, and T. W. Odom, "Multiscale patterning of plasmonic metamaterials," *Nat Nanotechnol*, vol. 2, pp. 549-54, Sep 2007.
- [32] N. A. Abu Hatab, J. M. Oran, and M. J. Sepaniak, "Surface-enhanced Raman spectroscopy substrates created via electron beam lithography and nanotransfer printing," *ACS Nano*, vol. 2, pp. 377-85, Feb 2008.
- [33] C. Chen, J. A. Hutchison, P. Van Dorpe, R. Kox, I. De Vlaminck, I. H. Uji, J. Hofkens, L. Lagae, G. Maes, and G. Borghs, "Focusing plasmons in nanoslits for surface-enhanced Raman scattering," *Small*, vol. 5, pp. 2876-82, Dec 2009.

- [34] N. C. Linn, C. H. Sun, A. Arya, P. Jiang, and B. Jiang, "Surface-enhanced Raman scattering on periodic metal nanotips with tunable sharpness," *Nanotechnology*, vol. 20, p. 225303, Jun 3 2009.
- [35] P. K. Wilson, T. Jiang, M. E. Minunni, A. P. Turner, and M. Mascini, "A novel optical biosensor format for the detection of clinically relevant TP53 mutations," *Biosens Bioelectron*, vol. 20, pp. 2310-3, May 15 2005.
- [36] W. Zhou, H. Gao, and T. W. Odom, "Toward broadband plasmonics: tuning dispersion in rhombic plasmonic crystals," *ACS Nano*, vol. 4, pp. 1241-7, Feb 23 2010.
- [37] M. E. Stewart, J. Yao, J. Maria, S. K. Gray, J. A. Rogers, and R. G. Nuzzo, "Multispectral Thin Film Biosensing and Quantitative Imaging Using 3D Plasmonic Crystals," *Anal Chem*, Jul 10 2009.
- [38] K. Okamoto, I. Niki, A. Shvartser, Y. Narukawa, T. Mukai, and A. Scherer, "Surface-plasmon-enhanced light emitters based on InGaN quantum wells," *Nat Mater*, vol. 3, pp. 601-5, Sep 2004.
- [39] C. W. Shen, J. Y. Wang, W. H. Chuang, H. L. Chen, Y. C. Lu, Y. W. Kiang, C. C. Yang, and Y. J. Yang, "Effective energy coupling and preservation in a surface plasmon-light emitter coupling system on a metal nanostructure," *Nanotechnology*, vol. 20, p. 135202, Apr 1 2009.
- [40] N. Fang, H. Lee, C. Sun, and X. Zhang, "Sub-Diffraction-Limited Optical Imaging with a Silver Superlens," *Science*, vol. 308, pp. 534-537, April 22, 2005 2005.
- [41] W. Dickson, G. A. Wurtz, P. R. Evans, R. J. Pollard, and A. V. Zayats, "Electronically controlled surface plasmon dispersion and optical transmission through metallic hole arrays using liquid crystal," *Nano Lett*, vol. 8, pp. 281-6, Jan 2008.
- [42] J. Frischeisen, C. Mayr, N. A. Reinke, S. Nowy, and W. Brutting, "Surface plasmon resonance sensor utilizing an integrated organic light emitting diode," *Opt Express*, vol. 16, pp. 18426-36, Oct 27 2008.
- [43] B. Liedberg, C. Nylander, and I. Lunström, "Surface plasmon resonance for gas detection and biosensing," *Sensors and Actuators*, vol. 4, pp. 299-304, 1983.

- [44] N. Nath and A. Chilkoti, "Label-Free Biosensing by Surface Plasmon Resonance of Nanoparticles on Glass: Optimization of Nanoparticle Size," *Analytical Chemistry*, vol. 76, pp. 5370-5378, 08/05/ 2004.
- [45] M. E. Stewart, N. H. Mack, V. Malyarchuk, J. A. Soares, T. W. Lee, S. K. Gray, R. G. Nuzzo, and J. A. Rogers, "Quantitative multispectral biosensing and 1D imaging using quasi-3D plasmonic crystals," *Proc Natl Acad Sci U S A*, vol. 103, pp. 17143-8, Nov 14 2006.
- [46] H. Gao, J. Henzie, M. H. Lee, and T. W. Odom, "Screening plasmonic materials using pyramidal gratings," *Proc Natl Acad Sci U S A*, vol. 105, pp. 20146-51, Dec 23 2008.
- [47] S. H. Chang, S. Gray, and G. Schatz, "Surface plasmon generation and light transmission by isolated nanoholes and arrays of nanoholes in thin metal films," *Opt Express*, vol. 13, pp. 3150-65, Apr 18 2005.
- [48] T. H. Park, N. Mirin, J. B. Lassiter, C. L. Nehl, N. J. Halas, and P. Nordlander, "Optical properties of a nanosized hole in a thin metallic film," *ACS Nano*, vol. 2, pp. 25-32, Jan 2008.
- [49] S. Wedge and W. Barnes, "Surface plasmon-polariton mediated light emission through thin metal films," *Opt Express*, vol. 12, pp. 3673-85, Aug 9 2004.
- [50] J. P. Hoogenboom, G. Sanchez-Mosteiro, G. Colas des Francs, D. Heinis, G. Legay, A. Dereux, and N. F. van Hulst, "The single molecule probe: nanoscale vectorial mapping of photonic mode density in a metal nanocavity," *Nano Lett*, vol. 9, pp. 1189-95, Mar 2009.
- [51] B. Min, E. Ostby, V. Sorger, E. Ulin-Avila, L. Yang, X. Zhang, and K. Vahala, "High-Q surface-plasmon-polariton whispering-gallery microcavity," *Nature*, vol. 457, pp. 455-8, Jan 22 2009.
- [52] L. Feuz, P. Jonsson, M. P. Jonsson, and F. Hook, "Improving the limit of detection of nanoscale sensors by directed binding to high-sensitivity areas," *ACS Nano*, vol. 4, pp. 2167-77, Apr 27 2010.
- [53] R. J. Green, J. Davies, M. C. Davies, C. J. Roberts, and S. J. Tendler, "Surface plasmon resonance for real time in situ analysis of protein adsorption to polymer surfaces," *Biomaterials*, vol. 18, pp. 405-13, Mar 1997.

- [54] J. Homola, "Surface plasmon resonance sensors for detection of chemical and biological species," *Chem Rev*, vol. 108, pp. 462-93, Feb 2008.
- [55] H. Liu and P. Lalanne, "Microscopic theory of the extraordinary optical transmission," *Nature*, vol. 452, pp. 728-31, Apr 10 2008.
- [56] D. P. Lyvers, J. M. Moon, A. V. Kildishev, V. M. Shalaev, and A. Wei, "Gold nanorod arrays as plasmonic cavity resonators," *ACS Nano*, vol. 2, pp. 2569-76, Dec 23 2008.
- [57] K. M. Mayer, S. Lee, H. Liao, B. C. Rostro, A. Fuentes, P. T. Scully, C. L. Nehl, and J. H. Hafner, "A label-free immunoassay based upon localized surface plasmon resonance of gold nanorods," *ACS Nano*, vol. 2, pp. 687-92, Apr 2008.
- [58] J. McPhillips, A. Murphy, M. P. Jonsson, W. R. Hendren, R. Atkinson, F. Hook, A. V. Zayats, and R. J. Pollard, "High-performance biosensing using arrays of plasmonic nanotubes," *ACS Nano*, vol. 4, pp. 2210-6, Apr 27 2010.
- [59] H. M. Hiep, H. Yoshikawa, M. Saito, and E. Tamiya, "An interference localized surface plasmon resonance biosensor based on the photonic structure of Au nanoparticles and SiO₂/Si multilayers," *ACS Nano*, vol. 3, pp. 446-52, Feb 24 2009.
- [60] L. J. Sherry, R. Jin, C. A. Mirkin, G. C. Schatz, and R. P. Van Duyne, "Localized surface plasmon resonance spectroscopy of single silver triangular nanoprisms," *Nano Lett*, vol. 6, pp. 2060-5, Sep 2006.
- [61] S. Y. Chuang, H. L. Chen, S. S. Kuo, Y. H. Lai, and C. C. Lee, "Using direct nanoimprinting to study extraordinary transmission in textured metal films," *Opt Express*, vol. 16, pp. 2415-22, Feb 18 2008.
- [62] T. H. Reilly, R. C. Tenent, T. M. Barnes, K. L. Rowlen, and J. van de Lagemaat, "Controlling the optical properties of plasmonic disordered nanohole silver films," *ACS Nano*, vol. 4, pp. 615-24, Feb 23 2010.
- [63] H. Im, N. C. Lindquist, A. Lesuffleur, and S. H. Oh, "Atomic layer deposition of dielectric overlayers for enhancing the optical properties and chemical stability of plasmonic nanoholes," *ACS Nano*, vol. 4, pp. 947-54, Feb 23 2010.

- [64] E. Ouellet, C. Lausted, T. Lin, C. W. Yang, L. Hood, and E. T. Lagally, "Parallel microfluidic surface plasmon resonance imaging arrays," *Lab Chip*, vol. 10, pp. 581-8, Mar 7 2010.
- [65] M. Sukharev, P. R. Sievert, T. Seideman, and J. B. Ketterson, "Perfect coupling of light to surface plasmons with ultra-narrow linewidths," *J Chem Phys*, vol. 131, p. 034708, Jul 21 2009.
- [66] Y. W. Jiang, L. D. Tzuang, Y. H. Ye, Y. T. Wu, M. W. Tsai, C. Y. Chen, and S. C. Lee, "Effect of Wood's anomalies on the profile of extraordinary transmission spectra through metal periodic arrays of rectangular subwavelength holes with different aspect ratio," *Opt Express*, vol. 17, pp. 2631-7, Feb 16 2009.
- [67] J. Cazes and G. W. Ewing, *Ewing's analytical instrumentation handbook*, 3rd ed. New York: Marcel Dekker, 2005.
- [68] I. R. Lewis and H. G. M. Edwards, *Handbook of Raman spectroscopy : from the research laboratory to the process line*. New York: Marcel Dekker, 2001.
- [69] B. Yan, A. Thubagere, W. R. Premasiri, L. D. Ziegler, L. Dal Negro, and B. M. Reinhard, "Engineered SERS substrates with multiscale signal enhancement: nanoparticle cluster arrays," *ACS Nano*, vol. 3, pp. 1190-202, May 26 2009.
- [70] J. Gamby, A. Rudolf, M. Abid, H. H. Girault, C. Deslouis, and B. Tribollet, "Polycarbonate microchannel network with carpet of gold nanowires as SERS-active device," *Lab Chip*, vol. 9, pp. 1806-8, Jun 21 2009.
- [71] Z. Q. Tian, B. Ren, J. F. Li, and Z. L. Yang, "Expanding generality of surface-enhanced Raman spectroscopy with borrowing SERS activity strategy," *Chem Commun (Camb)*, pp. 3514-34, Sep 14 2007.
- [72] W. R. Premasiri, D. T. Moir, M. S. Klempner, N. Krieger, G. Jones, 2nd, and L. D. Ziegler, "Characterization of the surface enhanced raman scattering (SERS) of bacteria," *J Phys Chem B*, vol. 109, pp. 312-20, Jan 13 2005.
- [73] S. Cintra, M. E. Abdelsalam, P. N. Bartlett, J. J. Baumberg, T. A. Kelf, Y. Sugawara, and A. E. Russell, "Sculpted substrates for SERS," *Faraday Discuss*, vol. 132, pp. 191-9; discussion 227-47, 2006.

- [74] M. H. Lee, H. Gao, and T. W. Odom, "Refractive Index Sensing Using Quasi One-Dimensional Nanoslit Arrays," *Nano Letters*, vol. 9, pp. 2584-2588, 06/03/ 2009.
- [75] S. Selcuk, K. Woo, D. B. Tanner, A. F. Hebard, A. G. Borisov, and S. V. Shabanov, "Trapped electromagnetic modes and scaling in the transmittance of perforated metal films," *Phys Rev Lett*, vol. 97, p. 067403, Aug 11 2006.
- [76] L. Yin, V. K. Vlasko-Vlasov, A. Rydh, J. Pearson, U. Welp, S. H. Chang, S. K. Gray, G. C. Schatz, D. B. Brown, and C. W. Kimball, "Surface plasmons at single nanoholes in Au films," *Applied Physics Letters*, vol. 85, pp. 467-469, 2004.
- [77] P.-K. Wei, H.-L. Chou, Y.-R. Cheng, C.-H. Wei, W. Fann, and J. O. Tegenfeldt, "Beaming effect of optical near-field in multiple metallic slits with nanometric linewidth and micrometer pitch," *Optics Communications*, vol. 253, pp. 198-204, 2005.
- [78] E. S. Kwak, J. Henzie, S. H. Chang, S. K. Gray, G. C. Schatz, and T. W. Odom, "Surface plasmon standing waves in large-area subwavelength hole arrays," *Nano Lett*, vol. 5, pp. 1963-7, Oct 2005.
- [79] H. Gao, J. Henzie, and T. W. Odom, "Direct evidence for surface plasmon-mediated enhanced light transmission through metallic nanohole arrays," *Nano Lett*, vol. 6, pp. 2104-8, Sep 2006.
- [80] G. Leveque and O. J. Martin, "Optical interactions in a plasmonic particle coupled to a metallic film," *Opt Express*, vol. 14, pp. 9971-81, Oct 16 2006.
- [81] M. E. Stewart, C. R. Anderton, L. B. Thompson, J. Maria, S. K. Gray, J. A. Rogers, and R. G. Nuzzo, "Nanostructured plasmonic sensors," *Chem Rev*, vol. 108, pp. 494-521, Feb 2008.
- [82] J. Prikulis, P. Hanarp, L. Olofsson, D. Sutherland, and M. Kall, "Optical Spectroscopy of Nanometric Holes in Thin Gold Films," *Nano Letters*, vol. 4, pp. 1003-1007, 04/27/ 2004.
- [83] Z. Sun and X. Zuo, "Tuning resonant optical transmission of metallic nanoslit arrays with embedded microcavities," *Opt Lett*, vol. 34, pp. 1411-3, May 1 2009.

- [84] A. Mary, S. G. Rodrigo, L. Martín-Moreno, and F. J. García-Vidal, "Theory of light transmission through an array of rectangular holes," *Physical Review B*, vol. 76, p. 195414, 2007.
- [85] Y. S. Jung, J. Wuenschell, H. K. Kim, P. Kaur, and D. H. Waldeck, "Blue-shift of surface plasmon resonance in a metal nanoslit array structure," *Opt Express*, vol. 17, pp. 16081-91, Aug 31 2009.
- [86] E. Ozbay, "Plasmonics: Merging Photonics and Electronics at Nanoscale Dimensions," *Science*, vol. 311, pp. 189-193, January 13, 2006 2006.
- [87] M. R. Aguilar, A. Gallardo, L. M. Lechuga, A. Calle, and J. San Roman, "Modulation of proteins adsorption onto the surface of chitosan complexed with anionic copolymers. Real time analysis by surface plasmon resonance," *Macromol Biosci*, vol. 4, pp. 631-8, Jul 14 2004.
- [88] A. J. Haes, L. Chang, W. L. Klein, and R. P. Van Duyne, "Detection of a Biomarker for Alzheimer's Disease from Synthetic and Clinical Samples Using a Nanoscale Optical Biosensor," *Journal of the American Chemical Society*, vol. 127, pp. 2264-2271, 01/27 2005.
- [89] B.-K. Oh, Y.-K. Kim, K. W. Park, W. H. Lee, and J.-W. Choi, "Surface plasmon resonance immunosensor for the detection of Salmonella typhimurium," *Biosensors and Bioelectronics*, vol. 19, pp. 1497-1504, 2004.
- [90] D. Sarkar and P. Somasundaran, "Polymer surfactant kinetics using surface plasmon resonance spectroscopy dodecyltrimethylammonium chloride/polyacrylic acid system," *Journal of Colloid and Interface Science*, vol. 261, pp. 197-205, 2003.
- [91] M. P. Jonsson, P. Jonsson, A. B. Dahlin, and F. Hook, "Supported Lipid Bilayer Formation and Lipid-Membrane-Mediated Biorecognition Reactions Studied with a New Nanoplasmonic Sensor Template," *Nano Letters*, vol. 7, pp. 3462-3468, 09/29 2007.
- [92] C. Hempen and U. Karst, "Labeling strategies for bioassays," *Anal Bioanal Chem*, vol. 384, pp. 572-83, Feb 2006.

- [93] H. Yu, J. W. Raymond, T. M. McMahon, and A. A. Campagnari, "Detection of biological threat agents by immunomagnetic microsphere-based solid phase fluorogenic- and electro-chemiluminescence," *Biosens Bioelectron*, vol. 14, pp. 829-40, Jan 2000.
- [94] X. Shan, X. Huang, K. J. Foley, P. Zhang, K. Chen, S. Wang, and N. Tao, "Measuring surface charge density and particle height using surface plasmon resonance technique," *Anal Chem*, vol. 82, pp. 234-40, Jan 1 2009.
- [95] T. A. Bendikov, A. Rabinkov, T. Karakouz, A. Vaskevich, and I. Rubinstein, "Biological Sensing and Interface Design in Gold Island Film Based Localized Plasmon Transducers," *Analytical Chemistry*, vol. 80, pp. 7487-7498, 08/29 2008.
- [96] J. Ferreira, M. J. Santos, M. M. Rahman, A. G. Brolo, R. Gordon, D. Sinton, and E. M. Girotto, "Attomolar protein detection using in-hole surface plasmon resonance," *J Am Chem Soc*, vol. 131, pp. 436-7, Jan 21 2009.
- [97] C.-J. Heo, S.-H. Kim, S. G. Jang, S. Y. Lee, and S.-M. Yang, "Gold "Nanogrills" with Tunable Dipolar Multiple Plasmon Resonances," *Advanced Materials*, vol. 21, pp. 1726-1731, 2009.
- [98] P. Nagpal, N. C. Lindquist, S.-H. Oh, and D. J. Norris, "Ultrasoother Patterned Metals for Plasmonics and Metamaterials," *Science*, vol. 325, pp. 594-597, July 31, 2009 2009.
- [99] T.-H. Lin, N. C. Linn, L. Tarajano, B. Jiang, and P. Jiang, "Electrochemical SERS at Periodic Metallic Nanopyramid Arrays," *The Journal of Physical Chemistry C*, vol. 113, pp. 1367-1372, 01/07 2009.
- [100] J. Homola, M. Piliarik, and J. Homola, "SPR Sensor Instrumentation," in *Surface Plasmon Resonance Based Sensors*. vol. 4: Springer Berlin Heidelberg, 2006, pp. 95-116.
- [101] H. Zhu, M. Bilgin, R. Bangham, D. Hall, A. Casamayor, P. Bertone, N. Lan, R. Jansen, S. Bidlingmaier, T. Houfek, T. Mitchell, P. Miller, R. A. Dean, M. Gerstein, and M. Snyder, "Global analysis of protein activities using proteome chips," *Science*, vol. 293, pp. 2101-5, Sep 14 2001.

- [102] J. C. Yang, J. Ji, J. M. Hogle, and D. N. Larson, "Metallic nanohole arrays on fluoropolymer substrates as small label-free real-time bioprobes," *Nano Lett*, vol. 8, pp. 2718-24, Sep 2008.
- [103] M. J. Levene, J. Korklach, S. W. Turner, M. Foquet, H. G. Craighead, and W. W. Webb, "Zero-mode waveguides for single-molecule analysis at high concentrations," *Science*, vol. 299, pp. 682-6, Jan 31 2003.
- [104] V. Lomakin, M. Lu, and E. Michielssen, "Optical wave properties of nanoparticle chains coupled with a metal surface," *Opt Express*, vol. 15, pp. 11827-42, Sep 17 2007.
- [105] J. Maria, T. T. Truong, J. Yao, T.-W. Lee, R. G. Nuzzo, S. Leyffer, S. K. Gray, and J. A. Rogers, "Optimization of 3D Plasmonic Crystal Structures for Refractive Index Sensing," *The Journal of Physical Chemistry C*, vol. 113, pp. 10493-10499, 05/21/ 2009.

BIOGRAPHICAL SKETCH

Pei-Yu Chung received her B.S. degree in Bio-Industrial Mechatronics Engineering at National Taiwan University in 2006 and was admitted to the Ph.D. program in the Department of Materials Science and Engineering at University of Florida in 2007. She joined Dr. Christopher Batich's group and became a doctoral candidate in 2008. For her Ph.D., she conducted research on the development of optoelectronic plasmonic diagnostic chips specifically for label-free detection. The breakthroughs in the high-sensitivity, portability, and low-cost nano-scale fabrication led her to a Research Excellence Award, which is offered to 10 awardees out of 3000+ researchers, by the Society of Photo-Optical Instrumentation Engineers. The importance of her overall work is reflected by her jointly filed patent application and leading authorship of nine manuscripts.